Politecnico di Torino
Prima Facoltá di Ingegneria
Scuola di Dottorato in Fluidodinamica

Anno Accademico 2012-2013

Turbulence in fluids: two case studies of climate relevance

Roberta Sciascia
Matr.160150

Relatori: Antonello Provenzale
Fiammetta Straneo

Politecnico di Torino
Prima Facoltá di Ingegneria
Scuola di Dottorato in Fluidodinamica

Turbulence in fluids: two case studies of climate relevance

Roberta Sciascia

Home is not just the building where you live.

Contents

Chapter 1

Introduction

1.1 Motivation

Turbulence is one of the main open problems in fluid dynamics. Since the pioneering work of Kolmogorov, turbulence has been widely studied theoretically, numerically and experimentally. Earth's oceans are a complex web of physical phenomena and to fully describe the processes which determine their state, turbulence must be taken into account. Turbulence occurs over scales ranging from the very large (thousands of kilometers) down to very small scales (centimeters). Of particular relevance are problems such as: entrainment in overflows, mesoscale vortices and double-diffusion convection.

The dynamics of many important oceanic systems is closely related to turbulence. And the dependence of these systems on ocean variability is crucial to explore, for example, possible future climate. Thus, it is possible to explore the role of turbulence and parametrize its dynamics rather than fully resolve it.

This thesis is a summary of my PhD works. It explores the influence of turbulence on two different oceanic systems that can play a significant role in future climate variability: the marine ecosystem and the impact of high-latitude dynamics of Greenland fjords on submarine ice melting.

1.2 Outline

The thesis is conceptually divided into two distinct part organized as follows. In chapter 2 I will briefly discuss the role of turbulence in the oceans.

The first part of the thesis, presented in chapters 3-6, is dedicated to the interaction between oceanic ecosystem and turbulence. Chapter 3 will provide the theoretical background for the three original works written during my PhD and presented in the following chapters.

In chapter 4 I will present a research on the settling rates of particles in fully developed turbulence using DNS simulations. We address the role possible effects of pressure gradient of the flow field on the equation of tracers by using different settling measures. This term might be relevant for particles, such as plankton, with densities comparable to the one of the fluid in which they are embedded.

In chapter 5 we discuss the role of gravitational sinking in driving cell size selection by introducing a simplified parametrization of turbulence in an ecosystem model described by a set of differential equations. We show that the outcome of phytoplankton competition is determined by the dependence of sinking velocity on cell size, shape, and on the temporal variability associated with turbulence.

In chapter 6 an ecosystem model similar to the one presented in chapter 5 is used to describe the dynamics of high-altitude alpine lakes. The results are compared with measurements from 12 alpine lakes in the Gran Paradiso National Park. Model results are consistent with measured data, indicating the appropriateness of this modeling approach for quantitatively studying mountain lake ecosystems and their response to environmental changes.

The second part, chapter 7 and 8, will explore the high-latitude dynamics of Greenland fjords. Chapter 7 provides the theoretical background necessary to present my research.

In chapter 8 I will present a model for the impact of fjord dynamics on submarine melting of a Greenland glacier. Using a non-hydrostatic fjord scale model we investigate the variability of melt rates and circulation as a function of the far field water properties in the fjord, external forcing and glacier properties.

Finally I will draw some conclusions and present some future development.

Chapter 2

Turbulence in the Ocean

2.1 The nature of the turbulent flow

Giving a simple definition of turbulent flow it is no simple task and one can find many process oriented definitions of turbulence. The oceanographer James McWilliams tried to describe the properties of turbulent flows in term of dualities between a regular and turbulent flow.

- Deterministic vs random.
- Orderly versus chaotic.
- Time reversible versus time irreversible.
- Materially confined versus dispersive.
- Conservative versus non-conservative.
- Quasi-periodic and spatially smooth versus broad-band.
- Predictable versus unpredictable.
- Smooth versus sensitive dependence.
- Statistically regular versus statistically irregular.
- Globally ordered versus locally ordered.
- Persistent versus transient, evanescent, chaotically recurrent patterns.

Turbulence is the dominant physical process in the transfer of momentum and heat and in dispersing solutes and small particles in the oceans. Thus the natural state of the ocean is one of turbulent motion and the knowledge of turbulence and its effects is crucial in understanding how the oceans works and in the construction of numerical models.

The mean depth of the ocean is 3795 m and the typical speed are $0.1ms^{-1}$. This means that the characteristic Reynolds number, Re, of the ocean is of the order of 4×10^8 that is much greater than the critical value of 10^4 predicted by Reynolds Reynolds [1883, 1895]. The ocean should be therefore turbulent with large overturning eddies mixing the water column. Indeed the ocean is turbulent, but turbulent motion is patchy and eddies do not overturn on a scale comparable to the water depth.
The reason for this lies in a factor that was not considered by Reynolds but that has a vital role in determining the nature of turbulence in much of the ocean. These are the density variations due mainly to the atmospheric heating and the redistribution of heat by ocean's circulation. Understanding the processes that lead to density variation means also knowing the turbulent forcing of the ocean.

2.2 Turbulent forcing

Most of the turbulence in the ocean is induced by processes that can be divided into two categories.
In the surface and benthic boundary layer, *external processes*, in the form of buoyancy and momentum fluxes through the boundaries generate turbulence. In the upper layer the atmosphere plays a crucial role though wind events and convection, on the bottom layer turbulence is induced by tides and geothermal heating.
On the other hand turbulent *internal processes* are for example shear across density interface, internal waves and double diffusion convection. Figure 2.1 is a schematic classification of mixing processes according to their source of energy.

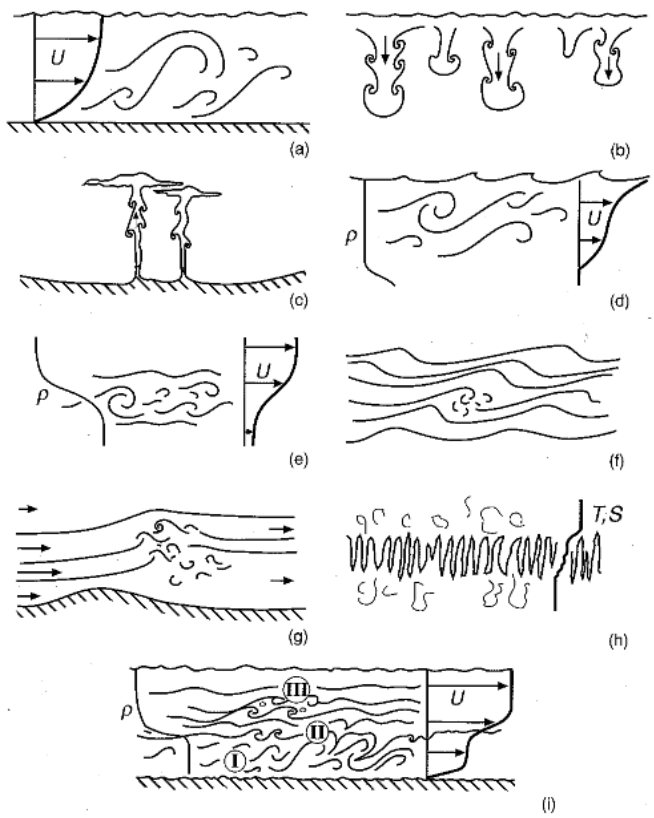

Figure 2.1: Classification of mixing processes according to their source of energy. (a)-(d) External processes: (a) Turbulence induced by tides or wave over a solid boundary, (b) Convection due to cooling at the sea surface, (c) same process for (b) but due to geothermal heating, (d) wind-generated turbulence. (e)-(h) Internal processes: (e) Mixing in shear flow, (f) breaking of internal waves, (g) Mixing in internal hydraulic jump, (h) Double diffusive salt-fingers. (i) Interaction between three different mixing processes (a, e, f) (Thorpe [2007]).

2.3 External processes

Buoyancy and momentum fluxes lead to three main types of boundary layer, those in which

- the stress is negligible and in which the turbulent motion is due to unstable stratification and convection
- there is no flux of buoyancy and turbulent motion is driven by the stress
- there are both stress and buoyancy fluxes.

It is furthermore necessary to say that the physical presence of a boundary (i.e. seabed) constrains and modifies the form and scale

of turbulence close to the boundary itself.
In the following subsection are presented examples of idealized steady state conditions and, although the ocean can rarely be described as steady, if the changes in fluxes are negligible in comparison with the mean fluxes some of these processes can be useful to study the ocean mixing properties.

2.3.1 Convection with no shear

In 1900 Bénard showed that in a laboratory fluid a steady cellular flow occur when a thin horizontal layer of fluid is either heated from below or cooled from above.
The ocean is deep and the cooling of its upper surface can lead to a transient convective motion in which plumes of water are periodically generated. The periodic cooling of the sea surface leads to changes in the density structure and turbulence within the mixed layer.
One of the main causes of heating and cooling processes in the ocean is the diurnal cycle of the mixed layer which therefore experience a cycle of turbulent motion.
Some regions of the ocean, for example East Greenland, can experience extreme winter cooling resulting in convective mixing up to 1-3 km and plumes that can reach the bottom of the ocean.

A particular case of convection in the ocean is due to the continuous release of hot and buoyant fluid from hydrothermal vents on the ocean floor. The edge of the plume entrains water from the outside and the local rate at which the fluid is entrained into the raising plume is proportional to the mean speed of the raising plume. Buoyant plumes and entrainment processes are also found in overflows dynamics and close to cooling surface such as glaciers front.
Further discussion on plume theory and on turbulence in absence of convection (see next subsection) will be presented in the second part of this thesis (chapter 6-7) where they will be applied to the study of Greenland glaciers.

2.3.2 Stress and no convection

The condition of stress in absence of convection is commonly found at small distances, (0.05m to 2-5m), from a plane rigid boundary, but beyond a distance at which viscous effects and small-scale roughness,

have important influences on the flow. Thus this kind of turbulence results, for example, from braking waves on continental shelf or seabed.

2.3.3 Stress and buoyancy fluxes

The ocean is rarely in the state described in the two previous subsection but buoyancy and stress fluxes act together to produce mixing both in the surface and benthic layer.
We can therefore introduce, from dimensional analysis, a characteristic scale for turbulence in the convective boundary layer with an applied stress.
The only two available parameters are the buoyancy flux, B_0, $[L^2T^{-3}]$ and the surface stress, τ/ρ_0, $[L^2T^{-2}]$. By combining them we introduce the Obukov length scale

$$L_O = -u_*^3/(k/B_0) \tag{2.1}$$

where $u_* = (\tau/\rho_0)^{1/2}$ is the frictional velocity and k is the von Kármán constant. For positive values of B_0 we have that $L_O < 0$, this happens for destabilizing conditions that favour convection. The opposite is true for stabilizing conditions where the fluxes contribute to a stable stratification ($B_0 < 0$).
At distances from the boundary beyond the effects of breaking waves or viscosity if

- $z < 0.03 \mid L_O \mid$ buoyancy has little effect
- $0.03 \mid L_O \mid < z < \mid L_O \mid$ there are mixed conditions of buoyancy and stress
- $z > \mid L_O \mid$ buoyancy tend to dominate.

In the next two subsection we will consider separately some of the processes contributing to mixing in the upper ocean and benthic layer.

2.3.4 Mixing processes in the upper ocean

Turbulent processes acting in the surface layer are sketched in Fig. 2.2. some of which have already been described in the previous subsections.
The presence of waves makes a strong physical distinction between

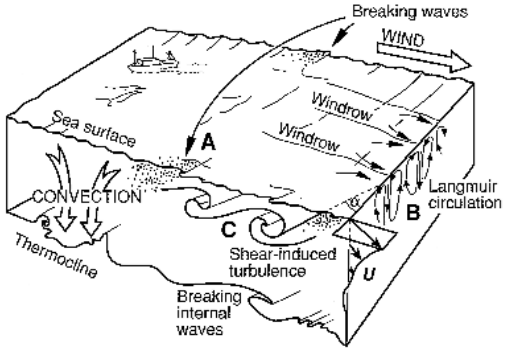

Figure 2.2: Sketch of the processes leading to the mixing of the upper ocean (Thorpe [2007])

this boundary layer and that near the seabed. The breaking of wind-generated waves creates turbulence that contribute to the mixing of the upper ocean and enhance the rates of dissipation and transfer of momentum into the mean flow.
In 1920s, Langmuir formalized the so-called Langmuir circulation found in the surface layer of the ocean and induced by the interaction of waves and shear flows. In the upper layer is often possible to see bands of foam aligned in the wind direction. These 'windrows' are signs of convergent motion in which water at the surface, although mainly moving downwind, also has spatially periodic cross-wind components that carry floating materials into the bands. To preserve the continuity, the water moves downwards below the band, leaving the buoyant material floating, and it then diverges and rises toward the sea surface.
This circulation can also carry planktonic organism and contributes to their vertical cycling within the mixed layer, therby exposing them to varying level of solar radiation.
The cells are not steady and have some of the properties of variability and transience found in small-scale turbulent motion, for this reason it is often described as 'Langmuir turbulence'. The Langmuir cells are large eddies that supply energy to the turbulent cascade within the mixed layer and distributes the turbulent energy produced at smaller scales induced by processes such as breaking waves.
The Langmuir cells are not the only coherent structures observed in the mixed layer, among the other we can cite the 'temperature ramps'. These are temperature gradient oriented in the across wind direction and tilted downwind of 45°. They are advected by the mean flow in

the mixed layer, and often extend for about a third of the thickness of the mixed layer.

2.3.5 The benthic boundary layer

Except near hydrothermal vents, over decaying organic material or where gases are released into the water column, the buoyancy fluxes through the seabed have little effect on the structure of the boundary layer.
Benthic boundary layers $5 - 60m$ thick with vertically uniform temperature and salinity and maintained in a mixed state by turbulence generated by shear stress are commonly found overlaying seabed in deep water. The near-bed flow will generally be strongly influenced by roughness and will ultimately determine the statistical spatial and temporal variability of the flow. Relative large roughness elements, such as stones, can produce flow separation and eddies.
Coherent structures, such as horseshoe vortices, have been identified within the turbulent flow above the sub-layer dominated by viscosity or small-scale roughness. In high Reynolds number flow hairpin are also a common coherent structure. These appear to be associated with larger than average Reynolds stress and represent a process of detrainment of fluid from the near-bed region of the boundary layer.

2.4 Internal processes

This section is about turbulence within the stratified body of the ocean. As we said before the processes leading to mixing in the stratified regions of the ocean are due to internal sources of energy. The main difference between turbulence in the stratified ocean and in the ocean's boundary layer is that the latter is generally sustained, being in close proximity to external energy inputs, whereas the former is usually intermittent, being maintained by variable and transient mixing processes such as internal waves.
Thus, most of the processes can be defined as transitional and they lead to turbulent motion from a relatively quiescent flow.
Two different processes usually dominate the generation of turbulence and diapyclan mixing in the ocean.
The first is the instability due to shear or different motion of water and is often caused by internal waves. The second process is a form of convection that result from the different molecular diffusion coefficient of heat and salinity.
We will describe these precesses in the next subsections.

2.4.1 Shear-flow instability

The instability that allows, in stably stratified flow, a small disturbance to grow is know as Kelvin-Helmholtz instability. For a steady, inviscid, non diffusive, two-dimensional, parallel horizontal flow instability can occur only when the gradient Richardson number in the flow,

$$Ri = N^2/(\mathrm{d}U/\mathrm{d}z)^2 \tag{2.2}$$

is less than 1/4 somewhere in the flow. Where N is the buoyancy frequency and $\mathrm{d}U/\mathrm{d}z$ is the vertical shear.
Flows in which Ri is greater than 1/4 are stable and a small perturbation decay or propagates as internal waves without increasing in amplitude. For instability to occur, the smallest Richardson number, Ri_{min}, must be less than 1/4 but this is not a sufficient condition. The largest value of Ri_{min} for which instability is possible is known as the critical Richardson number Ri_c of the flow. The value of Ri_c depends on the shape of the density and velocity profiles. When in a given flow, Ri is less than Ri_c at some level z, small waves will grow.

Turbulence in the stratified ocean is patchy. Internal waves produce transient shear, locally reducing the Richardson number and occasionally leading to instability or wave breaking that creates local patches of turbulence. Because the instability of a stably stratified shear flow depends on the Richardson number, le local value of Ri in the ocean may be useful to understand the factors leading to turbulence and can provide a means to quantify mixing.

2.4.2 Double diffusive convection

While internal waves breaking contributes substantially to the mixing of the stratified ocean, another process is evident in those regions where such mixing is relatively weak and in which the vertical gradients of temperature and salinity have the same sign. This form of convective motion is known as double diffusive convection.
This process is due to the different order of magnitude of the molecular diffusivity of salt, κ_S (about $1 \times 10^{-9} m^2 s^{-1}$) and the thermal conductivity κ_T (about $1.4 \times 10^{-7} m^2 s^{-1}$).
Seawater in which the temperature and salinity both increases upwards can be unstable even if the vertical density gradient is stable ($d\rho/\mathrm{d}z < 0$). A small volume of (non-turbulent) water moved upwards receive a heat by thermal conduction from the surroundings an so its temperature rises. Although its salinity will also rise through molecular diffusion, the rate of salt transfer is much less than that of heat, and as a consequence there are conditions in which the decrease in density of the displaced fluid through the rise in temperature exceeds the increase through salinity. Thus the fluid become less dense and continue to rise under buoyancy forces and developing a convective motion.

There are two types of double diffusive convection. The first is known as the 'finger regime' when, less dense but warmer and saltier water lies over colder fresher water. It is characterized by ascending and descending convective columns (fingers) of water, typically 1-6 cm wide. Because the molecular conductivity of heat is greater than the molecular diffusivity of salt, as described before, the density of the cold and fresh ascending fingers become less, being reduced by the more rapid transfer of heat than salinity from the surrounding descending fingers. The later, losing heat more rapidly than salinity,

become denser but remain more saline than the ascending finger and tend to continue their descent.
The second type of double diffusive convection is the 'diffusive regime', in which relatively warm and salty water lies beneath less dense cold and fresher water. If it is displaced downwards, the colder water becomes less dense, due to the molecular transfer, than the surroundings and rises buoyantly to recover its original position. Having achieved a lower density than when it started, overshoots its original position and continues to rise but now losing heat and becoming denser. The sequence of re-sinking and rising lead to a growing oscillation known as 'overstability'. The diffusive regime of convection can be active in the Arctic, for example above relatively warm and salty intrusion of water of Atlantic origin.
Frictional effects of viscosity limit the development and the motion of both types of instability and the width and growth rate of the fast-growing fingers depend on the kinematic viscosity.
The convection described so far does not involve turbulence, the motion driven by instability are laminar. Provided that the contribution to turbulence from other sources such as internal breaking waves is relatively weak, the initial form of instability in the double diffusive convection evolves into a spatially coherent structure containing layers of uniform temperature and salinity. These layers appear as a staircase in the temperature and salinity profiles.

2.5 Turbulent diffusion

In this section I will briefly discuss some of the properties of turbulent dispersion in the ocean.
There are several reason why dispersion is of fundamental importance in the ocean. It is dispersion that determines the distribution of natural traces, such as, salinity but it also has an important role in determining the dispersion of chemicals, oil or toxic algae. Dispersion is frequently related to highly anisotropic stirring motion, with vertical scales constrained by buoyancy. Dispersion depends not only on turbulent processes but also on the nature of the dispersant and on its buoyancy. Dispersants, such as dye, have little effect on the dynamics of the fluid while those like salinity may have buoyancy effect. Other

dispersants, at least in high concentrations, may change the turbulence properties of the water into which they spread. For example and oil film can reduce the frequency of wave breaking and the generation of near-surface turbulence.
Due to their complexity, it is difficult to address the dynamics of dispersants in general terms, however it is possible to focus the attention on two types.
The first one are those that float at the sea surface or that remain on a given isopycnal surface. The second are those, like dyes and solutes in low concentrations, that follow the motion and vertical diffusion of the turbulent water.
Since floating particles are constrained to remain on the sea surface or on isopycnal subsurfaces, their dispersion is essentially two-dimensional. Dyes are free to follow the fluid, thus their motion is fully three-dimensional.
Eddies play an important role in dispersion processes. If an eddy is much larger than a patch of dye, this is advected and distorted by shear or convergence. If the patch size is of scale comparable to that of turbulent eddies it is usually distorted in the field of shear and convergence between eddies. When, eventually, a patch reaches much greater size than the turbulent eddies the effect is to mix the fluid within the patch itself and slowly spread the patch at its outer boundaries.
The rates of dispersion of particles therefore depends on the presence of eddies with appropriate scale to cause their dispersion, and the coefficient of dispersion will vary according to how effective eddies of this scale are at causing dispersion. Just as the energy of eddies depends on size also their dispersive action will be scale-dependent.
Other processes that force motion, but which are not described as 'eddy-like' may contribute to the dispersion of a patch in the ocean as the time after its release increases and those are all the processes that induce turbulent motion (i.e. wind, diurnal cycle).
As well as temporal variability, spatial non-uniformity in dispersion may also be important, for example when a patch reaches the boundary of a region confined by tidal fronts or a region of enhanced mixing due to topography.

Dispersion is related to the spreading or relative position of particles

released as group at some instant of time, $t = 0$. The location of a particle relative to its starting point is

$$X(t) = U_0 t + x(t) \tag{2.3}$$

where U_0 is the mean speed of a group of particles and $x(t) = \int_0^t u(\tau)\mathrm{d}\tau$. The relative spread of particles depend on weather or not their motions are similar and consequently on weather their locations remain similar. This is related to the idea that eddies are larger than the distance between particles and will move all the particles in a similar way, and therefore contributing little to increasing the size of the cluster. Eddies of size comparable to or smaller than the distance between particles will move them apart.
A measure of the time scale over which the speed of a particle remain similar while encountering eddies is given by the velocity autocorrelation function, $R(\tau)$. The smallest time, τ, at which R becomes zero provide an approximate measure of the timescale over which the motion remains coherent.
A more useful measure of the separation rate of particles is obtained by integrating R over the separation time τ giving the the so-called Lagrangian integral time scale. $T_L = \int_0^\infty R(\tau)\mathrm{d}\tau$ which represent the time for which a particle's speed remain strongly coherent or self correlated.

To conclude it is also necessary to mention the effects on positively or negatively buoyant particles. The distribution of sediment particles sinking within a closed circulation, like the Langmuir cells, is an example of dispersion of non-neutral traces.
Sinking particles may be trapped for some time in Langmuir cell and prevented from sinking. If the fall speed of particles through still water exceed the maximum upward flow speed in the cells, the circulation affects the paths but they will always have a positive downward velocity and sink through the cells. If, however, the maximum upward vertical speed in the circulation exceed the particles fall speed, there is a region within which particles may be trapped.
However the Langmuir circulation is more intense near the surface than at depth and it is unsteady. This means that relatively small-scale turbulent motions may eject particles from one cell into another or the circulation may break down before neutrally buoyant particles can be carried around a cell.

This chapter has provided an overview of the main processes leading to mixing of the ocean both in the boundary layer and in the pycnocline and the role of turbulent dispersion in the dynamics of natural and anthropogenic tracers. In the next chapter I will discuss how some of these processes affect the dynamics of marine ecosystem.

Chapter 3

Ocean and marine ecosystem interaction

Marine ecology is traditionally defined as the study of marine organisms together with the surrounding environment. The recent growing interest in this research is due to many reasons, among which we can cite

- the physical processes underlying some of the large-scale biological phenomena are now better understood.
- the advancements in the quality of biological measurements
- the interest in understanding fundamental processes to better manage ocean's resources.

  and last but maybe the most important

- the need to understand marine ecological processes influencing the greenhouse effect and other aspects of the climate.
  The carbon dioxide sequestration from the atmosphere onto the surface waters and then in the deep ocean from biological processes is a fundamental mechanism for climate change.
  Marine organisms contribute also to aerosol formation that is one of the key variable for a better estimate of possible future climate scenarios.

When talking about marine ecology is important to define the spatial and temporal scale of the problem we are considering.
The typical length scale can vary up to 14 order of magnitude. Ocean basins are $10000km$ wide and they confine the largest biological communities. The average depth of the euphotic layer and mixed layer is

$\sim 100m$ and these are more often critical for the open-ocean biological processes.
The typical size of bacteria is $10^{-6} - 10^{-5}$, plankton can go from $10^{-5} - 10^{-1}$ while fishes can reach up to $50m$.
In this theoretical introduction and in the following two chapters we will focus our attention on plankton dynamics.

The interaction between plankton and the ocean system can occur at different scales.
For processes on a scale less the a $1km$, the turbulent motion and viscous boundary layers affect the locomotion and feeding of plankton cells which are also influenced by the mixed layer dynamics.
At mesoscale, processes on a scale of $1 - 1000km$, the presence of winds, coherent vortices and costal upwelling affects the availability of nutrients in the upper ocean.
At large scale, which means processes on scale of thousands of kilometres, the possible changes in the overturning circulation might affect the biological productivity of the ocean and the thermohaline circulation and its interaction with the atmosphere is also influencing the spatial distribution of plankton species in the oceans.

At first approximation one might think that the time scale should change in direct proportion to the length scale. While the physical feature determine the spatial scale of the ecological processes it's the organism itself that determines the time scale.
Plankton may complete a generation in few days or weeks maximum, and as a consequence, they can have rapid fluctuations in numbers.
It is furthermore necessary to introduce the concept of ecological and evolutionary time scales. The evolutionary time scale is define as the time in which a population of organisms acquire and pass on new traits from generation to generation. On the other hand the ecological time scale is shorter, of the order of tens to hundreds of years, and focuses on community events.
It follows that some of the physical processes might be relevant for plankton dynamics just on one of the two time scale.

In the three following sections I will overview the ecosystem-ocean dynamics at different scales. The small scale is presented in section 3.1, in section 3.2 I will discuss the mesoscale to conclude in section 3.3 with the large scale.

3.1 Small-scale interaction

When talking about the small-scale interaction between marine ecosystem and the environment we look at two processes: the dynamics of a single plankton cell and that of the mixed layer.
Due to their size, the dynamics of a plankton cell has some fundamental constraints. For a micro-organism viscosity is all important. Small plankton particles are affected by viscous drag and swimming in water is like swimming in honey for a human being.
A cell of about $1\mu m$ diameter swimming at $30\mu m s^{-1}$ and then stopping would come to a complete stop in $0.6\mu s$ having travelled only $10^{-4}\mu m$ (Purcell [1977]). A small crustacean 'rowing' to move itself forward would go forward an then backward exactly at its original position.
The reason for that lies in the governing equations of motion, the Stokes flow equation (3.1), which are time-reversible.

$$\begin{cases} \nabla p = \mu \nabla^2 \mathbf{u} + \mathbf{f} \\ \\ \nabla \cdot \mathbf{u} = 0 \end{cases} \tag{3.1}$$

In the small-scale boundary layer of a plankton particle the viscosity causes the average speed of the flow to decrease from its value in the open ocean to zero at the boundary. The size of the turbulent eddies also decrease to zero at the boundary which means that they are not as efficient as in the open ocean to transport nutrient. This creates problems for organisms and the cells metabolism is restricted by the lack of turbulent transport which is instead replaced by the slow transport due to molecular diffusion Munk and Riley. [1952].
However the thickness of the boundary layer can be reduced proportionally to the speed of the flow past to it, which means that plankton particles have adopted different strategies to reduce the thickness of the boundary layer.
There are mainly two strategies. The first one is to have a heavy cell which sinks through the water column. This technique is employed for example by diatoms and all those cells denser than water and it works best in the mixed layer where the stirring tendency of the turbulent flow counteracts the sinking of the organisms. Without turbulence the

diatoms would all end up in the deep water where there is insufficient light for photosynthesis.
This problem will be further analysed in chapter 4 using a DNS simulation of particles in a turbulent flow.
Swimming is the second technique adopted by plankton particles that have motion organs. The most common mechanisms to swim in a viscous environment are 'corkscrew' and flagella.
The effectiveness of these two techniques depends on the size of plankton particles. Small flagellates, in the range of $1-10\mu m$, move in order to find better concentrations of nutrient in the environment, not to reduce their diffusion limitation. On the other hand bigger particles that are able to swim up to 10 times their body length may have a significant increase in nutrient uptake by swimming.
For sinking particles only the large cells sink fast enough to gain a significant advantage form it in term of nutrient uptake. Figure 3.1 shows the fractional increase of nutrient flux for different cell sizes as a function of speed.

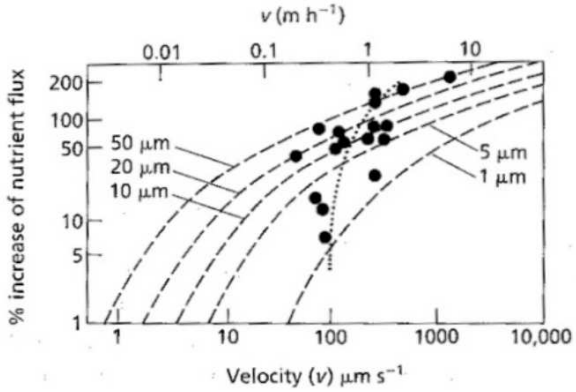

Figure 3.1: Fractional increase of nutrient flux to the cell surface as a function of velocity and cell diameter (Sommer [1988]).

In no case these cells can overcome nutrient limitation by sinking or swimming, but the differences between cells can be great enough to influence competition. In chapter 5 I will partially explore this problem using an ecosystem population model, that takes into account different sinking rates depending on particle size.
Thus, in the viscous plankton environment the only possible advantage of motility for the organism is that it might find nutrients in higher concentration.
In all the previous discussion turbulence has never been taken into

account. The first study to take into account the effect of turbulence on molecular diffusion close to small organisms was made by Munk Munk and Riley. [1952]. They suggested that the turbulent-pressure fluctuations in the ocean create a small relative motion between the organism and the water because the two have slightly different densities but with a negligible effect on diffusion near the cell. Lazier Lazier and Mann [1989] re-examined the issue in terms of shear created by turbulence and the effect on the diffusion. Figure 3.2 is a summary of the increase diffusive flux due to the relative motion and to turbulence.

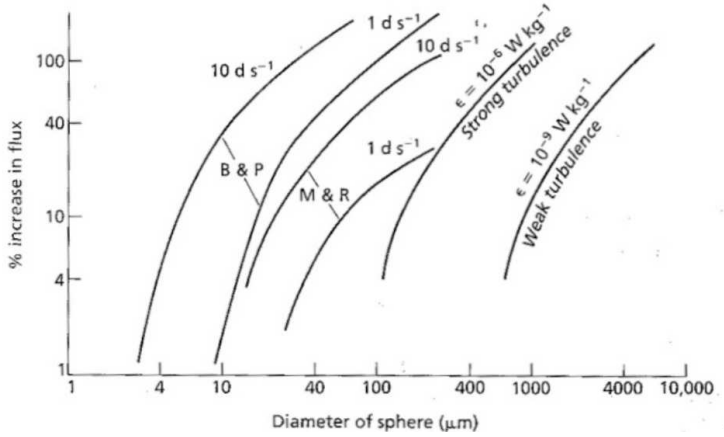

Figure 3.2: Percentage of increase in the diffusion flux created by relative motion or turbulent shear. The curves for the relative motion are for sinking or swimming of 1 and 10 diameters per second (ds^{-1}) based on two different works (Lazier and Mann [1989]).

The turbulence curves show that even strong turbulence will not have an appreciable effect compared to the relative motion through the water. But for a stationary cell the turbulence will start to have an effect on cells greater than $100\mu m$ in diameter. In weak turbulence, only cells larger than $1mm$ will be affected.

After the overview of the single cell interaction with the ocean I will now address the problem of biology in the mixed layer.
One of the problem of phytoplankton in the ocean is the need of nutrient and light for growth and reproduction. The source of light comes from above, while the source of nutrients is at depth. The sunlight is absorbed by the water and decrease exponentially so there is a finite layer, the euphotic zone, in which there is enough light for photosynthesis and growth. In an ocean with no turbulence the euphotic zone would become depleted of nutrient from phytoplankton uptake.

The nutrients in the deeper ocean are constantly replenished from the decomposition of dead organisms and, in absence of turbulence, all the nutrients would be all kept at depth.
Because the real ocean is turbulent the typical structure of the water column is more like the one reported in figure 3.3. Thus, the persis-

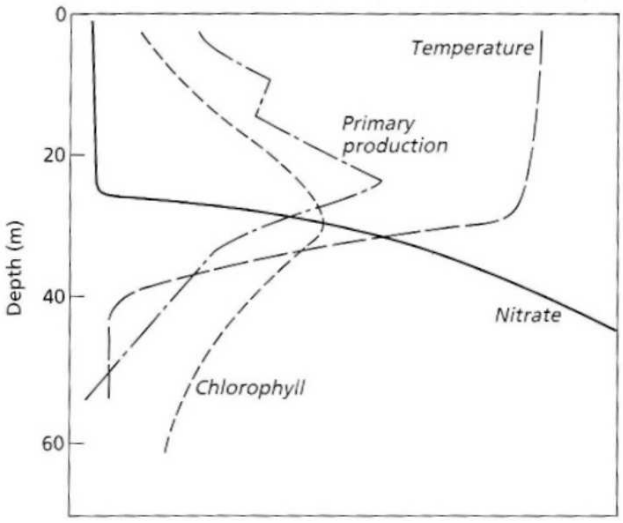

Figure 3.3: Schematic diagram showing water column composition in tropical waters.

tence of phytoplankton community in the mixed layer depends on the vertical transport of nutrient but might be also influenced by horizontal advection.
The ocean mixed layer can be divided into different areas depending on the changes in water properties that ultimately influence the marine ecosystem.
If we look at the mixed layer of the open tropical ocean, the properties are relatively constant throughout the year except for the equatorial upwelling zones where the majors ocean currents cause upwelling of nutrient-rich waters from below the thermocline. In temperate and polar waters seasonal changes are more evident and also the diurnal cycle might be important in exposing phytoplankton to light fluctuation. In winter time, the downward mixing generated by convection at the cooled surface and wind-driven turbulence cause a deepening of the mixed layer in polar and temperate waters. This means that that turbulence penetrates deeper into the zone of high nutrients and brings them up in the euphotic zone. On the other hand it means that phytoplankton, carried by turbulent mixing, stay longer below the euphotic zone where photosynthesis is not possible. The opposite

happens in spring time conditions both for phytoplankton and for nutrients.
The results of the shallowing of the mixed layer after a period of vertical transport of nutrient is the so called spring bloom that is an enhanced primary production (i.e. production of organic compounds).

In this section we have seen that small scale processes can have a significant role both on the single cell dynamics and on the ecosystem. Individual cells have changed their motion techniques to overcome viscosity limitation while the presence of mixed layer dynamics influences the availability of nutrients in the euphotic layer and the growth of plankton population.

3.2 Mesoscale interaction

In this section I will consider processes on the scale of thousands of kilometres such as wind-induced upwelling regions, fronts and internal waves. This processes can determine the import at surface of nutrient and the composition of phytoplankton population.
One of the approach that can be used at this scale, as well as, at the large scale is to model the ecosystem through population dynamics equations. Instead of looking at a single particle one can look at the dynamics of different classes of organisms and model them with different sets of equations depending on the mean characteristic of that given class.
There are two main types of population model in plankton dynamics. The NP (Nutrient-Phytoplankton) model where the ecosystem is modelled using only nutrient and phytoplankton dynamics and the NPZ model (Nutrient-Phytoplankton-Zooplankton) where the zooplankton is also included in the model. These are the two basic structures of population model but they can be increased in complexity by adding for example different type of nutrient or classes of plankton depending on their size.
An NP model can be described as follows:

$$\begin{cases} \dfrac{\mathrm{d}N}{\mathrm{d}t} = f(N, P, ...) \\ \\ \dfrac{\mathrm{d}P}{\mathrm{d}t} = g(N, P, ...) \end{cases} \tag{3.2}$$

where $f(N, P, I...)$ and $g(N, P, I...)$ are functions that parametrize for example the mortality rate, growth rate, consumption of nutrients, sinking rates and competition for resources for all the compartments considered in the model.
In chapter 5 I will present a NP model to understand some implications of the turbulent variability due to mesoscale processes focusing on size selection.

Let us first consider the effects of coastal upwelling on marine ecosystems. The intensity of the coastal upwelling regions is not uniform. It is influenced by the location of the coastal current (California, Peru, northwest, southwest or northeast Africa) and it is also influenced by topographic features such as canyons that give rise to complex upwelling patterns. This complexity is increased by seasonality and by isolated evens in which wind stress and the associated upwelling tend to build and decline over a period of up to 10 days.
Available data shows that these isolated events tend to enhance the biological productivity because they create temporary spring bloom-like conditions. In temperate waters the alternance between winter mixing and spring stratification provide the conditions for the spring bloom. In upwelling areas the period of maximum wind stress provide the upwelling of nutrients while the periods in between provide well-stratified conditions in which phytoplankton is held in the euphotic layer permitting photosynthesis, nutrient uptake and population growth.

Plankton production is also influenced by sharp gradients typical of front systems such as tide fronts or shelf-break fronts.
Shelf-sea or tidal-mixing front have been widely studied more than other front systems. These fronts separate the tidally-mixed region from the stratified region and are areas of enhanced plankton productivity. One of the reasons for this production was found in the convergence of surface water and the relative downwelling. Any organism buoyant enough to resist the downwelling would aggregate to the front. Thus passive advection was a possible explanation for plankton concentrations in fronts.
Shelf-break fronts occur where winter cooling and wind mixing lead to cooler, less saline water on a continental shelf with warmer and saline water offshore. In this case the associated plankton production is due

to the formation of tidally-driven internal waves with the consequent vertical transport of nutrients to the surface.
Upwelling fronts form at the interface between normal shelf water and the cool, nutrient-rich water brought to the surface during wind-driven coastal upwelling. This type of front can vary in time and space depending on the wind patters. Biological studies suggested that planktonic organisms tend to aggregate to the coastal side of the front resulting in a enhanced plankton productivity.

The last mesoscale processes that can influence plankton dynamics are tides, tidal mixing and the generated internal waves.
The changing in water level due to the tides leads to pattern of different planktonic organism known as zonation. This is due to the different exposure to air and to the changes in temperature between upper and lower regions of the tides. The tides, interacting with the sea floor, produce turbulence that prevent from stratifications and generate areas of well-mixed ocean. In situations where tidal mixing is less strong and the water column becomes stratified the formation of internal waves on the thermocline causes the redistribution of nutrients.
If tidal currents are strong enough to mix the water column all year, there is a continuous supply of nutrients from near-bottom waters up to the euphotic zone, which permits phytoplankton production throughout the summer. This is in contrast with the situation in stratified waters, where the supply of nutrients tend to become depleted after the spring bloom. As a result, tidally-mixed areas, have production levels higher than adjacent stratified areas.
One of the important features of these tidally-mixed areas is that their boundaries act as natural barriers to create ecological niches where some species prevail and maintain their genetic differentiation.
If we look at internal waves the motion shows an alternance of zones of upwelling with divergence and downwelling with convergence. Buoyant material tend to aggregate in the convergence zone allowing phytoplankton to associate with it and move shoreward. This process might be significant in adaptations of organisms habiting the convergence zone.

In these section we have briefly overview the effects of masoscale processes on adaptation and evolution of organisms living in areas of

the ocean where these are relevant. Thus studying the ocean ecosystem interaction at this scale might be relevant on an evolutionary and ecological point of view.
The formation of niches in tidally-mixed areas, for example, can have an important role on ecological time scale. Organisms adapting to the internal waves convergence zone are on the other hand affected on a evolutionary time scale.

3.3 Large-scale interaction

In this section we will look at the effect of large scale ocean circulation on marine ecosystem and also at the possible impact of future climate change on marine biology.
Organisms have adapted to various physical regimes associated with the large-scale circulation, such as, warm and cold core rings that detach from western boundary currents or ocean gyres. Some of them use the boundary currents for long range transport other use gyres as niches in which they grow to maturity.
The presence of rings and gyres modify the pattern of primary production in the center of ocean basin, far from the upwelling regions, to values considerably higher than expected.
One interesting ecological dynamics that can enhance biological production is that of cold and warm core rings. An research cruise followed six cold rings and their interaction with the Gulf Stream. The biological characteristic of the rings changed more rapidly than the physical one. In the early stage the center of the ring had much higher phytoplankton concentration. The primary production was about 50% higher of that of the nearby areas. As the time went by, the heating of surface waters, caused a shift to smaller specie and to a greater diversity so that the plankton community in the ring resembled more to that of the surrounding sea with productivity that falls to lower values.
This study showed that the formation of these highly productive core can change the dynamics of seas that are usually characterized by low productivity.
Warm-core rings are also areas of primary production and are mainly regulated by two physical mechanisms. The first one is isopycnal mixing that brings deep, nutrient rich water to the surface at the periphery of the ring.
The second physical process that regulate the primary production is due to cooling of the surface waters that become cooler than those at depth and thus generating convective mixing and a well-mixed deep layer. Since the isotherms are depressed in the core, convective mixing in the center may carry phytoplankton at greater depth while bringing at the surface those of the outer ring and stimulating phytoplankton

production in this area.

By using the example of the North Atlantic, it is possible to look at the effects of climate variability on marine ecosystem and looking at the combined effect of ocean and atmosphere. One important climate phenomena is the so called North Atlantic Oscillation (NAO) and is characterized by fluctuations in the difference of atmospheric pressure at sea level between Iceland and the Azores. The NAO is essentially due to the atmosphere but its effect are evident also in oceans waters. The best-known effect of the North-Atlantic oscillation are warm winters in Europe that coincide with cold winters in Labrador and west Greenland and vice versa.
By looking at this index is possible to divide the 20th century in three main phases: (i) before 1935 when the index was predominantly positive and winters in Europe were warmer than average; (ii) between 1935 and 1950 when the index was oscillating; and (iii) between 1950 and 1965 when the index was falling and remained negative until 1971. This was a period of increasing cold northerly winds over the waters of north-east Atlantic. Many biological records show some connections between the index and the productivity and variety of species in the North Atlantic. Before 1935, thanks to the warm winters in Europe subtropical species appeared off the coast of western Europe. On the other hand once the cooling trend was established there was a well documented decline in phytoplankton ad zooplankton biomass.

The last large scale interaction that can also have implication on possible future climate scenarios is the interaction between the thermohaline circulation and the biology and the sequestration of carbon dioxide from the atmosphere.
In the regions of deep water formation large quantities of carbon dioxide dissolved in the water sinks at great depth while in the regions of upwelling th carbon dioxide is given back to the atmosphere. On top of these main physical mechanism there is also the contribution due to biological effects, known as the biological pump.
Biological processes lead to a net flux of carbon dioxide into the ocean. This mechanism operate on the entire surface of the ocean where carbon dioxide is fixed through photosynthesis and introduced into the deep ocean by the sinking of dead organisms.
When looking at possible future changes in CO_2 concentration it is

important to take into account this biological process. Since the biological pump is responsible for the downward transport of carbon dioxide into the deep ocean any factor that decreases the biological activity, while the upward transport from the deep ocean continues at its normal rate, will lead to an increasing atmospheric CO_2.
In addition to their role in the fixation of carbon dioxide, phytoplankton can influence the earth's climate through the production of dimethylsulphide (DMS). Most species of phytoplankton excrete DMS, and a part of it escapes to the atmosphere where it reacts to form methane sulphate aerosols and the latter stimulates, for example, the formation of clouds over the oceans.
Trying to predict the possible biological consequences of climate change is a difficult task. Regardless of which will be the most relevant physical changes in ocean dynamics, planktonic organisms can adapt quickly to them. This means that after a few years of changed environmental conditions, the planktonic community may have changed its species composition and adapted to a new regime.

In this chapter we have investigated the interaction between ocean dynamics and marine ecosystem.
The interaction can occur at different spatial and temporal scales influencing the distribution of nutrient and plankton but also the evolution of different species. In the following two chapter I will present two personal work where I have addressed the interaction between ocean turbulence and planktonic communities using two different approaches.

In chapter 4, I will investigate the small scale dynamics of the mixed layer by looking and the settling rate of particles in a turbulence DNS model. In chapter 5, using an NP model, I will focus on mesoscale interactions and the effects on selection of plankton cell size. In chapter 6, a similar ecosystem model is used to to investigate the dynamics of high-altitude alpine lake. Model results are consistent with data collected in the Gran Paradiso National Park, indicating the appropriate-

ness of this modeling approach for quantitatively studying mountain lake ecosystems and their response to environmental changes.

Chapter 4

Settling rates of particles in turbulent water

Roberta Sciascia, Claudia Pasquero, and Antonello Provenzale, Preprint

Abstract

The settling of particles in a homogeneous and isotropic turbulent environment, simulated by the numerical integration of the Navier-Stokes equations, is investigated. Here we address the role of particle density, in the equation of motion for passive tracers and its effect on settling rates. Especially we address the role of the term due to the effect of pressure gradient of the flow field on the dynamics of tracers. This term might be relevant for particles, such as plankton, with density comparable to the one of the fluid in which they are embedded. We use different metrics to characterize the particle settling rates and show that they provide different informations. In the explored range of parameters, the distribution of vertical velocities integrated along particle trajectories shows a dependence on size and density and the effects of the term $\rho_f/\rho_p \sim 1$ on particle settling rates is minor compared to the effect of Stokes viscous drag and buoyancy.

4.1 Introduction

The settling of heavy particles in turbulent flow is relevant for a wide range of physical phenomena, from the dynamics of cloud droplets and aerosols in the atmosphere, to the motion of plankton cells in aquatic environments. Numerous studies have addressed the issue, following theoretical, numerical and experimental approaches, often leading to contrasting results depending on the details of the flow. Heavy particles dynamics in a moving flow has been discussed theoretically in the pioneering work of Stommel Stommel [1949]. He considered particles moving in a two-dimensional steady cellular flow field according to the balance of the gravitational force with the Stokes drag force, and showed the existence of equilibrium points (at which the local flow velocity is equal and opposite to the particle free-fall terminal velocity) and of closed orbits that lead to indefinite suspension. Maxey and Corrsin Maxey and Corrsin [1986] repeated the study including particle accelerations and described what has later become known as the *sling effect*: heavy particles tend to be ejected from high vorticity regions and concentrate in high strain regions between the flow cells; closed orbits no longer exist and heavy particles eventually end up in the downflow regions between the cells, causing an increase of the

mean settling rate compared to what happens in still fluid. Pasquero et al. Pasquero et al. [2003] used a steady random two-dimensional flow to demonstrate that closed orbits and suspension still occur in presence of particle inertia, provided that the flow has closed streamlines with changing sign of curvature, so that the sling effect pushes particle trajectories to alternatively cross the flow streamlines outward and inward the eddy core. More complex flows have also been used to investigate the problem, such as those given by three dimensional Gaussian random velocity fields Maxey [1987], direct numerical simulation of three-dimensional isotropic turbulence Wang and Maxey [1993] and experimental grid generated turbulence Ruiz et al. [2004]. Contrasting results have been reported in one dimensional models Deleersnijder et al. [2006], in two dimensional cellular flows Afonso [2008], in kinematic turbulence Fung [1993], in large eddy simulations et al. [2006] and in experimental grid generated turbulence Zhou and Cheng [2009], indicating that different mechanisms, not yet fully understood, exist as well. The studies cited above concentrate more on the complexity of the flow but always using the equation of motion for particles of Maxey and Riley Maxey and Riley [1983] in the approximation of heavy particles ($\rho_P >> \rho_f$). However, this approximation does not hold for some physical processes for example, plankton cells, have density close to that of the ocean.
Given the relevance of this problem, in this work we investigate the equation of motion both in the limit of $\rho_f/\rho_p \sim 1$ and $\rho_f/\rho_p \sim 0$. We integrate numerically the motion of heavy particles in homogeneous and isotropic 3D turbulence and focus on the settling velocity integrated along the particle trajectory, studying its distribution across the particle population. In this way, we are able to provide new insight into the dynamics of particles in turbulence in both density limits.

4.2 Model formulation

4.2.1 Model description

The non dimensional flow field is obtained by direct numerical simulation (DNS) of the three dimensional Navier-Stokes and the continuity

equations:

$$\begin{cases} \partial_t \mathbf{u} + \mathbf{u} \cdot \nabla \mathbf{u} = -\nabla p + \nu \nabla^2 \mathbf{u} + \mathbf{f} \\ \nabla \cdot \mathbf{u} = 0 \end{cases} \tag{4.1}$$

where p is the pressure field, $\mathbf{f}$ is the external energy source, and ν is viscosity. The domain, defined as a box of size $L = 2\pi$, is periodic in every direction. Energy is injected at any timestep by adding a zero mean divergenceless field characterized by wavenumber $k_f = 2$, random phase, and energy $\epsilon \Delta t$, where ϵ is the energy dissipation rate and Δt is the integration time step.

The equation of motion for passive, point-like, neutrally-buoyant tracers is written as $d\mathbf{V}/dt = \mathbf{u}(\mathbf{X}, t)$ where $\mathbf{V}$ is the (Lagrangian) tracer velocity and $\mathbf{u}(\mathbf{X}, t)$ is the Eulerian velocity of the turbulent flow at the tracer position, $\mathbf{X}$, and at time t. The equation of motion for particles is written assuming low particle concentration, particle size much smaller than the Kolmogorov length scale, small Reynolds particle number. Under those conditions, the flow around the particle can be considered as a Stokes flow, and the motion of a small rigid sphere of radius a and density ρ_p, located at position $\mathbf{X}$ and moving at velocity $\mathbf{U} = (U, V, W)$ is described by Maxey and Riley [1983], Armenio and Fiorotto [2001], Cencini et al. [2006]:

$$\begin{cases} \frac{d\mathbf{U}}{dt} = \delta \frac{D\mathbf{u}(\mathbf{X},\mathbf{t})}{Dt} + \frac{1}{\tau}(\mathbf{u}(\mathbf{X}, t) - \mathbf{U} + \mathbf{W_T}) \\ \\ \frac{d\mathbf{X}}{dt} = \mathbf{U} \end{cases} \tag{4.2}$$

Here, $\tau = 2a^2(\rho_p - \rho_f)/(9\rho_f \nu)$ is the Stokes time, ρ_f is the fluid density, $\delta = \rho_f/\rho_p$ is the ratio between fluid and passive tracer density and $\mathbf{W_T} = (0, 0, -\tau g)$ is the free-fall terminal velocity in still fluid. We perform two sets of experiments one in which $\delta << 1$ (i.e.$\rho_p >> \rho_f$) and the term due to the pressure gradient of the flow can be neglected and another in which $\delta \sim 1$ (i.e. $\rho_p \sim \rho_f$)

The fluid equations are integrated until a statistically stationary steady state is achieved, then $N_p = 32768$ neutrally-buoyant tracers and N_p heavy particles are uniformly seeded through the domain. The initial velocity for the heavy particles is given by the sum of the fluid velocity at the particle location and the terminal velocity $\mathbf{W}_T$. We use a third-order Adam-Bashforth spectral integration scheme for both

Table 4.1: Non dimensional parameters of the DNS: Microscale Reynolds number R_λ, resolution N^3, maximum wavenumber k_{max}, viscosity ν, energy dissipation rate ϵ, root-mean-square velocity u_{rms}, domain size L, Taylor microscale $\lambda = (15u_{rms}^2\nu/\epsilon)^{1/2}$, Kolmogorov length scale $\eta = (\nu^3/\epsilon)^{1/4}$, grid spacing δx, Kolmogorov time scale $\tau_\eta = (\nu/\epsilon)^{1/2}$, eddy turnover time $T_e = R_\lambda \tau_\eta$

$R_\lambda = 70$	$N^3 = 128^3$	$k_{max} = 86$	$\nu = 0.001$	$\epsilon = 0.05$	$u_{rms} = 0.36$
$L = 2\pi$	$\lambda = 0.19$	$\eta = 0.012$	$\tau_\eta = 0.14$	$T_e = 10$	

Table 4.2: list of τ_p and δ values used in the simulations

δ	τ_p
0	10^{-3}
	10^{-1}
	1
0.42	10^{-3}
0.7	$6 \cdot 10^{-4}$
	$9 \cdot 10^{-4}$
	$1.4 \cdot 10^{-3}$
0.88	10^{-4}
0.98	10^{-5}

the fluid equations and the integration of the particle trajectories. To compute the value of fluid velocity at the particle location we use cubic splines with the De Boor algorithm. Parameters of the fluid numerical simulation are reported in table 4.1. Different values of the non dimensional Stokes time τ_p and δ have been used to conduct the simulations and are reported in table 4.2. Fluid density is set to the typical value of the ocean, $\rho_f = 1030\ kg/m^3$ and particles radius has been varied from $80 - 120\mu m$. The explored range of parameters represent the typical dynamics of plankton particles in the ocean.

4.2.2 Settling Metrics

Settling velocity is often measured as the ensemble mean of the instantaneous vertical velocity of the advected particles (e.g. , Maxey and Corrsin [1986], Deleersnijder et al. [2006], Ruiz et al. [2004]),

$$\langle W(t) \rangle = \sum_{i=1}^{N_p} W_i(t). \tag{4.3}$$

In the following, we drop the index i referring to the i-th particle, and use angular brackets to refer to ensemble averages.

Instantaneous velocities, however, do not take into account temporal correlations along particle trajectories. For this reason, they cannot give information on the effective behavior of each particle and thus cannot identify the possible presence of particles which stay suspended for long times. Other metrics, which carry a different information, can be used to characterize the velocity statistics of settling particles Davila and Hunt [2001]: The integral velocity

$$W_I(t^*, t) = \frac{1}{(t^* - t)} \int_t^{t^*} W(t')dt', \tag{4.4}$$

which provides a measure of the mean settling speed of a particle over the time interval $(t^* - t)$, and the bulk velocity

$$W_B(h, t) = h/(t^* - t) \ , \tag{4.5}$$

where t^* is the time at which the particle first arrives at the position $Z(t^*) = Z(t) - h$, which provides a measure of the mean velocity of a particle during the time taken to cover a given vertical distance.

The two metrics (4.4,4.5) describe the effective settling rate of the heavy particles. The distributions of these quantities, as well as their ensemble means, can differ from those of the instantaneous vertical velocities of the particles. In particular, the mean bulk velocity is always positive, since, by definition, its value is either zero or positive. A value of the bulk velocity equal to zero indicates that the particle stayed suspended - or moved upward - without reaching the plane at the level h below the starting position.

The differences between the instantaneous, integral, and bulk velocities are expected to be important mainly at short time intervals (of the order of the Lagrangian decorrelation time) and small values of h, when the temporal correlations of particle velocities are important. In 3D turbulent flow, it is expected that on long enough times (much longer than the Lagrangian decorrelation time), all particle will have a similar behavior and no long-term differences will be encountered.

4.3 Results

By construction, the initial ensemble mean velocity of a homogeneous distribution of neutrally-buoyant tracers is zero and that of a homogeneous distribution of heavy particles is the free-fall velocity in still fluid. The initial probability distribution function (pdf) of the differences between the instantaneous velocities and the ensemble mean, for both the tracers and the heavy particles, is equal to the fluid velocity pdf over the entire domain. In the course of time, inertial particles tend to be ejected from elliptic regions Maxey and Corrsin [1986], Cencini et al. [2006], leading to a preferential particle concentration in high-strain regions. Correspondingly, the velocity pdf of the particle distribution becomes different from that of an equivalent set of passive, neutrally-buoyant tracers, as illustrated in figure 4.1. Heavy particles with small τ have a slightly wider distribution than tracers, as the low velocity regions in the eddy cores are not sampled. Heavy particles with large τ have a narrower distribution Snyder [1971], as their motion is essentially given by the free fall velocity with some perturbations due to the turbulence Nielsen [2007]; the perturbations are weak for particles with large inertia. The mean values of instantaneous velocities are statistically equal to the free-fall terminal velocity.

Next we turn attention to the integral velocities. Their ensemble mean values do not provide new information, as $\langle W_I(t^*, t)\rangle$ is equal to the time average of $< W(t') >$ in the interval $[t, t^*]$. Second-order statistics, however, are slightly different: figure 4.2. Particles with small τ have a decay of the velocity variance similar to that of neutrally-buoyant tracers which follows fluid trajectories around the eddies, and on average it does not move neither up or down. Heavier particles, with a larger τ, all behave similarly and tend to be trapped in downdraft/updraft regions which implies a slightly faster decay of the velocity variance, at least for short time scales. To explore the effect of flow pressure gradient on particles velocity we consider tracers with $\tau = 10^{-3}$ and integrate the equation of motion in both regimes. In the explored range of parameters, when the pressure gradient term is included in the equations, particles tend to go from a neutrally-buoyant behavior to that of heavy particles (Fig. 4.2) with preferential particle

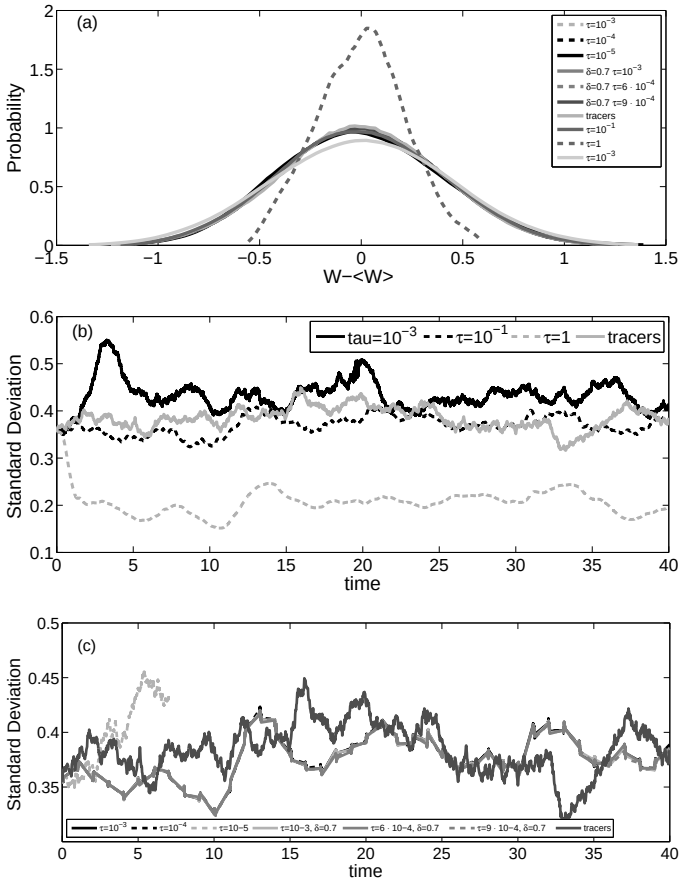

Figure 4.1: Probability distribution (pdf) of the instantaneous vertical velocities for neutrally-buoyant tracers and for heavy particles, averaged over the time interval [10:40] (panel a). Panels b and c show the root mean square of the pdfs versus time (panel b for $\rho_p >> \rho_f$ and panel c $\rho_p \sim \rho_f$) Mean values have been removed.

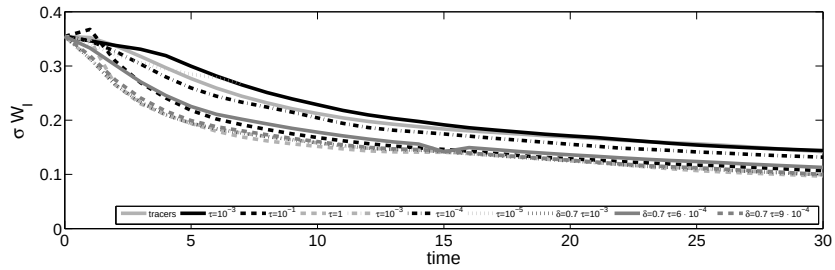

Figure 4.2: Standard deviation of the distribution of integral velocities, $W_I(t^*, 0)$, as a function of the duration of the integration time interval t^*. Eddy turnover time is 10 non dimensional units.

concentration in high strain regions.

The properties of the heavy particle motion are further revealed by the statistics of bulk velocities. We choose $h = 0.07$, a distance that tracers typically cover in a time that is longer than the eddy turnover time. The velocities of neutrally-buoyant tracers and particles with small τ (panels a-c) are small compared to the r.m.s. fluid velocity. Most particles, over this distance, have very similar bulk velocities and the distribution of bulk velocities is unimodal. However, the distributions show a population of particles that have a bulk velocity that is larger than the free fall settling velocity, indicating that, over those distances, turbulence can enhance the settling rate of the heavy particles. Quite importantly, there is also a population of particles whose bulk velocity is smaller than the free fall velocity. The bulk velocity distribution for particles with larger τ (panel d-f) is qualitatively different and it is Gaussian with mean value greater than the r.m.s. fluid velocity. The presence of two populations of particles is further analyzed in Fig. 4.5. For short H, all heavy particles have bulk velocity greater than their free fall velocity. As τ decreases tracers splits into two distinct populations of particles.

4.4 Conclusion

In this work we have numerically investigated the settling of heavy particles in homogeneous and isotropic 3D turbulence, is different density regimes. Our analysis indicates that the instantaneous vertical velocities give little information on the effective settling rate of the particles. Integral velocity distributions are much wider for heavy particles than for tracers, due to the presence of long temporal correlations along particle trajectories, associated with the inertial terms in the equation of motion.

In the explored range of parameters, the effect of the term due to pressure gradient of the flow filed cannot be neglected. This indicates that caution must be taken in situations where particles density is relevant, such as for phytoplankton in aquatic environments or for dust and aerosol in the atmosphere.

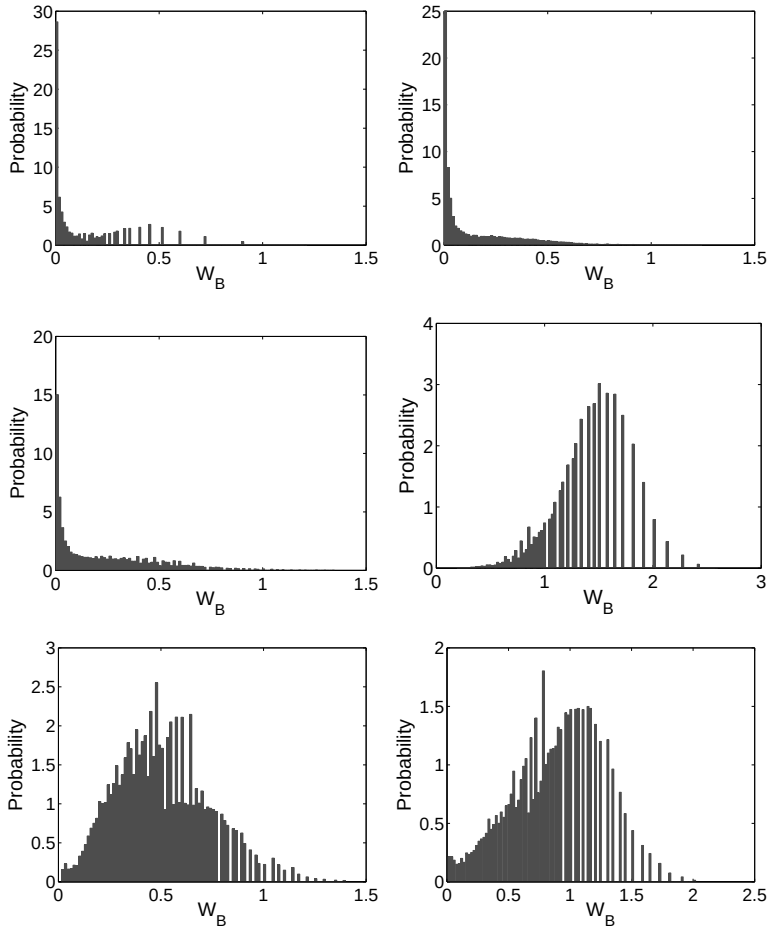

Figure 4.3: Distribution of bulk velocities for $h = 0.07$ for (a) fluid particles, (b) heavy particles with $\tau = 10^{-3}$, (c) heavy particles with $\tau = 10^{-4}$, (d) heavy particles with $\tau = 10^{-3}$ with pressure gradient term, (e) heavy particles with $\tau = 10^{-1}$ and (f) heavy particles with $\tau = 9 \times 10^{-4}$ and $\delta = 0.7$.

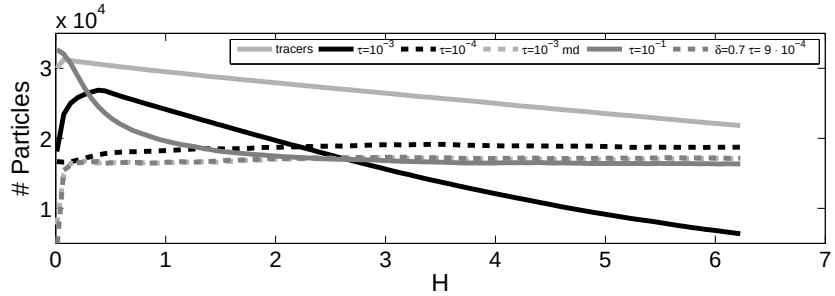

Figure 4.4: Number of particles with $W_B > W_T$.

Chapter 5

Physics of sinking and selection of plankton cell size

Roberta Sciascia, Silvia De Monte, and Antonello Provenzale,
Physics Letters A (2013), Volume 377, Issue 6, Pages 467-472

Abstract

Gravitational sinking in the water column is known to affect size composition of planktonic communities. One important driver toward the reduction of plankton size is the fact that larger cells tend to sink faster below the euphotic layer. In this work, we discuss the role of gravitational sinking in driving cell size selection, showing that the outcome of phytoplankton competition is determined by the dependence of sinking velocity on cell size, shape, and on the temporal variability associated with turbulence. This opens a question on whether regional modulations of the turbulence intensity could affect size distribution of planktonic communities.

5.1 Introduction

Phytoplankton need light for photosynthesis and nutrients for metabolism and reproduction. Light comes from above and penetrates only the upper layer of the ocean, down to a depth of about 100 meters, in a region called the euphotic zone (that is, the zone which is rich in light). In the ocean, nutrients come mostly from below, from the deeper layers where bacteria transform dead biomass and excreta into nutrient. As a result, phytoplankton live only in the upper layer, where most of the oceanic primary production takes place. However, since phytoplankters are usually slightly heavier than water, they tend to sink in the water column. If they sink too deep, they exit from the euphotic zone, cannot perform photosynthesis and eventually do not survive.

In a still fluid, at large times sinking is regulated by the Stokes law, which determines the terminal velocity of a small, spherical particle as $W = \left[2g\left(\rho_p/\rho_f - 1\right)/9\nu\right]x^2$ where ρ_p is the density of the falling particle and ρ_f the density of water, g is the acceleration of gravity, ν is the kinematic viscosity of water, and x is the radius of the falling particle. The terminal velocity for an homogeneous, spherical plankton cell with radius x =50 μm is about 4 m/d Smayda [1970], and it would thus take about 25 days to fall below a surface mixed layer with depth of 100 meters. From the expression of the terminal velocity, one also sees that (keeping fixed the density of the falling particle and the properties of water) larger particles fall faster than small objects. From this, it would seem that smaller phytoplankters

are favored, and should become dominant at the expenses of larger phytoplankton.

Sinking is not the whole story, however, and other elements enter the picture. Cell size is widely considered as one of the main determinants of planktonic taxa success, due to its relation to multiple physiological, ecological and life-history traits Schmidt et al. [2006], Litchman et al. [2007]. Cell size-dependent metabolism and resource exploitation, for instance, can induce allometric trade-offs that shape size distribution in habitats with different nutrient availability Falkowski and Oliver [2007], Yoshiyama and Klausmeier [2008]. The ability to capture nutrients and transform them into biomass, in particular, depends on the size of the phytoplankton cell Jiang et al. [2005].

The spatial and temporal distribution of nutrient input in the euphotic layer is another determinant of plankton dynamics. Nutrient input is rarely homogeneous and it is shaped by the pattern of upwelling and downwelling (that is, by the vertical velocity field). This non-homogeneous and temporally variable nutrient input has important effects on the marine ecosystem, some of which have been studied at depth in past years, see for example Pasquero et al. [2005] and references therein.

The depth of the euphotic layer in the open ocean roughly corresponds to that of the mixed layer, the surface oceanic region where the effects of winds and waves vertically homogenize water properties (such as temperature and salinity) and nutrient concentration. This, in turn, creates an additional source of complexity. The mixed layer is one of the most turbulent regions of the ocean. Thus, phytoplankton live in a highly turbulent environment, where fluid dynamical processes control many aspects of their lives. In this sense, fluid dynamics, and its interaction with gravitational sinking, is one of the important components of marine ecosystems.

The presence of turbulence can heavily affect settling of heavy particles, and in past years this fact has generated some discussions on the role of turbulence in shaping plankton communities. As pointed out more than thirty years ago by Margalef [1978], the adaptive success of planktonic cells must depend also on their ability to match the mixing intensity in the water column. Turbulence in the mixed layer affects

nutrient availability and light exposure, as well as the settling speed of negatively buoyant particles, therefore shaping the distribution of cells along the vertical gradients of nutrients and light Huisman et al. [2002], Estrada and Berdalet [1997]. More recently, however, Ruiz et al. [2004] have conducted laboratory experiments showing that turbulence increases the settling rate of heavy particles, and Jiang et al. [2005], using a simple ecosystem model and a Stokes terminal velocity for the falling phytoplankton, concluded that smaller phytoplankton are favored, and that evolutionary pressures would be toward reducing the size of phytoplankton cells, contradicting Margalef's suggestion.

However, the situation is more complicated and the effects of turbulence on heavy particles depend on many factors. In particular, the exploration of particle dynamics in a flow model with complex, turbulent-like streamline topology has revealed that particles heavier than the fluid can stay suspended for long times owing to the interaction between particle inertia and streamline curvature Pasquero et al. [2003]. Those results also rationalized the discrepancies observed in experiments with different flow configurations (and thus different types of streamline curvature statistics), indicating that in turbulent environment, individual heavy particles can sink with velocities which can be far different from the Stokes terminal velocity in still fluid.

Several theoretical and experimental works have indeed revealed that the relation between size, as measured by the cell radius, and sinking rate does not universally obey the Stokes law Peperzak et al. [2003]. Rather, one should consider that the sinking rate has a general form that depends both on the shape of the cell and on the degree of vertical mixing Chase [1979], Stemmann et al. [2004], Guidi et al. [2008], and the importance of vertical mixing in shaping plankton community composition has been demonstrated both in laboratory and field experiments Laws [1975], Pannard et al. [2007], Jaeger et al. [2008]. Based on these results, here we adopt the view that turbulence in the water column can slow down plankton sinking, and explore the consequences of such effect. Similar consequences will also be found in regions where upwelling conditions prevail, that is, where upward vertical velocities prolong plankton suspension.

In this Letter, we study the effects of sinking on plankton competition and include a generalized form of the dependence of the sinking

rate on size in a simplified ecosystem model. We thus explore, in a conceptual modeling framework, how different sinking regimes affect phytoplankton dynamics. In order to focus on this specific process, we ignore other relevant aspects such as the role of non-homogeneous nutrient input. The results of our study indicate that different dominant sizes emerge, depending on the intensity of sinking. Given the process-oriented approach followed here, we neglect the role of light limitation and the spatial inhomogeneities in nutrient input associated with turbulence and upwelling Pasquero et al. [2005], and focus only on the direct effects of sinking on plankton mortality.

5.2 The dynamics of sinking

The sinking rate of heavy particles is determined both by their volume, shape and aggregation state and by the fluid dynamical properties of the mixed layer. The motion of a small, homogeneous spherical particle which is denser than the fluid is described by an equation which can become quite complicated and includes many terms, see e.g. Provenzale [1999]. Here, we use a simplified description based on the equation Maxey and Riley [1983], Pasquero et al. [2003]

$$\frac{d\mathbf{V}}{dt} = \delta \frac{D\mathbf{u}}{Dt} - \frac{1}{\tau}\left(\mathbf{V} - \mathbf{u}\right) - \left(1 - \delta\right) g\hat{z} \tag{5.1}$$

where $\mathbf{V}$ is the (three-dimensional) velocity of the particle, $\mathbf{u}$ is the Eulerian fluid velocity at the particle position, $\hat{z}$ is the upward-pointing unit vector in the vertical direction, and $D/Dt = \partial/\partial t + \mathbf{u} \cdot \nabla$ is the material (Lagrangian) derivative. The constant g is the acceleration of gravity and $\delta = \rho_f/\rho_p$ is the ratio of the fluid density ρ_f to the density of the falling particle, $\rho_p > \rho_f$. The Stokes time scale is $\tau = 2x^2/(9\nu\delta)$, where x is the radius of the particle and ν is the kinematic viscosity of the fluid; note that this value of τ strictly depends on the assumed spherical shape of the particle. In equation (5.1), the Stokes term $-\left(\mathbf{V} - \mathbf{u}\right)/\tau$ forces the particle velocity to become equal to the fluid velocity, the buoyancy term pulls the particle downwards, and the inertial term $\delta D\mathbf{u}/Dt$ causes the particle trajectory to deviate from a fluid particle path. Previous works Maxey and Riley [1983], Tanga and Provenzale [1994], Provenzale [1999] have shown that terms such as the added mass Thomas [1992], Druzhinin and Ostrovsky [1994]

and the Basset term Benjamin [1986], play a minor role in the type of dynamics of interest in this work. Therefore, in the simplifieddescription adopted here, we have discarded the added mass term, the Basset history term, the lift force and the Coriolis acceleration.

When the fluid is at rest, $\mathbf{u} = 0$. Equation (5.1) simplifies to

$$\frac{d\mathbf{V}}{dt} = -\frac{\mathbf{V}}{\tau} - (1-\delta)\, g\hat{z} \ . \tag{5.2}$$

At long times, the solution of this equation tends to $\mathbf{V} = -W\hat{z}$ where $W = g(1-\delta)\tau = \left[2g\left(\rho_p/\rho_f - 1\right)/9\nu\right] x^2$ is the terminal velocity of a small spherical particle in still fluid.

A source of complication is related to the effect of non-vanishing fluid velocity. However, determining the effects of turbulence on particle settling has been a controversial issue. For example, Stommel [1949] showed that heavy particles can be permanently suspended in a steady two-dimensional array of eddies, provided one discards the particle inertia term. Perhaps based on this result, Margalef [1978] assumed that turbulence can prolong particle suspension, and built a view where larger phytoplankers (e.g., diatoms) are favored in turbulent environments while smaller cells (e.g., dinoflagellates) are favored in quieter waters.

However, Maxey and Corrsin [1986] later showed that the inclusion of particle inertia excludes the possibility of permanent suspension as found by Stommel. Indeed, owing to their inertia, particles tended to concentrate in the downward portions of the flow, falling even faster than in still fluid. Apparently, the relatively recent laboratory experiments by Ruiz et al. [2004] confirmed this view.

Both the theoretical arguments of Maxey and Corrsin [1986] and the specific experimental setting of Ruiz et al. [2004] are based on a (almost) regular array of approximately circular eddies, a configuration which is quite far from real turbulence. To settle the issue, Pasquero et al. [2003] considered a fluid configuration characterized by flow streamlines with complex, turbulent-like topology, and showed that in this case the particle behavior is much more complicated. While some of the particles do reach the downdrafts and fall faster, many others stay suspended and the whole population of heavy particles split into two sub-populations. For stationary two-dimensional flow, particles can stay suspended forever. For non-stationary flows, the re-

sults showed that permanent suspension of particles in turbulent flows becomes unlikely, but the particles can nevertheless stay suspended for much longer times than in still fluid. These findings helped understanding the results of several other laboratory experiments which, at variance with Ruiz et al. [2004], indicated that heavy particles in turbulent flows can fall either faster or slower than in still fluid Fung [1993], A.Srdic [1999], Davila and Hunt [2001].

The complicated situations depicted above for spherical particles becomes even more difficult to handle for spiny objects, see for example Mallier and Maxey [1991] for the simple case of elongated particles. Plankton cells are not at all spherical, and in this case the equations of motion become much more complicated, the fluid-particle interactions are difficult to describe and the particle velocity can be quite different from that obtained for spherical particles Smayda [1971], Padisák et al. [2003]. Under these conditions, more general power law expressions for the dependence of the sinking of heavy particles and marine snow aggregates on particle size have been adopted Guidi et al. [2008], Stemmann et al. [2004]. Observations have shown that often, these expressions can be approximated by using a different exponent in the dependence of the settling velocity on cell size Alldredge and Gotschalk [1988], Ploug and Grossart [2000].

Thus, if one thing was learned from all the exercises reported above, is that assuming a Stokes terminal velocity for falling plankton cells is probably a gross oversimplification. To simplify the problem for the goals of the present study, we generalize the Stokes expression and explore how the ecological dynamics of phytoplankton varies with a changing settling speed. In particular, we define the settling rate s of phytoplankton as the inverse of time required to fall below the euphotic layer, that is, $s = W/H$ where H is the depth of the euphotic layer and W is the terminal velocity of a small spherical particle. We then assume that

$$s\left(x\right) = \alpha \left(\frac{x}{x_0}\right)^{\rho} \tag{5.3}$$

where $x_0 = 50\mu$m is a reference size, ρ is the sinking exponent and α is the strength of the sinking. Clearly, for Stokes settling one has $\rho = 2$ and $\alpha = \left[2g\left(\rho_p/\rho_f - 1\right)/(9\nu H)\right] x_0^2$. By varying α and ρ, we can simulate particles falling either faster or slower than spherical particles

(with the same equivalent radius and density) in still fluid.

5.3 Model description

A typical Nutrient-Phytoplankton (NP) model describes the ecological dynamics of a resource-consumer system in the upper layer of the ocean, where phytoplankton feed on nutrient and light is abundant. For simplicity, we consider one type of nutrient, e.g. nitrogen in the open ocean. We assume a nutrient input into the system, associated with upwelling from deeper layers and/or dust deposition from the atmosphere, and a net biomass/energy loss associated with the sinking of dead biomass. Part of the dead phytoplankton biomass is recycled locally in the euphotic layer, while the remaining part sinks to lower levels. No light limitation is introduced in the simple formulation adopted here.

In our study of phytoplankton competition, we consider the dynamics of J phytoplankton populations that compete for the same (and only) limiting resource, that is, nutrient. Different phytoplankton types are distinguished only by a different size of plankton cells. Here, by *type* we indicate a phytoplankton compartment occupied by individuals with similar size; this could be a single species or a group of species with similar dimensions.

The model adopted is an extension of that discussed by Jiang et al. [2005] (JSF hereinafter), and it is written as

$$\begin{cases} \dfrac{dN}{dt} = I - g(N) \sum\limits_{j=1}^{J} \mu(x_j) Q P_j + \gamma m \sum\limits_{j=1}^{J} Q P_j \\ \\ \dfrac{dP_j}{dt} = [g(N)\mu(x_j) - m - s(x_j)] P_j \end{cases} \tag{5.4}$$

where all terms involving phytoplankton must be interpreted as referred to the appropriate phytoplankton compartment or as the appropriate sum.

In this model, N is the nutrient concentration and P_j is the biomass density of the j-th compartment of phytoplankton. The quantity x_j represents the linear size (equivalent radius) of a phytoplankton cell and the last term on the right-hand side of the nutrient equation is

a regeneration term which parameterizes the bacterial loop. The parameter $0 \leq \gamma \leq 1$ measures the efficiency of the local regeneration process. In this way, the nutrient is lost, mainly by sinking of dead biomass, from the euphotic layer, and the system is closed by the presence of the nutrient input term I associated with upwelling. In our formulation, all variables are dimensional, in order to keep track of the true size of the sinking cells.

The quantity Q is the nutrient quota of phytoplankton, that is, the mass of nutrient per unit phytoplankton biomass Van den Meersche et al. [2004]. For simplicity, here we assume the nutrient quota to be constant and the same for all phytoplankton compartments. The quantity $g(N)$ represents the nutrient consumption rate, assumed to have a Michaelis-Menten (Monod) form,

$$g(N) = \frac{N}{k+N} \tag{5.5}$$

where k is the half-saturation constant for nutrient uptake Eppley [1979] and is assumed to be the same for all phytoplankton types.

The size-dependent maximum growth rate of phytoplankton, $\mu(x_j)$, does not have a monotonic relationship with size. As reported in Jiang et al. [2005] and references therein, for large cell sizes the growth rate decreases with increasing cell size, while for much smaller cells, in the picophytoplankton range, the maximum specific growth rate tends to increase with size. A simple formula that mimics this behavior is Jiang et al. [2005]:

$$\mu(x) = \frac{x}{a_1 x^2 + a_2 x + a_3} \tag{5.6}$$

where a_1, a_2 and a_3 are constant parameters. Using the values of maximum growth rate from Raven [1994] and Tang [1995] we estimate the parameters $a_1 = 0.007\, d\, \mu\mathrm{m}^{-1}$, $a_2 = 0.261\, d$ and $a_3 = 1.925\, d\, \mu\mathrm{m}$, which correspond to an optimal size (from the point of view of nutrient uptake) of about 17 μm.

In homogeneous conditions, eqs. (5.4) indicate that only one phytoplankton size class survives, that is, the principle of competitive exclusion holds Hutchinson [1961]. The outcome of competition can easily be obtained by computing which species, at equilibrium, is able to reduce the nutrient level at the lowest value Tilman and Downing [1994].

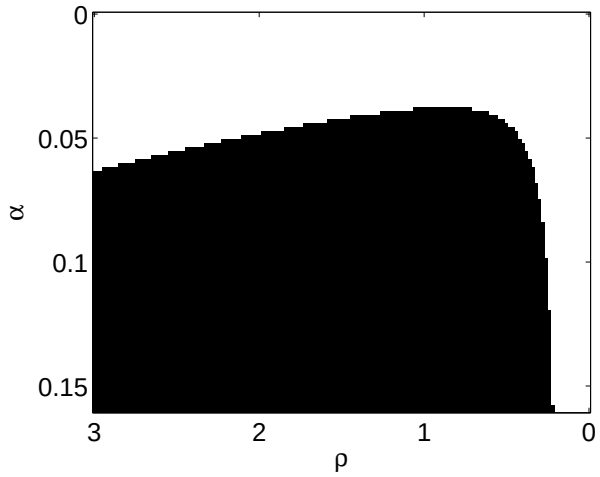

Figure 5.1: Survival of phytoplankton species as a function of the sinking parameters α and ρ in the two-species model. Black indicates survival of the smaller species ($x = 1.5\mu$m) and white of the larger species ($x = 76\mu$m).

In this model, phytoplankton losses are given by the sum of two terms: m represents a size-independent physiological mortality, and $s\,(x)$ represents a size-dependent, physical sinking term that depends on the intensity of turbulence in the euphotic layer and/or on the presence of vertical velocities associated with upwelling and downwelling, as well as, plankton cell shape. The base mortality m is assumed to be the same for all phytoplankton compartments.

The sinking rate $s\,(x)$ has dimensions of 1/time and it roughly represents the inverse of the time that a plankton cell takes to fall below the mixed layer. As discussed above, the sinking rate can be expressed as W/H, where W is the sinking (or settling) vertical velocity and H is the depth of the euphotic layer. In the JSF paper, the sinking term had the standard Stokes form, eq. (5.3) with $\rho = 2$), valid for terminal motion in still water. Assuming a mixed layer with depth in the range $H = (50 - 200)$ meters, this gives a sinking rate $s(x = 50\,\mu\text{m}) \approx (0.08 - 0.02)$ d^{-1}. For the reasons discussed in the previous section, in the following we shall allow a size-dependent sinking term with strength differing from the standard Stokes values for spherical particles in still fluid, and use instead the full form of eq.(3).

Table 5.1: Dimensional parameters and initial conditions for the NP model: Phytoplankton initial biomass concentration, P $[mg\, m^{-3}]$, nutrient initial concentration, N $[\mu M\, Kg^{-1}]$, nutrient input, I $[\mu M\, Kg^{-1} s^{-1}]$, mortality m $[d^{-1}]$, nutrient quota, Q $[NC^{-1}]$, regeneration fraction, γ, sinking strength in still or weakly turbulent fluid, α $[d^{-1}]$, half-saturation constant k $[\mu M]$

.

$P = 0.2$	$N = 15$
$I = 10$	$m = 0.03$
$Q = 0.1$	$\gamma = 0.5$
$\alpha = 0.08$	$k = 5$

5.4 Results

Figure 5.1 shows the results obtained by solving model (5.4) for two phytoplankton compartments, characterized by $x_1 = 1.5\mu$m (for example, cyanobacteria) and $x_2 = 76\mu$m (for example, diatoms), for the parameter values reported in Table 5.1 and varying α between 0 and 0.2 d^{-1} and ρ between 0 and 3. The figure shows that in this simple model the outcome of plankton competition depends on the sinking rate. Even using the standard Stokes value $\rho = 2$, the outcome of competition depends on the coefficient α, that is, on the shape and characteristics of the phytoplankton cells and on the intensity of turbulent motions which can prolong particle suspension. In keeping with the suggestion of Margalef [1978], where turbulent motions are not large enough to keep larger plankton suspended, smaller phytoplankton tend to be favored. In turbulent waters and in upwelling regions, sinking is reduced and the largest phytoplankton are favored. We have varied other parameters and functional forms in the model without obtaining qualitative differences to the situation depicted in Figure 5.1, indicating that the value of the sinking rate emerges as a crucial parameter in this type of model. Thus, at least with this formulation, the outcome of competition depends on the strength of sinking, which is controlled by the shape of the cells, the intensity of turbulence and the presence of vertical velocities. Repetition of the simulations with other values of the nutrient input rate indicate that in this simple model the outcome of plankton competition does not depend on the value of this parameter.

To provide a more complete picture, we have explored the outcome of competition in a system with J=50 phytoplankton compartments

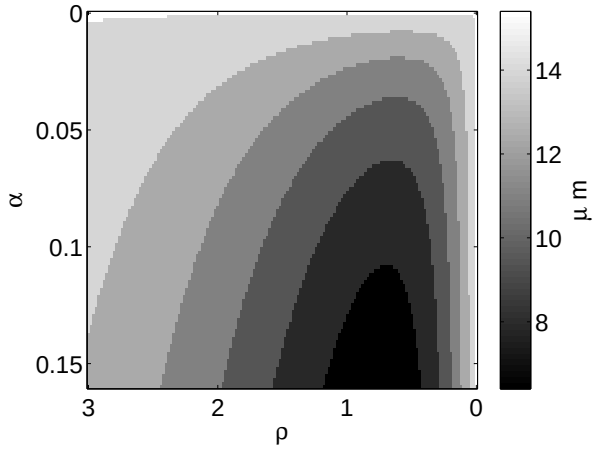

Figure 5.2: Size of the competitively dominant phytoplankton, in grayscale, as a function of the sinking parameters α and ρ for 50 compartments with different sizes.

with size ($1.5 \leq x_j \leq 76\mu m$). Figure 5.2 shows the size of the surviving phytoplankton compartments as a function of the sinking parameters α and ρ. From this figure, two facts emerge: (1) even for strong sinking, the favored species has not the minimum possible size, that is, the term associated with nutrient limitation at small size is effective at preventing dominance of ultra-fine phytoplankters; and (2) the size of the competitively dominant species varies continuously with both sinking parameters. In environments characterized by different sinking rates, we can thus expect a continuous distribution of dominant sizes.In this simple model, the selection of the competitively-dominant species does not display a dependence on the nutrient input rate. In fact, the outcome of phytoplankton competition is determined by minimization of the nutrient concentration and the nutrient input rate I enters as the same multiplicative factor for all species.

The results reported above refer to equilibrium conditions, where external forcings and sinking rates are kept constant in time. In natural situations, the pattern of vertical velocities and the sinking rate can vary in space and time. This has significant effects on primary productivity, as the ecosystem response to intermittent nutrient input is rather different from the response to spatially and/or temporally homogeneous input Martin [2003], Pasquero et al. [2005], Barton et al. [2010]. To determine the role of intermittent sinking conditions, we have analyzed the outcome of plankton competition in cases where the sinking term periodically alternates between standard values, corresponding to Stokes sinking in still (or weakly turbulent) water, and

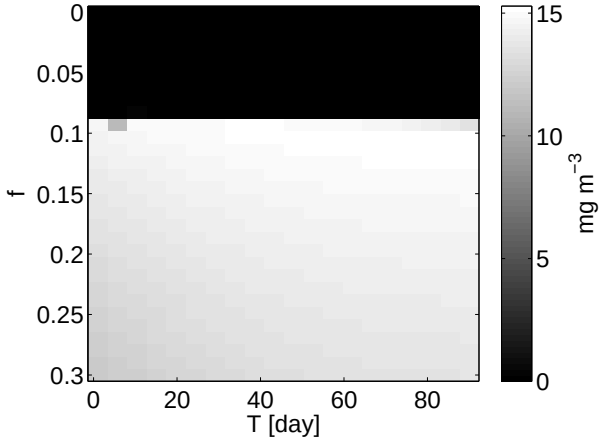

Figure 5.3: Average concentration of the largest phytoplankton species as a function of the period T of alternation between sinking and no-sinking and of the fraction of time f during which sinking is absent. For the parameter values chosen here, in a static environment ($f = 0$) the phytoplankton with smaller size dominate.

an extreme situation of no-sinking, associated with the temporary presence of cell suspension. That is, we assume $s(x_j) = 0$ during a fraction f of the period T of sinking rate variation, and $s(x_j) = \alpha x_j^2$ with $\alpha = 0.08$ d^{-1} during the remaining fraction of time. Once again, the two competing species have sizes $x_1 = 1.5\mu$m and $x_2 = 76\mu$m.

Figure 3 shows the outcome of plankton competition, as represented by the average concentration of the largest species, after having removed the initial transient period during which the system reaches a steady concentration. The results show that there is an approximate threshold f^* in the value of f: When $f > f^*$, the largest species is favored, while the opposite happens when the fraction of no-sinking is less than f^*. Interestingly, the value of f^* is rather small (for the parameter values used here, f^* is about 0.08), and thus rather limited regions/times of suspension are sufficient to allow the largest species to become competitively dominant. On the other hand, no dependence of the outcome of competition on the period of alternation between sinking and suspension has emerged, as it could have been expected from the fact that sinking enters the dynamical equations as a linear mortality term. We have also explored the case where nutrient input is modulated on the same temporal scale of the sinking rate, associating a larger nutrient input to the periods during which there is suspension (ideally generated by turbulent motions which can both delay sinking and enhance nutrient input). In the simple model adopted here,

the modulation of the nutrient input does not modify the outcome of the phytoplankton competition illustrated in figure 3. These results indicate that, in a system with alternate sinking and no-sinking conditions, larger phytoplankton species are usually favored. In our exploration of parameter space, we did not find any case in which the alternation of sinking and no-sinking allowed for the coexistence of phytoplankton species with different size, and on the long run only one compartment survived.

5.5 Discussion and conclusions

In this work we have numerically explored within an idealized setting how gravitational sinking may affect the outcome of phytoplankton competition. In general, when sinking is slower, owing for example to turbulent suspension or to the presence of upwelling, larger phytoplankton species are favored. Dominance of larger phytoplankton is observed also in the case of alternation between Stokes-like sinking and temporary suspension, as could happen in the case of advection past upwelling areas associated with mesoscale vortices or fronts, where vertical velocities can be intense and have a complex spatial and temporal pattern Koszalka et al. [2009].

These results indicate that the outcome of phytoplankton competition significantly depends on the pattern of vertical velocities and, possibly, on the level of environmental turbulence in the euphotic layer, confirming the view proposed by Margalef [1978]. Thus our results suggest that to capture this complex dependence, more sophisticated parametrization of the sinking velocity should be included in ecosystem models. Moreover they indicate that the dominance of smaller phytoplankton found by Jiang et al. [2005] does not hold when the sinking speed is not just the Stokes settling of spherical particles in still water. Also, the findings reported here indicate that consideration of phytoplankton dynamics in homogeneous environments can lead to misleading conclusions, as already reported by Pasquero et al. [2005] and references therein when considering a spatially varying nutrient input.

The models presented here are highly simplified, and complement the approach with more complex models discussed by Follows et al.

[2007] and Barton et al. [2010]. Several extensions of the work discussed here can be envisaged. For example, the possible interplay of non-homogeneous nutrient input with spatially or temporally variable sinking could be explored with spatially-extended versions of the model presented here. On the fluid dynamical side, one can address phytoplankton sinking in regional circulation models capable of properly representing the pattern of vertical velocities and the role of submesoscale diapycnal mixing Levy et al. [2001], Gruber et al. [2006]. On the ecological side, it would be interesting to consider more complicated trophic web structures and study how the bottom-up effects related to environmental turbulence compare and interact with top-down mechanisms such as those associated with predation by zooplankton. Finally, comparison with laboratory Estrada et al. [1987] or in-situ data would allow for testing the validity of these conceptual findings in aquatic ecosystems. We believe that the simple observations reported here provide evidence for the importance of turbulence and fluid dynamics in phytoplankton competition and motivate further study.

Chapter 6

A model for high-altitude alpine lake ecosystems and the effect of introduced fish

Ulrika Magnea, Roberta Sciascia, Francesco Paparella, Rocco Tiberti, and Antonello Provenzale,
Ecological Modelling (2013), Volume 251, Pages 211–220

Abstract

We discuss a simplified mathematical model for alpine lake ecosystems, describing the summer (i.e. ice–free period) dynamics of phosphorus, phytoplankton, three zooplankton compartments and fish abundance. Model output is compared with measurements of total phosphorus, chlorophyll–a and zooplankton biomass recorded in twelve high–altitude mountain lakes in the Gran Paradiso National Park (northwestern Italy) during the summer season from 2006 to 2009. Model results are consistent with measured data, indicating the appropriateness of this modeling approach for quantitatively studying mountain lake ecosystems and their response to environmental changes. The comparison between the results obtained for lakes without fish and those where the allochthonous brook trout (*Salvelinus fontinalis*) was introduced clearly indicates the strong impact of fish stocking in alpine lakes.

6.1 Introduction

Mountain areas and high-altitude alpine lakes are very sensitive to global and regional anthropogenic impacts, including atmospheric deposition and climate warming [Beniston et al., 1997], which affect the chemical and biological characteristics of lake waters such as species distribution, primary production, oxygen levels, and nutrient cycling [Sommaruga-Wograth et al., 1997, Parker et al., 2008]. Owing to the relatively small number of autochthonous species, high-altitude lakes are also characterized by low resilience to disturbances, and can be especially sensitive to the introduction of allochthonous species [Boavida and Gliwicz, 1996, Knapp et al., 2001].

The intensity of the environmental and climatic pressures currently insisting on high-altitude alpine lakes requires a quantitative assessment of the expected modifications, an endeavour which can be pursued by constructing a mathematical model of the lake ecosystem. In such an approach, one is faced with two opposing requirements. On the one hand, the model should be as complete as possible to catch the complicated workings of real ecosystems, a requirement that points toward building models with a large number of compartments. On the other hand, a model with many compartments is characterized by a

large number of parameters, whose values can be difficult to determine. For this reason, the benefits that potentially come with a large number of compartments can be obscured by parameter uncertainties. A trade–off between these two contrasting needs should thus be sought [Håkanson, 1995]. But most importantly, to study the impact of environmental changes it is necessary to verify whether such models are able to correctly reproduce in–situ measurements, a specific issue that we tackle here.

In this work we discuss a spatially homogeneous, six–compartment trophic network model for high–altitude, oligotrophic to ultra–oligotrophic alpine lakes and compare the model output with new experimental data from twelve mountain lakes in the Gran Paradiso National Park (GPNP) in the western Italian Alps. The data were collected during the ice–free summer periods (June–September) from 2006 to 2009. In six lakes, a species of fish, the brook trout (*Salvelinus fontinalis*), was artificially introduced several decades ago.

For lakes both with and without fish, the model output compares favorably with measured data, providing confidence in the use of this approach to describe the dynamics of high-altitude alpine lake ecosystems and the impact associated with the introduction of allochthonous species.

In Section 6.2 we introduce the characteristics of the lakes considered in this study and the experimental data. In section 6.3 we discuss the model formulation. The main results and the comparison between model output and data are presented in section 4, followed by a discussion of the main findings in section 6.5.

6.2 Data

The twelve mountain lakes considered in this study are located in the protected area of the Gran Paradiso National Park in the western Italian Alps, and their characteristics are summarized in Table 6.1.

All lakes studied here have glacial origin and are not affected by hydromorphological alterations. Their surface area is between 14,000 and 169,000 m^2 and all lakes are located above the local tree line, with watersheds belonging to the Alpine and Nival belts, see Tiberti et al. [2010] for a map of the area. All lakes but one (Lake Dres, 2087 m

Table 6.1: Characteristics of the GPNP alpine lakes considered in this study. The first six lakes are fishless, the last six lakes host a population of brook trout (*Salvelinus fontinalis*).

Lake	Longitude	Latitude	Altitude (m a.s.l.)	Max depth (m)	Area (m^2)	Catchment area (ha)
Nivolet Sup	07° 08' 41"	45° 28' 54"	2530	17.1	34482	29.11
Trebecchi Inf	07° 08' 48"	45° 30' 08"	2723	8.1	14812	43.76
Trebecchi Sup	07° 08' 40"	45° 30' 07"	2729	7.5	14172	23.66
Losere	07° 09' 25"	45° 28' 33"	2568	7.2	21401	43.48
Lillet	07° 12' 26"	45° 28' 00"	2765	13.2	36249	91.86
Motta	07° 24' 26"	45° 29' 55"	2656	51.0	101396	289.87
Leità	07° 07' 56"	45° 29' 28"	2701	11.0	62171	315.59
Nero (Leynir)	07° 09' 06"	45° 30' 28"	2747	22.1	44691	156.47
Nero (Djouan)	07° 10' 07"	45° 33' 07"	2671	6.0	17121	86.55
Djouan	07° 10' 43"	45° 33' 28"	2515	3.0	13341	30.60
Dres	07° 13' 26"	45° 24' 46"	2087	7.4	26112	291.85
Rosset	07° 08' 17"	45° 29' 47"	2703	46.9	168643	133.04

a.s.l.) are at an altitude between 2,500 and 2,800 m. The catchment areas are usually small (between 24 and 292 ha) and consist mainly of rock, debris and grassland, with very little vegetation in the form of shrubs. In some cases, glaciers cover some of the higher parts of the catchment area, but no lake is in direct contact with a glacier. The lakes are covered with ice and snow from October to late June. The mean annual precipitation recorded at the nearby meteorological station of Lake Serru (2275m) from 1962 to 2007 is 1147.5 mm and the mean snow depth from October to June is 93.2 cm, with peaks above 500 cm. The mean annual air temperature is 1.2 °C and the mean summer air temperature (from July to September) is 8.6 °C. The surface water temperature in these lakes never rises above 16 °C during the ice-free period. Some of the lakes display a full vertical mixing during summer, owing to their limited depth and the strong winds present at these altitudes. On the other hand, deeper lakes, develop a summer thermocline with two distinct layers.

The data, collected during the ice–free summer period (June-September) from 2006 to 2009, include geomorphological and geological lake characteristics, oxygen and temperature profiles, water chemistry, nutrient concentration and plankton abundance, constituting a rather uncommon and important data set on high-altitude mountain lake ecosystems [Tiberti, 2007, Tiberti et al., 2010]. Owing to the harsh climatic

conditions, not all data are available for each year. For this reason, in the following we will consider data from different years according to the available data set.

In most cases, water is well oxygenated throughout the water column [Tiberti et al., 2010]. Only the deepest lakes undergo stratification. Some lakes have a Secchi depth transparency smaller than the maximum depth, with values ranging from 3.6 to 11 m in July and from 5.3 to 15.5 m in August 2008. Lakes are not affected by acidification processes with pH in the range 6.5 - 8.6 [Tiberti et al., 2010]. The limiting nutrient for all lakes is phosphorus. The recorded total phosphorus levels ranged from 1 to 13 μg L^{-1}, with an average of 4 μg (0.13 μmol) per liter, which classifies these lakes as oligotrophic to ultra-oligotrophic. Total nitrogen ranges between 80 and 350 μg L^{-1}, with an average of 180 μg L^{-1}.

6.2.1 Bacteria and phytoplankton

The concentration of chlorophyll–*a*, measured in July and August 2007 using a spectrofluorimeter, ranges from 0.1 to 1.23 μg L^{-1}, with an average value of 0.53 μg L^{-1}. There is no significant difference in chlorophyll levels between the lakes with fish and those without fish. Using a conversion factor of chlorophyll–*a* to carbon of 50 [Reynolds, 2006], one obtains an average carbon content of phytoplankton of the order of 26 μg L^{-1}. Owing to the scarcity of nutrients, we expect phytoplankton to be dominated by species with small cell dimensions [Callieri et al., 2006]. Measurements indicate that, among picoplankton, cyanobacteria are rare (on average, less than 10 cyanobacteria per mL). On the other hand, in summer 2009 heterotrophic bacteria numbered around 1.8 million per mL, averaging over the whole water column and over all lakes.

6.2.2 Zooplankton

In the high-altitude alpine lakes at GPNP, zooplankton include protozoa, rotifers, copepods, and cladocerans; with low species diversity of the zooplankton communities [Tiberti, 2007, Tiberti et al., 2010]. A summary of the average characteristics of zooplankton in the GPNP lakes is reported in Table

6.2. Due to the absence of systematic data, the faunal assemblage

Table 6.2: Average body length, dry weight, and distribution of zooplankton species in the twelve lakes under study for the years 2006-2007. Only adult copepods and cladocerans have been identified at species level. The two values refer to lakes without fish and with fish, respectively. Lakes in which fish is present tend to have slightly smaller zooplankton.

Zooplankton	Average body length (μm)		Average dry weight (μg)		Number of lakes where found (2006 – 07)	
	No fish	Fish	No fish	Fish	No fish	Fish
Rotifers	119	119	0.15	0.15	6	6
Copepod nauplii	254	251	0.47	0.41	6	6
Copepodites	763	691	3.17	2.54	6	6
Arctodiaptomus alpinus	1236	1257	13.03	13.58	6	5
Cyclops abyssorum	1267	1249	17.33	16.57	6	5
Eucyclops serrulatus	–	740	–	4.21	0	1
European *Daphnia* gr. *pulicaria*	2103	–	47.04	–	4	0
Daphnia gr. *longispina*	1307	1002	14.14	6.42	5	5
Alona quadrangularis	699	652	5.85	4.30	3	2
Acroperus harpae	327	592	1.23	2.05	1	1
Chydorus sphaericus	352	323	1.78	1.32	2	5

of the community of protozoa is hard to estimate.

Several genera of rotifers have been observed in GPNP lakes (mainly *Keratella* and *Polyarthra*; occasionally *Notholca*, *Synchaeta*, *Hexarthra*, *Lecane*, *Euchlanis*, *Trichocerca*). In these lakes, rotifers have an average body length of 0.12 mm and an average dry weight of 0.15 μg, as measured during the ice–free period in the years 2006–2007 (see Table 6.2).

Assuming that 40% of the dry weight is carbon [Yúfera et al., 1997] (although this percentage can be highly variable), data from four measuring campaigns during summers 2006 and 2007, show that rotifer abundance in the GPNP averaged from 0.06 μg (0.005 μmol) carbon per liter in fishless lakes, to 1.9 μg (0.16 μmol) carbon per liter in lakes with fish.

In GPNP lakes, copepods are represented by Calanoids and Cyclopoids. Cyclopoid *Cyclops* gr. *abyssorum* and Calanoid *Arctodiaptomus alpinus* were observed in the alpine lakes, the latter accounting for $\sim$ 55% of the total copepod abundance both in lakes with and without fish. Cyclopoids of the species *Eucyclops serrulatus* sometimes lived at very low density levels in some of the studied lakes. Data for the copepod species at GPNP are summarized in Table 6.2. Copepod biomass is highly variable throughout the season and with

the year. It averages around 9.13 μg (0.76 μmol) carbon per liter in fishless lakes and 2.26 μg (0.19 μmol) carbon per liter in lakes with fish in the summers 2006 and 2007, assuming that 48% of dry weight is carbon.

Cladocerans (water fleas) range in size from 0.2 to 3.0 mm. The most common cladoceran species in the GPNP lakes is *Daphnia* gr. *longispina*, accounting for 76% of the cladoceran abundance in fishless lakes and 23% in lakes with fish population. Interestingly, some rare population of pigmented European *Daphnia* gr. *pulicaria*, phenotipically and genetically distinct from the remaining European populations, were found in lakes Nivolet Superiore, Trebecchi Inferiore, Trebecchi Superiore, and Lillet, and they represent up to 20% of the cladocerans in these fishless lakes [Tiberti, 2011].

As indicated in Table 6.2, some small cladoceran species were found as well. In fishless lakes, small species represent only 1–2% of the total number of cladocerans, but in lakes with fish the relative abundance of these species is larger (14%, 19% and 44% of the total respectively for *Alona sp.*, *Acroperus harpae* and *Chydorus sphaericus*). The average biomass of cladocerans, as measured in the years 2006–2007, corresponds to approximately 5.80 μg (0.48 μmol) carbon per liter for lakes without fish, and only 0.084 μg (0.007 μmol) carbon per liter in lakes with fish. However, these numbers can vary by an order of magnitude depending on the year and season. In the following we will assume carbon to be 48% of dry weight.

6.2.3 Macroinvertebrates and frogs

Fishless GPNP lakes are populated by a large number of macroinvertebrates, living in the water and on or near the surface. The littoral macroinvertebrates community is composed of several taxonomic groups including *Plecoptera*, *Trichoptera*, *Diptera*, *Coleoptera*, *Hemiptera*, *Acari*, *Oligochaeta*, *Planaria* and *Bivalvia*.

The only frog species found at this altitude is *Rana temporaria*, which is well adapted to cold climates and can live at temperatures close to 0 °C. This amphibian is found in four fishless GPNP lakes, but it survives only in one lake with fish (Lake Djouan), possibly owing to the presence of a small fishless pond near the lake where tadpoles can survive. These findings support the hypothesis that

the *Salvelinus fontinalis* exterminates frog populations, presumably by feeding on juveniles [Tiberti and von Hardenberg A., 2012]. In fact, the introduction of the brook trout in other previously fishless lakes is known to be the cause of a dramatic reduction of many threatened and endangered amphibian populations [*Global invasive species database http://www.issg.org/database*]. Similarly, very few invertebrates are found in GPNP lakes with fish populations [Tiberti, 2012].

6.2.4 Brook trout

The brook trout *(Salvelinus fontinalis)* is native to North America and prefers waters with low temperatures and high oxygen content. Around 1960, several naturally fishless lakes in GPNP were stocked with brook trout by the Park management and presumably also by individual fishermen. However, stable fish populations did not survive in all stocked lakes; reproductive stable populations survived at depressed growth rates only in some of the lakes. In the lake sample analyzed here, six lakes included a fish population and six lakes were currently fishless.The brook trout has a relatively short life span (less than 5 years) and a slow growth rate, which result in populations being dominated by fish less than 30 cm in length. In the GPNP, measurements of captured brook trout indicate an average body length of 23.2 cm. The brook trout is considered an opportunistic feeder. It prefers larger prey, but feeds on a wide range of organisms including worms, leeches, beetles, crustaceans, molluscs, fishes, small amphibians, insects, showing also cannibalistic behavior [*Global invasive species database http://www.issg.org/database*].

Analysis of the stomach content of fish collected in GPNP lakes indicate that a large fraction of the diet consisted of terrestrial insects (81%), obviously available only during summer. When large zooplankton species are present, they may also constitute up to 50% of the stomach content in adult fish. The introduction of *Salvelinus fontinalis* in different lakes has been shown to result in changes in the average body size of zooplankton and in the whole plankton community structure [Boavida and Gliwicz, 1996, Knapp et al., 2001]. For GPNP lakes, there is an indication of smaller sizes of *Daphnia* gr. *longispina* and *Cyclops abyssorum* where brook trout is present Tiberti and Iacobuzio [2012]. In addition, the rare European *Daphnia* gr.

pulicaria, the largest of the cladocerans in fishless lakes, is absent in lakes with brook trout.

6.3 Model formulation

In the past, a wide variety of lake ecosystem models have been developed [Mooij et al., 2010, Jørgensen, 2010]. Few of these models, however, were specifically designed for the case of ultra-oligotrophic mountain lakes. For this reason, and in order to have full control of the model structure, we introduce here a simple model of the alpine lake ecosystems, based on rather standard choices for the relevant interaction mechanisms. An important issue, which is addressed in the present work, is the comparison between the model output and the available data on the lake ecosystem.

The model adopted here is spatially homogeneous and it describes the pelagic ecosystem dynamics in vertically mixed, shallow lakes (such as Lakes Trebecchi) or in the well-mixed epilimnion of deeper lakes such as Lake Nivolet Sup. In this case, however, the model lacks a proper description of the mixing between the upper mixed layer and the hypolimnion. This could be a problem in case the bottom sediment is an important source of nutrients (as in the case of many subalpine lakes). Due to the highly oligotrophic nature of the lakes considered here, on the other hand, nutrient input from the bottom presumably plays a minor role and vertical mixing during summer is correspondingly less important.

The model includes six compartments, describing the concentration of phosphorus (indicated by N, for nutrient), phytoplankton (P), three zooplankton compartments (Z_i, $i = 1, 2, 3$ indicating rotifers, copepods and cladocerans respectively), and fish (F). The concentration of nutrient is given in phosphorus content (measured in μmol-P L^{-1}), while the plankton and fish compartments are measured in carbon content (μmol-C L^{-1}). We then use an appropriate conversion factor, in the form of a fixed P:C ratio q, to convert from carbon to phosphorus. For simplicity, we adopt the same conversion factor for all living organisms. Test runs with different realistic P:C ratio values showed similar results.

In the model, we do not explicitly describe the dynamics of bacteria,

protozoa, macroinvertebrates and amphibians. Bacterial concentration, in particular, is assumed not to limit remineralization and recycling, constituting a large pool which reacts rapidly to the availability of organic material. In this way, the role of bacteria is parameterized in terms of nutrient remineralization.

Based on the results of the physical and chemical measurements and on the highly oligotrophic nature of these lakes, the limiting nutrient is assumed to be phosphorus, which we expect to be mostly organic and contained in living plankton cells or in detritus, or else available as dissolved or colloidal organic phosphorus [Wetzel, 2001]. As will be explained in more detail below, we assume that the phosphorus egested by living organisms as well as part of the phosphorus released upon autolysis of dead cells becomes rapidly available for consumption due to its rapid transformation into soluble, bioavailable phosphorus.

Light limitation (both in terms of insufficient or excessive light as it can happen in high mountains) is not explicitly included in the model. As shown by the Secchi depth transparency data, this is a reasonable assumption for the summer dynamics of these high–altitude mountain lakes. Data on phytoplankton composition are rather limited, but indicate that a large portion of it is composed of flagellates ranging in size between 2 and 20 μm. Due to the lack of data and for simplicity of the theoretical model, we lumped all the autotrophic phytoplankton into a single compartment.

On the other hand, we do have detailed information on zooplankton, and therefore we decided to use three different compartments of zooplankters, to allow for a quantitative comparison between model results and observations. Hereafter, the subscript P refers to phytoplankton, $1, 2, 3$ to the three zooplankton compartments and F to fish. We denote by g_P, g_i, $i = 1, 2, 3$ the growth efficiencies of the respective kinds of plankton, i.e. the fraction of ingested food (or phosphorus, for phytoplankton) used for biomass growth and reproduction. The parameters m_P, m_i, $i = 1, 2, 3$ are the linear mortality rates of phytoplankton and zooplankton respectively. Fish is assumed to feed on both macroinvertebrates and zooplankton, with a quadratic loss term $d_F \mathrm{F}^2$. A list of the model parameters and their values is given in Table 6.3.

The food web model adopted here is described by the equations

Table 6.3: Model parameters and their numerical values. GE = growth efficiency, GR= growth rate, HS= half saturation constant, MR= mortality rate, P=phytoplankton, N=phosphorus, F=fish.

Symbol	Description	Value	Units	References
V_P	optimal P uptake rate	60.0	d^{-1}	Reynolds [2006], Vadstein and Olsen [1989]
κ_P	HS for N uptake	0.5	μmol–P L^{-1}	
r_1	optimal GR for rotifers	0.80	d^{-1}	Wetzel [2001]
r_2	optimal GR for copepods	0.10	d^{-1}	Wetzel [2001]
r_3	optimal GR for cladocerans	0.05	d^{-1}	Wetzel [2001]
r_F	optimal GR for fish	0.03	d^{-1}	
ϵ_1	HS for rotifers	0.1	μmol–C L^{-1}	
ϵ_2	HS for copepods	0.02	μmol–C L^{-1}	
ϵ_3	HS for cladocerans	0.01	μmol–C L^{-1}	
ϵ_F	HS for fish	0.50	μmol–C L^{-1}	
q	P:C molar ratio	1/100	mol–P mol–C $^{-1}$	Wetzel [2001], Touratier et al. [2001], Vrede et al. [2002]
Φ	external phosphorus input	0.001	μmol–P L^{-1} d^{-1}	Wetzel [2001]
g_P	GE for P	0.45		Smith and Prairie [2004], Kragh et al. [2008]
g_1	GE for rotifers	0.60		Lyche et al. [1996]
g_2	GE for copepods	0.50		Lyche et al. [1996]
g_3	GE for cladocerans	0.60		Lyche et al. [1996]
g_F	GE for fish	0.75		Rasmussen and Ostenfeld [2000], Rasmussen et al. [2000]
m_P	P MR	1/3	d^{-1}	Wetzel [2001], Baudoux [2007]
m_1	MR for rotifers	1/20	d^{-1}	Enesco [1993], Yoshinaga et al. [2005]
m_2	MR for copepods	1/40	d^{-1}	Myers and Runge [1983], AS et al. [1995]
m_3	MR for cladocerans	1/60	d^{-1}	Nandini and Sarma [2000], Gama-Flores et al. [2007]
d_F	fish quadratic MR	0.01	$d^{-1}(\mu$mol-C $L^{-1})^{-1}$	
α	copepod preference for P	0.6		
β_M	F preference for macroinv.	0.39		
β_1	F preference for rotifers	0.01		
β_2	F preference for copepods	0.40		
β_3	F preference for cladocerans	0.20		
M	constant pool of macroinv.	1	μmol-C L^{-1}	
γ	remineralized dead biomass	0.6		

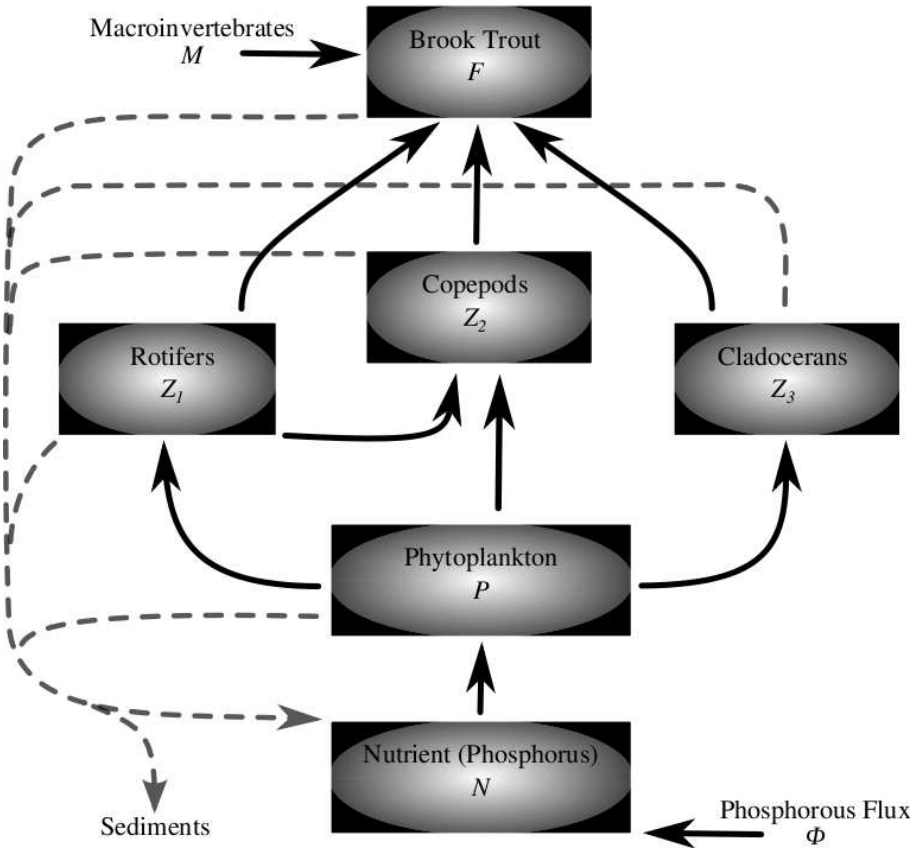

Figure 6.1: A conceptual diagram representing the model adopted here. Each box represents a model compartment, whose dynamics is described in the text. The solid arrows indicate energy and biomass fluxes which are explicitly represented in the model; dashed arrows indicate fluxes of dead and/or egested biomass which are partly recycled and partly deposited in the sediment. External inputs are the phosphorus flux Φ and the constant pool of invertebrates entering the diet of the brook trout.

(6.3.1) to (6.3.12). For the ease of interpretation, in Figure 6.1 we show a conceptual diagram of the model and of the flow of energy and biomass.

In the following subsections, we discuss the different equations of the model.

Nutrient

The dynamics of phosphorus concentration is described by

$$\frac{\mathrm{d}N}{\mathrm{d}t} = -V_P \frac{N}{\kappa_P + N} qP + q\rho + \Phi \tag{6.3.1}$$

where N denotes the concentration of bioavailable phosphorus. The first term on the right hand side describes phosphorus uptake by phytoplankton, using a Michaelis–Menten (Holling type II) functional form with parameters V_P, the maximal uptake rate, and κ_P, the half–saturation constant for phosphorus uptake. The carbon content of P is multiplied by the molar P:C ratio q to obtain the phosphorous content of phytoplankton. A fraction of the phosphorus in the ecosystem comes from rapid recycling in the water column. The term ρ, given explicitly in equation (6.3.12) discussed below, corresponds to this rapid regeneration of soluble phosphorus from egestion, excretion and secretion from algae and zooplankton and the decomposition of at least part of the dead organic matter. In the model, this contribution is added instantaneously to the N pool. The fraction of dead organic matter that is not immediately remineralized constitutes a net sink for the ecosystem biomass.

The parameter Φ is the external influx of soluble phosphorus, mainly consisting in phosphorus input by precipitation and runoff from the basin surrounding the lake and, when present, by release from the bottom sediment. For fishless lakes, this is the only external input to the ecosystem.

Phytoplankton

The equation for phytoplankton dynamics is

$$\frac{\mathrm{d}P}{\mathrm{d}t} = g_P V_P \frac{N}{\kappa_P + N} P - r_1 \frac{P^2}{\epsilon_1^2 + P^2} \mathrm{Z}_1$$

$$- r_2 G_{\mathbf{2}}(P, \mathrm{Z}_1) \frac{\alpha P}{\alpha P + (1-\alpha)\mathrm{Z}_1} \mathrm{Z}_2 - r_3 \frac{P^2}{\epsilon_3^2 + P^2} \mathrm{Z}_3 - m_P P \qquad (6.3.2)$$

where P is phytoplankton concentration. In equation (6.3.2), the first term corresponds to growth of the phytoplankton biomass by phosphorus uptake, the second, third and fourth to the loss of phytoplankton due to grazing by zooplankton and the last term represents phytoplankton mortality. This latter includes both natural mortality and the loss due to sinking of phytoplankton cells out of the euphotic layer, which in turn depends on the level of turbulence, on the stratification of the lake and on the size and shape of phytoplankton cells. Given the

poor knowledge of all these factors, which together concur in defining the value of plankton mortality, we considered it best to have just one parameter describing the loss of phytoplankton cells.

In this model, rotifers and cladocerans are assumed to consume only phytoplankton [Wetzel, 2001], and the functional form chosen for grazing is a standard Holling type III function with maximum grazing rates r_1 and r_3 and half-saturation constants ϵ_1 and ϵ_3. In principle, for filtering organisms a Holling type II (or even type I) function could have been chosen; for *Daphnia*, however, available data indicate that a Holling type III functional response is apparently observed [Sarnelle and Wilson, 2008]. In any case, the overall results discussed below do not critically depend on the functional response adopted for zooplankton.

Copepods feed on both phytoplankton and rotifers, albeit possibly with a different preference. The predation function is expressed as a Holling type III function for the preference-weighted total biomass of phytoplankton and rotifers, multiplied by a selection function that splits copepod grazing between phytoplankton and rotifers respectively [Denman, 2003]. That is, copepod grazing of phytoplankton is expressed as

$$\Pi_P(P, \mathrm{Z}_1, \mathrm{Z}_2) = r_2 G_2(P, \mathrm{Z}_1) \frac{\alpha P}{\alpha P + (1-\alpha)\mathrm{Z}_1} \mathrm{Z}_2 \tag{6.3.3}$$

where r_2 is the maximum grazing rate of copepods and the function G_2 is

$$G_2(P, \mathrm{Z}_1) = \frac{[\alpha P + (1-\alpha)\mathrm{Z}_1]^2}{\epsilon_2^2 + [\alpha P + (1-\alpha)\mathrm{Z}_1]^2} \tag{6.3.4}$$

and $0 \leq \alpha \leq 1$ is a parameter expressing the preference of copepods for phytoplankton ($\alpha = 0$ means that copepods feed only on rotifers, $\alpha = 1$ means that copepods feed only on phytoplankton).

We do not consider flagellate phagotrophy in the model. Apparently, in naturally occurring waters and especially at low substrate concentrations, as in these ultraoligotrophic lakes, algal heterotrophy is a relatively unimportant process. This is also due to the relative inefficiency of algal phagotrophy compared to the efficiency of bacterial substrate consumption [Wetzel, 2001]. Possibly, algal heterotrophy may become important under the long period of ice and snow cover,

when light intensity in the lakes is reduced.

Zooplankton

The equations for rotifer, copepod and cladoceran concentrations, Z_1, Z_2 and Z_3 respectively, are written as

$$\frac{dZ_1}{dt} = g_1 r_1 \frac{P^2}{\epsilon_1^2 + P^2} Z_1 - r_2 G_2(P, Z_1) \frac{(1-\alpha)Z_1}{\alpha P + (1-\alpha)Z_1} Z_2$$

$$- r_F G_F(M, Z_1, Z_2, Z_3) \frac{\beta_1 Z_1}{\beta_M M + \beta_1 Z_1 + \beta_2 Z_2 + \beta_3 Z_3} F - m_1 Z_1 \quad (6.3.5)$$

$$\frac{dZ_2}{dt} = g_2 r_2 G_2(P, Z_1) Z_2$$

$$- r_F G_F(M, Z_1, Z_2, Z_3) \frac{\beta_2 Z_2}{\beta_M M + \beta_1 Z_1 + \beta_2 Z_2 + \beta_3 Z_3} F - m_2 Z_2 \quad (6.3.6)$$

$$\frac{dZ_3}{dt} = g_3 r_3 \frac{P^2}{\epsilon_3^2 + P^2} Z_3$$

$$- r_F G_F(M, Z_1, Z_2, Z_3) \frac{\beta_3 Z_3}{\beta_M M + \beta_1 Z_1 + \beta_2 Z_2 + \beta_3 Z_3} F - m_3 Z_3 \quad (6.3.7)$$

In eq. (6.3.5), we model rotifer predation on phytoplankton through the first term, while the loss terms are due to predation by copepods and fish and to natural mortality, and are represented by the last three terms. Copepod predation on rotifers is expressed as

$$\Pi_1(P, Z_1, Z_2) = r_2 G_2(P, Z_1) \frac{(1-\alpha)Z_1}{\alpha P + (1-\alpha)Z_1} Z_2 \quad (6.3.8)$$

and the total grazing of copepods is given by the sum $\Pi_P + \Pi_1$, as expressed in the first term of eq. (6.3.6) for the copepod density. The second term in this equation is copepod loss due to fish predation and the third term is natural linear mortality. In eq. (6.3.7) for cladocerans, the first term is grazing on phytoplankton, the second term is loss due to fish predation and the third term is natural linear mortality.

The form for fish predation is analogous to that used for copepods and its structure is determined by the fact that fish feed on macroinvertebrates and insects, whose fixed concentration is given by M, and

on the three compartments of zooplankton. For each compartment, fish predation is expressed by a Holling type III form for the total preference-weighted biomass,

$$G_F(M, \mathrm{Z}_1, \mathrm{Z}_2, \mathrm{Z}_3) = \frac{(\beta_M M + \beta_1 \mathrm{Z}_1 + \beta_2 \mathrm{Z}_2 + \beta_3 \mathrm{Z}_3)^2}{\epsilon_F^2 + (\beta_M M + \beta_1 \mathrm{Z}_1 + \beta_2 \mathrm{Z}_2 + \beta_3 \mathrm{Z}_3)^2} \qquad (6.3.9)$$

where the parameters β_j indicate fish preference for the j-th compartment; we impose $\beta_M + \beta_1 + \beta_2 + \beta_3 = 1$. The parameters r_F and ϵ_F^2 are the maximum grazing rate and half-saturation constant for fish.

Brook trout

We assume that *Salvelinus fontinalis* feeds on macroinvertebrates, insects and zooplankton. We do not explicitly describe the dynamics of macroinvertebrates and assume instead a constant pool of macroinvertebrate and insect biomass at a fixed carbon concentration M. Fish biomass dynamics is assumed to follow the equation

$$\frac{\mathrm{dF}}{\mathrm{d}t} = r_F g_F G_F(M, \mathrm{Z}_1, \mathrm{Z}_2, \mathrm{Z}_3)\mathrm{F} - d_F \mathrm{F}^2 \qquad (6.3.10)$$

where G_F is given by eq.(6.3.9). The feeding term in the above equation comes from the sum of the feeding terms for all compartments. For the fish mortality, a quadratic term is used to close the system and to qualitatively represent fish feeding on juvenile fish. The choice of a quadratic mortality term for the highest trophic level in a model ecosystem is rather standard and the reason for it is the following. A quadratic mortality term allows for the existence of stationary equilibria with non-zero densities in the model system. This would not be the case in the presence of a linear loss term [Steele and Henderson, 1992]. In our specific case, the quadratic mortality term for the fish population also allows for a stationary fish population feeding on invertebrates: in the absence of zooplankton, the fish density obeys a logistic equation,

$$\frac{\mathrm{dF}}{\mathrm{d}t} = g_F c_F \mathrm{F} - d_F \mathrm{F}^2 \ , \qquad (6.3.11)$$

where $c_F = r_F \beta_M^2 M^2/(\epsilon_F^2 + \beta_M^2 M^2)$ is a constant parameter.

Direct phosphorus recycling

The fraction of food that is not used for biomass growth enters the metabolism of the consumer/predator. This biomass is then egested (i.e. respired, excreted, or secreted from the body surface). The phosphorus thus released is assumed to be soluble phosphorus [Wetzel, 2001, Touratier et al., 2001] and is rapidly released due to bacterial and enzymatic activity [Olsen et al., 1986, Uehlinger, 1986, Lyche et al., 1996].

Likewise, due to the same kinds of activity, soluble reactive phosphorus is immediately released following autolysis of dead organisms [Olsen et al., 1986, Uehlinger, 1986, Lyche et al., 1996]. Particulate detritus in the form of dead algae and zooplankton rapidly (within hours or days) loses most of its phosphorus content in the form of orthophosphate and organic phosphorus, which is subsequently remineralized. The remaining part of the phosphorus contained in particulate detritus is lost as it sinks into the bottom sediment [Wetzel, 2001, Lyche et al., 1996]. The term $q\rho$ in eq.(6.3.1), where q is the P:C ratio of living organisms (taken for simplicity to be the same for all organisms), represents the phosphorus that is instantaneously recycled. The term ρ is given by

$$\begin{aligned}\rho = (1-g_P)V_P\frac{N}{\kappa_P+N}P + (1-g_1)r_1\frac{P^2}{\epsilon_1^2+P^2}\ \mathrm{Z}_1 \\ +(1-g_2)r_2G_2(P,\mathrm{Z}_1)\mathrm{Z}_2 + (1-g_3)r_3\frac{P^2}{\epsilon_3^2+P^2}\mathrm{Z}_3 \\ +(1-g_F)r_FG_F(M,\mathrm{Z}_1,\mathrm{Z}_2,\mathrm{Z}_3)\mathrm{F} \\ +\gamma\left(m_P\mathrm{P}+\sum_{i=1}^{3}m_i\mathrm{Z}_i+d_Fq_F\mathrm{F}^2\right)\end{aligned} \tag{6.3.12}$$

where $1-g_P$, $1-g_i$, $1-g_F$ indicate the fractions of resource/prey which are used for metabolism and $0 \le \gamma \le 1$ is a parameter which fixes the fraction of dead organic matter that is rapidly remineralized before being buried in the sediment. The term $(1-\gamma)\left(m_P\mathrm{P}+\sum_{i=1}^{3}m_i\mathrm{Z}_i+d_Fq_F\mathrm{F}^2\right)$ gives the only net sink of biomass and phosphorus of this ecosystem.

Parameter values

As in any ecosystem model, the determination of parameter values is a difficult issue, especially because the ecosystem compartments used in the model lump together different species and/or different life stages, which can have rather different feeding behaviors and mortality rates.

Some of the parameters in the model have been obtained from published values and the relevant references are reported in the Table 6.3. In particular, there are estimates of the uptake parameters V_P and κ_P for phytoplankton, of the growth efficiencies and natural mortalities of plankton and of the average nutrient input in oligotrophic lakes.

However, other parameters have to be determined heuristically. The preference of copepods for phytoplankton and rotifers, as well as the preference of fish for macroinvertebrates and zooplankton, have been fixed based on general consideration related to size preference. We have assumed that fish has a higher preference for macroinvertebrates (which constitute a large part of their summer diet) and for the larger zooplankton, and a lower preference for rotifers, which are much smaller. As for copepods, we have assumed a slightly higher preference for phytoplankton than for rotifers. Similarly, the quadratic mortality rate and the Holling type III parameters for fish, and the fraction of dead biomass which is rapidly remineralized have been determined heuristically.

As we discuss below, the values of some of these parameters is relatively unimportant, while the model results are more sensitive to the assumed values of other parameters.

6.4 Results

The model equations (6.3.1)–(6.3.12) are integrated in time using a fourth order Runge–Kutta method with a time step of 0.01 days. A full exploration of the phase-space and parameter-space behavior of system (6.3.1)–(6.3.12) is beyond the scope of this work; for this reason, in this section we consider a few selected sets of parameter values, compare the model output to the measured data, and discuss some of the most interesting parameter dependencies.

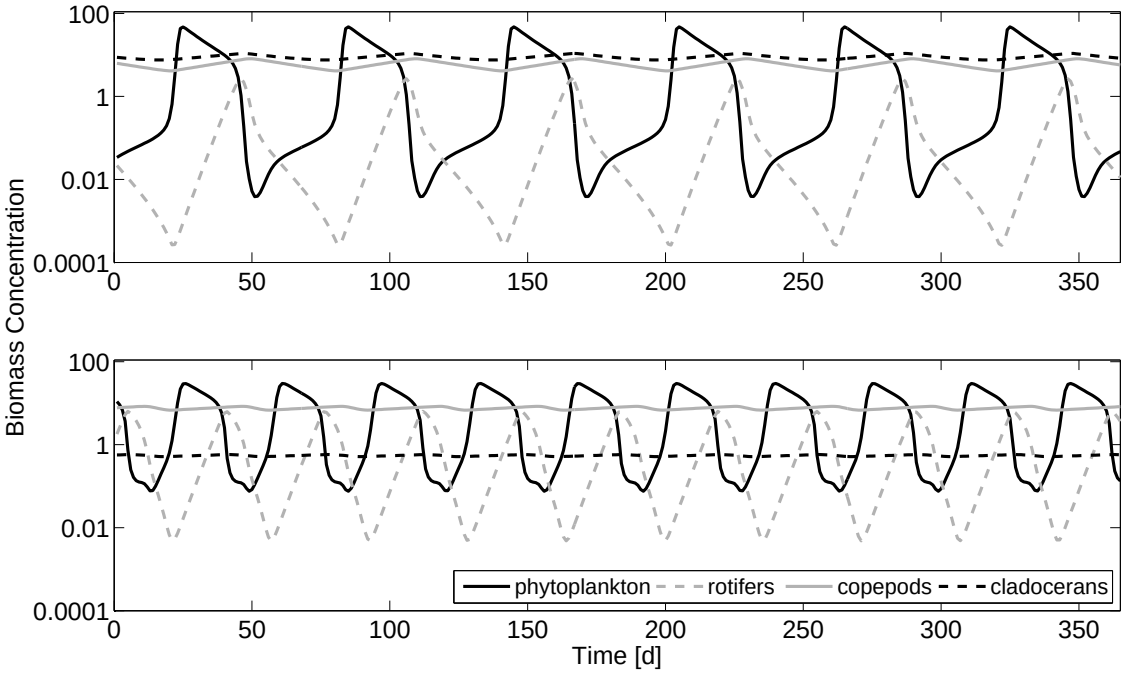

Figure 6.2: Upper panel: temporal dynamics of the five-compartment ecosystem for a fishless lake. Lower panel: same as above but for lake with fish. Biomass concentrations are reported on logarithmic scale.

6.4.1 Lakes without fish

We first consider the case without fish, i.e., $F = 0$. As a preliminary step, it is interesting to study the behavior of the model in simplified cases, for example, when some of the compartments are initially set to zero. The model is built in such a way that if phytoplankton or any of the zooplankton compartments are initially zero, they stay zero. When zooplankton is absent, with the parameter values reported in Table 6.3 the system tends to a stable stationary equilibrium determined by the value of the phosphorus input rate, Φ.

When only rotifers are added, the system still converges to a stable equilibrium of the nutrient-phytoplankton-rotifer model. On the other hand, when copepods are added instead of rotifers (that is, a zooplankton compartment with different parameter values), the stationary state becomes unstable and the system undergoes limit cycle oscillations. A similar situation is observed when only cladocerans are added. In these cases, phytoplankton density periodically gets very close to zero and its average value is typically lower than in the case where no consumers are present. When all three compartments of zoo-

Table 6.4: Minimum, maximum and average total phosphorus (TP), phytoplankton, and zooplankton biomass in six fishless lakes of the Gran Paradiso National Park. For each compartment, we report the observed values (bold) and the model output (italic). Phosphorus is given in μg-P L^{-1}, biomass in μg-C L^{-1}. Chlorophyll–*a* was converted to carbon of autotrophic phytoplankton using a factor of 50.

[μg L^{-1}]	Min.	Max.	Average
TP	**1**	**13**	**4**
TP	*0.9*	*1.94*	*1.34*
Chl–a ($\times$50)	**7.5**	**61.5**	**27.4**
Phytoplankton	3.8×10^{-3}	*47.7*	*8.19*
Rotifers	**0**	**1.4**	**0.06**
Rotifers	2.5×10^{-4}	*2.68*	*0.27*
Copepods	**0.2**	**96.9**	**9.1**
Copepods	*4.1*	*8.1*	*5.9*
Cladocerans	**0.03**	**129.6**	**5.8**
Cladocerans	*7.6*	*10.9*	*8.9*

plankton are included, the system undergoes limit-cycle oscillations. The upper panel of Figure 6.2 shows the temporal dynamics of the full five-compartment ecosystem for a fishless lake. The black solid line is for phytoplankton, the grey dashed line is for rotifers, the grey solid line is for copepods and the black dashed line is for cladocerans. In this figure, and in the tables discussed below (Table 6.4, 6.5), we indicate plankton abundance in μg-C L^{-1}, using the appropriate atomic weights for conversion to provide a direct comparison with the measured data.

Minimum, maximum and average values of total phosphorus and plankton biomass are reported in Table 6.4. Note that plankton biomass is given in μg-C L^{-1}, while phosphorus is given in μg-P L^{-1}. The carbon content of the plankton was computed using the molar P:C ratio in Table 6.3.

Notice that the range of variability of the model output and that of the measurements have been computed in different ways. For the data, we indicated the range of individual measurements, which were taken twice a year in different years and in different lakes. For the model, the variability comes from the temporal variability of the model solution for a given set of parameter values. In principle, if all lakes had the same characteristics and the same ecosystem composition, with no inter-annual variability, in the limit of many measurements the two approaches could provide the same information. In reality,

Table 6.5: Minimum, maximum and average total phosphorus (TP), phytoplankton, and zooplankton biomass in six lakes with fish of the Gran Paradiso National Park. For each compartment, we report the observed values (bold) and the model output (italic). Phosphorus is given in μg-P L^{-1}, biomasses in μg-C L^{-1}. Chlorophyll–*a* was converted to carbon of autotrophic phytoplankton using a factor of 50. TP does not include the phosphorus in the fish population.

[μg L^{-1}]	Min.	Max.	Average
TP	**1**	**13**	**4**
TP	*0.76*	*1.30*	*0.99*
Chl–a ($\times$50)	**13.5**	**53.5**	**25.2**
Phytoplankton	7.5×10^{-2}	*30.0*	*8.9*
Rotifers	**0**	**16.8**	**1.9**
Rotifers	4.8×10^{-3}	*6.37*	*1.27*
Copepods	**0**	**12.1**	**2.3**
Copepods	*6.80*	*8.37*	*7.57*
Cladocerans	**0**	**0.9**	**0.08**
Cladocerans	*0.52*	*0.58*	*0.55*

there are several differences between the individual lakes, as well as the possibility of significant inter-annual fluctuations. For this reason, the comparison between the two ranges of variability should be considered only at the order-of-magnitude level.

The values reported in Table 6.4 show that there is a general agreement between the model results and the observations. The modeled total phosphorus is smaller than in the data, and it shows a more limited variability compared to the data. Phytoplankton abundance has similar values in the model and the data, although the model periodically generates very small phytoplankton densities compared to the data.

Rotifers, copepods and cladocerans display similar values in the data and in the model, although model rotifers tend to have larger abundance than in the data and the average cladoceran abundance in the model is larger than that of copepods. Both copepods and cladocerans tend to display much less variability in the model than in the data.

6.4.2 Impact of *Salvelinus fontinalis*

The introduction of brook trout induces several effects on the lake ecosystem, as shown by the data collected in GPNP lakes. In particular, relative abundances and average sizes of different zooplankton

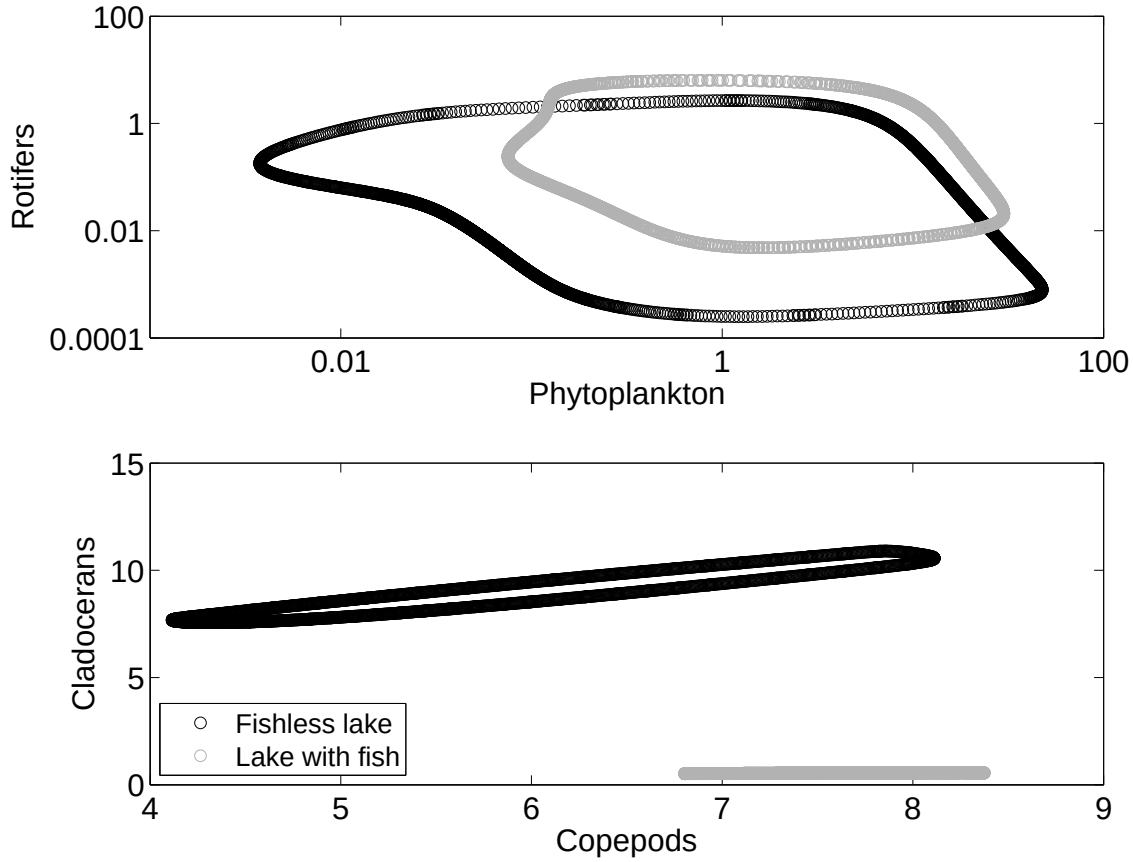

Figure 6.3: Upper panel: System dynamics in the phase plane defined by the phytoplankton and rotifer abundance (in logarithmic scale) for a fishless case (black circles) and for a lake with fish (gray circles). Lower panel: same as above for the phase plane defined by the copepod and cladoceran abundance (in linear scale).

compartments are modified by the presence of fish. To theoretically study the effect of fish introduction we adopt the same parameter values used for fishless lakes and introduce, in the model ecosystem, the action of brook trout. The lower panel of Figure 6.2 shows the temporal dynamics of phytoplankton and zooplankton for a case where fish is present. Minimum, maximum and average biomasses of phytoplankton and zooplankton are reported in Table 6.5.

The results obtained for lakes with fish agree with the data in showing a decreased biomass of the cladocerans and an increased concentration of rotifers compared to the fishless lakes. Agreement is also found in the (somehow counter-intuitive) absence of major differences in the phytoplankton biomass in lakes with and without fish. Figure 6.3 shows the dynamics of the two ecosystems, with and without fish, in the phase plane defined by phytoplankton and rotifer abundance.

6.4.3 Sensitivity to parameter variations

Changing the values of some parameters leads to minor, quantitative changes in model output, while variations in other parameters may induce more significant changes in the model behavior. A complete study of the system dynamics in the full parameter space is beyond reach and, probably, not particularly enlightening. Here, we provide a few hints on how the various parameters affect the system behavior when varied individually, with a specific focus on those parameters which can vary owing to changes in water temperature or to environmental modifications.

The value of the phosphorus input Φ can be decreased by a factor of ten or increased by a factor of two without affecting the qualitative behavior of the system. Further increase in the value of Φ can lead to the disappearance of the rotifer population, favoring the cladoceran population.

The value of the optimal uptake rate of phytoplankton, V_P, can be changed in the range 20-200 d^{-1} without qualitative changes in the system behavior. Decreasing the value of the phytoplankton uptake rate below 20 d^{-1} leads to the disappearance of the cladoceran population. By taking a small value $V_P = 1$ d^{-1} and increasing the phosphorus input by a factor of ten, one obtains again a system with the three coexisting compartments of zooplankton, but in this case phytoplankton abundances is about an order of magnitude higher than the observations.

The system dynamics is rather sensitive to the zooplankton and fish maximal feeding rates and half-saturation constants. Significant variations of some of these parameters lead to the disappearance of one or two zooplankton compartments. This behavior is due to the narrow limits on the range where coexistence of the three competing compartments seems to be possible. If the grazing rate of fish is too large, all zooplankton disappear.

The copepod preference for phytoplankton, α, can be increased without qualitative changes in the ecosystem dynamics. However, decreasing α at values of 0.5 and less leads, with the parameter values adopted here, to the disappearance of rotifers.

The preferences of fish for the various zooplankton and macroinvertebrate compartments are difficult to determine from field data,

and the values of $\beta_i (i = M, 1, 2, 3)$ remain as heuristic parameters. Increasing fish preference for the constant pool of macroinvertebrates, β_M, leads to a larger fish population and to the possible disappearance of some (or all) zooplankton compartments owing to higher fish predation. On the other hand, decreasing the parameter β_M down to zero (while keeping the other preferences roughly in the same ratios) does not qualitatively change the results.

By increasing fish preference for rotifers up to 0.2 and above, no significant changes in the results are found. However, cladocerans are quite sensitive to fish predation. Increasing the fish preference for cladocerans (here fixed at the rather low value $\beta_3 = 0.2$) leads to the disappearance of cladocerans. This is consistent with the fact that very few (if any) cladocerans are observed in lakes with fish. In these cases, if fish predation on copepods is not intense enough also the rotifer population disappears, owing to competition with copepods and predation by the copepods themselves.

6.5 Discussion

In this work we discussed measurements of the main characteristics of twelve oligotrophic to ultra-oligotrophic alpine lake ecosystems in the Gran Paradiso National Park, northwestern Italy. The lakes, all above an altitude of 2000 meters a.s.l., are far from direct sources of pollution. Half of the lakes do not have a fish population while the other six lakes host populations of an introduced allochthonous fish species, the brook trout (*Salvelinus fontinalis*).

We then introduced a simplified model of oligotrophic to ultra-oligotrophic high-altitude lake ecosystems, which describes the temporal evolution of bioavailable phosphorus, phytoplankton, three compartments of zooplankton, and fish. The availability of repeated measurements of phosphorus content, chlorophyll–*a* and zooplankton abundance (distinguishing between rotifers, copepods and cladocerans) allowed for the comparison between model output and observations.

Although some discrepancies between model results and measured data were detected, the model outputs reproduced remarkably well many of the main properties of the measured data. A more precise fit between model and data could be obtained by fine tuning the free

parameters of the model; however, we think that this exercise is of little interest given the simplified nature of the model adopted here and the many processes which have been discarded, such as the temporal variability in the composition of the different plankton compartments. Also, we have adopted a vertically homogeneous, single-layer model which properly describes the dynamics of fully mixed (shallow) lakes such as Lake Trebecchi Sup., but could miss processes associated with vertical mixing in lakes with a summer thermocline, such as Lake Nivolet Sup. Although the role of vertical mixing is probably minor for these lakes, as the bottom sediment is rather poor in nutrients, some of the discrepancies between model results and measured data could be due to the vertical homogeneity assumed in the model.

Using the simplified model, we studied the effects of introducing an allochthonous fish species in a pristine alpine lake, and we compared the model predictions with data. In principle, building upon classic results on trophic control [Hairston et al., 1960], the expected effects of the introduction of *Salvelinus fontinalis* are: 1) a decrease of the biomass of the larger zooplankton (cladocerans and copepods) due to fish predation; 2) top-down effects on rotifers, which might increase their biomass due to the fish predation on large zooplankton and the reduction in the competition with cladocerans. It is more difficult to have clear expectations on the reaction of phytoplankton to introduced fish: for example, one could expect a beneficial effect on phytoplankton owing to the decreased grazing by cladocerans and, possibly, the larger amount of phosphorus regenerated from fish metabolism.

The measurements performed on zooplankton in the GPNP alpine lakes indicated both a smaller biomass (Tabs. 6.4, 6.5) and a smaller average size (Table 6.2) of cladocerans and of copepods, and an increased biomass of rotifers. In addition, as reported in Table 6.2, there was a redistribution of biomass on the different species of cladocerans with some completely absent in the lakes stocked with *S. fontinalis*. The phytoplankton appeared not to change significantly.

The introduction of fish in the model, keeping all other parameters unchanged, induced definite and significant changes in the model ecosystem which fully parallel those observed in GPNP lakes where fish was introduced. Due to the way we have implemented our model, we could not observe morphological changes or vertical migration, but

we did observe all the other expected effects, at least qualitatively, in the simulation. Because we kept all parameters fixed when adding fish, the simulation with fish and the numerical values of the final biomasses did not totally agree with the data, but the effect of *S. fontinalis* in the model was qualitatively the same as the one observed in lakes stocked with fish (i.e. a decrease in the biomass of the larger zooplankton and an increase in the biomass of the rotifer population). The results also indicate that the average phytoplankton abundance remains practically unaffected by fish introduction, as grazing by cladocerans is substituted by grazing by rotifers. We also saw a redistribution in the proportions of phosphorus retained by the various compartments, detailed in paragraph 6.4.2.

Clearly, the model introduced here can be ameliorated in several ways. A potentially important aspect is to introduce, albeit in a simplified way, the vertical stratification of the water column, taking into account vertical mixing. A second aspect is related to the lack of a detritus compartment. In highly oligotrophic lakes such as those considered here, for simplicity we opted for discarding slow phosphorus recycling in the bottom sediment, dividing the dead and egested biomass into a fraction that is immediately recycled in the water column and a part that is lost to the sediment and recycled much more slowly, possibly during winter. This aspect of the model could certainly be improved. More importantly, the nutrient input into the system is presumably very intermittent, being associated with spring snowmelt and individual precipitation events, but since data on the temporal variability of nutrient input are missing, it would be difficult to reconstruct the seasonal dynamics, and any attempt at doing so would bring more uncertainty into our model. For this reason, we chose to simplify the model and use a constant nutrient input. In any case, the results reported here confirm that even simple models composed of few compartments do have a useful role in the description and understanding of natural ecosystem dynamics, providing an important tool to assess the possible impact of environmental and/or climatic changes on alpine lake ecosystems.

Chapter 7

Ocean Dynamics in Greenland Fjords: Theoretical background

Recent data (Fig.7.1) have shown an increased mass loss from the Greenland ice sheet which have influenced Greenland contribution to sea-level rise. Over half of the loss is attributed to an increased ice

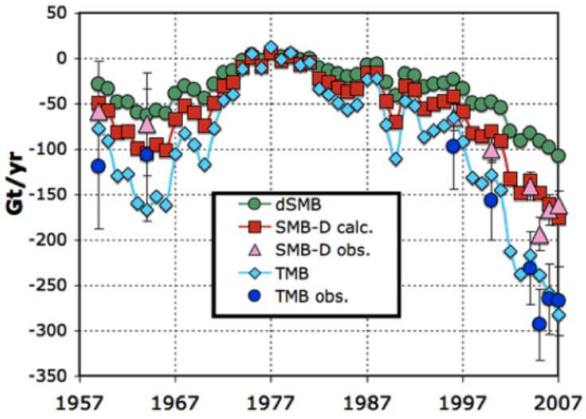

Figure 7.1: Total ice-sheet mass balance form 1957-2007. Interpolated: light blue diamonds, observed: blu circles. Surface mass balance anomalies: green circles. Surface mass balance interpolated (red squares) and observed (pink triangles) Rignot et al. [2008]

discharge due to the the acceleration of outlet glaciers from western and southeast Greenland (Rignot and Kanagaratnam [2006], van den Broeke et al. [2009]). The dynamic thinning of the glaciers is a highly non-linear and poorly understood process. It is absent from climate models and considered the largest source of uncertainty for sea-level rise predictions for the 21^{st} century (IPCC 2007).
Outlet glaciers terminate in deep narrow fjords that connect the glacier

to the ocean. These fjords are filled with shelf waters and are influenced by its dynamics.
One possible cause for the recent acceleration is due to increased submarine melting caused by warming of waters around Greenland.
The interaction between the ocean and Greenland ice sheet can be studied at different scales all having an impact on the submarine melting and its variability.
Starting with the currents around Greenland $\mathcal{O}(1000km)$, going down to the shelf dynamics $\mathcal{O}(200km)$ and to the fjord scale $\mathcal{O}(100km)$. Ultimately the submarine melting is influenced by small scale processes at the ice-ocean boundary $\mathcal{O}(10m)$. This chapter is an overview of the dynamics at different scales.

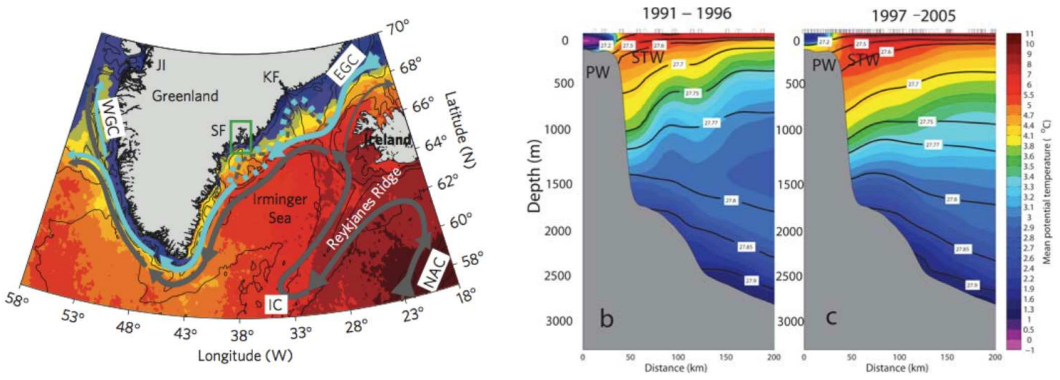

Figure 7.2: (a) Currents around Greenland. (b) Mean summer potential temperature section in south east Greenland. (Courtesy of k. Väge)

Figure 7.2(a) shows the system of currents around Greenland. Two main water masses reach Greenland: the polar and subtropical waters. The cold and relatively fresh polar waters (PW) are transported by the east and west Greenland currents (EGC,WGC). Unlike Antartica, thanks to its topography, warm and salty waters of subtropical origin (STW) can reach Greenland. A topographically stretched branch of the North Atlantic Current (NAC), the Irminger current, brings these waters towards Greenland.
Following the mid 1990's the STW have been accumulating on the ocean shelf (Fig.7.2(b)) and shelf waters have been warming (Holland et al. [2008], Motyka et al. [2011]), which empirically support the idea that Greenland mass loss might have been triggered by the ocean.

To better understand the dynamics of Greenland outlet glaciers I will consider in this introduction and in the following chapter, Helheim

Figure 7.3: Satellite image of Sermilk fjord

Glacier and Sermilik fjord in south-east Greenland.
Sermilik (Fig.7.3) $(66°N, 38°W)$ is a is a U-shaped narrow (6 km) fjord, 100 km long and 900 m deep not strongly influenced by rotation.

Submarine melting is associated with a transport of heat to the glacier and depend both on the temperature and on the circulation at the ice-edge. The leading paradigm for tidewater glaciers is that the heat transporting circulation is 'estuarine', characterized by subglacial discharge at depth.
It is driven by a rising plume of subglacial discharge and meltwater. Entrainment of ambient waters by the plume draws deep waters towards the glacier and drives a fresh outflow at the surface (Fig. 7.4(a)). The estimated melt rates is controlled by the temperature of the deep fjord waters and the subglacial discharge. This paradigm is based on observations from one Alaskan tidewater glacier with a shallow sill which is dynamically equivalent to the problem of forced convection in a homogeneous ocean.
However this is true in unstratified waters and recent surveys have shown that Greenland's fjords are filled with two water masses, STW and PW (Straneo et al. [2010]). Theoretical, laboratory studies (Huppert and Josberger [1980], Huppert and Turner [1980]) and data (Straneo et al. [2011]) have shown that in stratified water a more complex circulation arises (7.4(b)). The latter is characterized by an export of meltwater at surface but also at the interface between the two water masses with a consequent inflow of ambient water at the bottom of

the fjord but also at a shallower depth.
This arise the possibility that the melting is driven by more than one water mass and the the circulation is influenced by the density contrast.

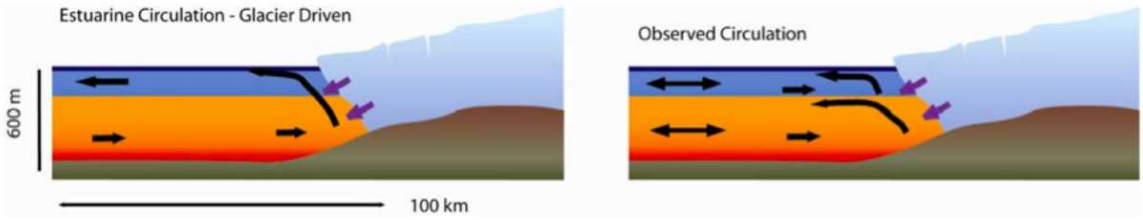

Figure 7.4: Schematic of the circulation in Greenland's glacier fjords. (a) Estuarine circulation, (b) observed circulation including multiple overturning cells Straneo et al. [2011]

Furthermore Greenland's fjords are characterized by vigorous shelf-ford exchange (Straneo et al. [2010]) and fast tidal to subtidal baroclinic flows (Straneo et al. [2011], Mortensen et al. [2011]) which likely contribute to the heat transport to the glacier. Recent measurement in Sermilik fjord have shown evidence of a fast, strongly sheared intermediary-circulation, driven by upwelling/downwelling on the shelf as a result of passing storms.
These circulations are typical of deep, narrow fjords and cause the renewal of fjord waters by shelf waters. The implication is that the heat to the glacier might be modulated by the number and frequency of weather systems in the region. Strongly sheared and variable flows were also observed near Helheim Glacier. These flows are likely internal modes (i.e. seiches) which are common in deep fjords. However, at present, it is unclear how these different circulations contribute to the transport of heat to the glacier.
Thus, the submarine melt rate of Greenland's outlet glacier is likely to depend on more complex oceanic processes and parameters (including externally forced circulations and water masses distribution on the shelf) than ambient water temperatures alone.

Ambient water properties in Greenland's fjords must be, ultimately, controlled by the properties on the shelf and their variability. In south-east Greenland the shelf is 100-300km wide, and around 300m deep, with deep troughs running across it. Its properties are dominated by cold fresh PW and farther offshore warm salty STW waters are carried

along the continental slope.
The spatial separation of PW and STW is true only in the mean while intrusion of STW are observed in summer (Pickart et al. [2005], Sutherland and Pickart [2008]) and winter (Straneo et al. [2010]). The mechanisms that control such intrusions are unknown but they might be generated by instability of the slope currents and topographic steering by the deep troughs. Such channels are common to many major fjord/glacier systems in Greenland since they are formed by the erosion during expanded Ice Age ice sheet. Warm intrusions on the shelf, such as those visible in figure 7.2(b), were also observed in regional simulations (Haine et al. [2009], Magaldi et al. [2011]). The mid-1990's warming together with the periodic intrusion of STW in the shelf are likely to be an important factor in the shelf/fjord dynamics and in the ocean triggered submarine melting.
The high winds occurring over south east Greenland continental shelf are also a potential factor. Specifically events like, barrier and katabatic winds, generated by the interaction of transiting synoptic low pressure systems with Greenland's orography (Moore and Renfrew [2005], Klein and Heinemann [2002]).

Ultimately the submarine melt rate is controlled by the dynamics of the rising plume in the ice-ocean interface and by the thermodynamics processes at the boundary layer. The starting point to model the dynamics at the ice edge is the theory of buoyant plume which was largely developed by Turner (Turner [1986]). The key feature of buoyant plumes is that the volume flux grows with height through the entrainment of the surrounding fluid. Turner studies started from the assumption that the entrainment rate at any height is proportional to the vertical velocity at that height (Morton et al. [1956]).
Ellison et al. Ellison and Turner [1959] showed that the same concept could be applied to buoyant flows that follow an inclined surface. The main modifications to the theory of Turner are that the buoyancy forcing is determined by the component of gravity parallel to the surface, which is also a source of drag, and that while the entrainment rate remains proportional to the velocity, the latter is no longer constant but determined by the stability of the flow, generally expressed as a function of the bulk Richardson number. This theory has been applied to many geophysical flows including, powder snow avalanches,

katabatic winds, overflows and turbidity currents. In many of these cases the density difference driving the flow is determined not only by the stratification of the environment but also by the interaction of the flow with the surface.
MacAyeal et al. MacAyeal and Jacobs [1985] applied the model to the overturning circulation beneath ice shelves, where the interaction between the plume and the surface and the consequent phase changes are the source of buoyancy.
The applicability of these models to Greenland's fjords is limited by two factors. The first is that the initial buoyancy flux due, for example, to the subglacial runoff, dominates over the generated melting. The second limiting factor is that rotation should play a minor role in the dynamics, which is true in narrow Greenland's fjords.
The only other constrain that need to be satisfied in order to apply these plume models is that the Reynolds number of the plume is large enough for the plume to be turbulent.
To satisfy the last condition, some analogies can be drawn between the ice melting dynamics and that of the thermal convection of a vertical heated plate. Wells et al. Wells and Worster [2008] has discussed the height at which a fully turbulent plume forms from the initial sheared boundary layer.

The last process that needs to be included to fully describe the dynamics of Greenland's fjord and, in fact, is the only direct interaction between the glacier and the ocean is the thermodynamics of the heat and mass exchange.
Turbulent mixing is the crucial process which control the phase changes and therefore the mass balance of the ice and the buoyancy forcing that drives the fjord circulation. At present, there have been no observations of turbulent transfer coefficients in the oceanic boundary layer beneath ice shelf or close to glaciers. Thus, models (Holland and Jenkins [1999]) use observations and the extensive literature (McPhee [2008]) of the turbulent boundary layer beneath sea ice to parametrize the thermodynamic interactions.
The turbulent ice-ocean boundary layer (Fig. 7.5) can be conceptually divided into two regions: the surface layer, typically a meter thick, where the turbulent mixing is influenced by the boundary and the outer layer, which typically extends over a few tens of meters,

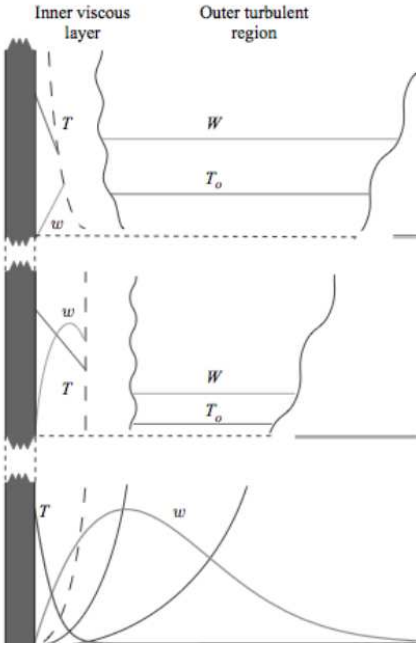

Figure 7.5: Schematic of the turbulent ice-ocean boundary layer

there the turbulence is unaffected by the boundary and rotation and stratification control the mixing.
In an interfacial sublayer, within the surface layer, the transfer of momentum is due predominantly to molecular viscosity and direct interaction of the flow with surface roughness, and it occupies the few millimetres up to centimetres closest to the ice-ocean interface. Seawater has a high Prandtl number and a very high Schmidt number, so a large part of the temperature and salinity changes between the interface and the far field occur over the interfacial sublayer, resulting in a relatively uniform scalar concentration beyond the sublayer and frequently the formation of a distinct mixed layer. As a consequence, the expressions for scalar transfer through the ice-ocean boundary layer tend to be dominated by the parametrization of the interfacial sublayer and show little sensitivity to the treatment of the mixing in the rest of the surface and outer layers (McPhee et al. [1987]).
To estimate the properties of the turbulent transfer oceanic boundary is necessary to consider the heat balance at the interface (eq. 7.0.1) and the consequent ablation rate.

$$\rho_i a_b L_i = \rho_i c_i k_i \frac{\partial T_i}{\partial z} - \rho_w c_w u_* \Gamma_T [T_f(S_b, P_b) - T_w] \tag{7.0.1}$$

The ablation rate at the ice ocean boundary a_b, is expressed as a change in the thickness of the solid ice per unit time. The first term on the right-hand side is the conductive heat flux into the ice, while the second term represents the turbulent heat flux through the oceanic boundary layer.
The heat flux is expressed as the product of the interfacial frictional velocity u_*, a dimensionless, turbulent transfer coefficient for heat, Γ_T, and the difference in temperature between the ice-ocean interface and the outer edge of the boundary layer. The frictional velocity is the square root of the kinematic stress at the ice-ocean interface and is normally assumed to be related to the freestream current beyond the boundary layer U through a quadratic drag law,

$$u_*^2 = C_d U^2 \tag{7.0.2}$$

where C_d is a dimensionless drag coefficient.
The interfacial salinity in eq. 7.0.1, S_b is obtained from consideration of the salt balance at the phase change interface,

$$\rho_i a_b (S_b - S_i) = -\rho_w u_* \Gamma_S (S_b - S_w) \tag{7.0.3}$$

where the diffusive salt flux in the ice is zero and the salinity of the ice S_i is generally taken to be zero.
The turbulent transfer coefficient for salt Γ_S is much smaller than the equivalent coefficient for heat because of the dominant role played by molecular diffusion within the interfacial sublayer.
While most of the terms in the above equations are either physical constant or properties of water and ice that can be easily observed, the same cannot be said of the drag coefficient and the turbulent transfer coefficients which represent simple parametrizations of the effects of turbulence in the boundary layer.
Various approaches to the specification of the turbulent transfer coefficients have been followed. The simplest Determan and Gerdes [1994] consider only heat transfer and made the implicit assumption that the far-field velocity was constant. Hellmer et al. Hellmer and Olbers [1989] and Scheduikat et al. Scheduikat and Olbers [1990] considered both heat and salt transfer but made the same implicit assumption of

constant velocity. Jenkins et al. Jenkins [1991] also considered both heat and salt transfer but introduced a velocity dependence into the expression for the turbulent heat and salt fluxes.
To derive the expression for the turbulent transfer velocities, in absence of any knowledge of ice roughness, the ice is considered as hydraulically smooth.
The velocity formulation was based on the laboratory studies of Kader et al. Kader and Yaglom [1972, 1977] and has been widely used to model the interaction between the ice and the ocean. Holland et al. Holland and Jenkins [1999] showed that the application of this laboratory parametrization yields to similar results of those produced by more complex parametrization that includes the effects of both rotation and stabilizing buoyancy flux caused by freshwater (McPhee et al. [1987]).
The insensitivity to the parametrization of mixing beyond the interfacial sublayer is due to the dominance of molecular diffusion within the sublayer in setting the overall heat and salt differences across the boundary layer.
At present, the work of Jenkins et al. Jenkins et al. [2010] is the most comprehensive study done to determine the turbulent transfer coefficients beneath ice shelf. Using direct measurements of basal ablation of Ronne Ice Shelf in Antartica, different parametrization of the turbulent transfer are tested. The results showed that, when using a parametrization that explicitly includes the effects of ocean currents, the estimated ablations rates agree with the observations. This study provide also an estimate for $C_d^{1/2}\Gamma_T$ and $C_d^{1/2}\Gamma_S$ which can be applied to other ice-ocean boundaries such as those of Greenland's tidewater glaciers.
One of the question that arises is which is the dominant ocean velocity influencing the turbulent transfer. In Greenland many dynamical processes take place, the rising plume at the ice edge, the fjord's circulation, the tide and the wind events on the shelf. The velocities in these cases are several orders of magnitude different and one of the challenges in modelling ice melting dynamics is the correct parametrization of the velocity in the turbulent transfer.

To fully describe the dynamics of Greenland fjords one should consider all the scales from the smallest up to the thermohaline circulation. In this chapter I have reviewed the main dynamical processes in Greenland fjords and the role play by the ocean in influencing the submarine melt rate and therefore Greenland contribution to sea-level rise.
In the next chapter I will present a personal work on the impact of fjord dynamics on submarine melt rates using a numerical non-hydrostatic model (MITgcm) where I will focus the attention on small and fjord scale processes.

Chapter 8

Modelling the impact of fjord dynamics on submarine melting of a Greenland glacier

Roberta Sciascia, Fiammetta Straneo, Claudia Cenedese, Patrick Heimbach,
Accepted with minor revision in Journal of Geophysical Research Ocean

Abstract

In a glacial fjord, the circulation driven by a large tidewater glacier is investigated using a non–hydrostatic ocean general circulation model (the MITgcm) with a melt rate parameterization at the vertical glacier front. The model configuration and water properties are based on data collected in Sermilik Fjord near Helheim Glacier, a major Greenland tidewater glacier. The approximately two-layer stratification of the fjord's ambient waters causes the melt water plume at the glacier front to drive a 'double cell' circulation with two distinct outflows, one at the free surface and one at the layer's interface. In summer, the discharge of surface runoff at the base of the glacier (subglacial discharge) causes the circulation to be much more vigorous and associated with a larger melt rate than in winter. The simulated 'double cell' circulation is consistent, in both season, with observations from Sermilik Fjord. Seasonal differences are also present in the vertical structure of the melt rate, which is maximum at the base of the glacier in summer and at the layers' interface in winter. The submarine melt rate is strongly sensitive to the amount of subglacial discharge, to changes in water temperature, and layers interface height. The simulated submarine melt rates are consistent with those inferred from simplified one–dimensional models based on the theory of buoyant plumes. Our results also indicate that to correctly represent the dynamics of the melt water plume, care must be taken in the choice of viscosity and diffusivity values in the model.

8.1 Introduction

Net mass loss from the Greenland Ice Sheet more than doubled over the last decade [Rignot and Kanagaratnam, 2006] and, at present, accounts for one quarter of global sea–level rise [Cazenave and Llovel, 2009, Milne et al., 2009, Bamber et al., 2012]. About half of the mass loss is attributed to an increased ice discharge from the acceleration of outlet glaciers in west and southeast Greenland [van den Broeke et al., 2009] which started in the mid–1990s [Joughin et al., 2004, Stearns and Hamilton, 2007, Howat et al., 2007, 2008]. The acceleration began at the tidewater termini of outlet glaciers where ice-ocean interface processes play a crucial role [Thomas, 2004, Vieli

and Nick, 2011] and an increasing number of studies suggest that it was triggered by the warming of waters around Greenland [Holland et al., 2008, Murray et al., 2010, Motyka et al., 2011, Christoffersen et al., 2011]. The exact chain of events is still unclear, but it has been proposed that warming of ocean waters coming in contact with Greenland's glaciers may have resulted in increased submarine melting at the marine terminus and have impacted glacier stability by thinning and ungrounding the terminus and/or affecting calving (see review by Vieli and Nick [2011]). Therefore submarine melting, and the processes and parameters controlling its magnitude and variability, need to be understood if we are to improve our understanding of past glacier variability in Greenland and its future evolution. This is a challenging problem given the difficulties of observing the ice-ocean interface and modeling the wide range of space and time scales involved. Furthermore, from a modeling perspective, the parameterizations of the ice-ocean boundary layer were derived in the context of vertical isothermal walls [Wells and Worster, 2008], but were mostly applied to Antarctica's floating ice shelves. Given the different properties of Antartica and Greenland ice shelves (e.g. quasi-vertical versus horizontal geometry) and the limited number of studies on Greenland's glaciers, it is unclear whether these parameterizations can be readily applied to Greenland's outlet glaciers and especially to high-resolution numerical models.

In Greenland, tidewater glaciers terminate in long, narrow, deep fjords which connect the glaciers to the surrounding continental shelf waters [Straneo et al., 2012]. Submarine melting at the glacier termini results from a net transport of oceanic heat to the glacier and depends on a range of oceanic and glaciological processes. In the immediate vicinity of the glacier, the circulation is thought to be dominated by the buoyancy driven circulation generated by the glacier itself through the discharge of fresh, buoyant water both at the surface and at depth [Chu et al., 2009, Das et al., 2008]. In the simplest scenario in which the glacier (buoyancy) driven circulation is the only relevant circulation, the leading paradigm is that the transport of heat to the glacier is governed by a steady estuarine-like circulation [Hanna et al., 2009, Rignot et al., 2010, Motyka et al., 2011] as observed for tidewater glaciers in Alaska [Motyka et al., 2003]. In this case, a buoyant plume

develops and is composed of glacially modified and entrained ambient waters. The plume rises vertically near the ice-ocean interface producing a buoyant current of relatively fresh water moving away from the glacier near the ocean free surface. In order to conserve volume, and because of entrainment, an inflow of ambient waters is generated at depth to balance the net surface outflow. In this case, the net heat transport to the glacier (and consequently the submarine melt rate) is due to the difference between the heat transported by warm deep waters flowing towards the glacier and that by cold surface waters flowing away from the glacier. Typically this circulation is thought of as a fast, thin surface outflow and a slow, thick, deep inflow such that the net top-to-bottom volume transport remains balanced. The direct applicability of this paradigm to Greenland's glaciers, however, is complicated by several factors, amongst which are fjord stratification, seasonal variability of subglacial discharge, as well as forcings external to the fjord/glacier system (e.g. continental shelf variability at the mouth of the fjord or local winds). The estuarine paradigm assumes that the fjord waters are mostly unstratified, except for the density contrast between the freshwater discharged by the glacier and the ambient water having a single density. Instead, multiple surveys of Greenland's major fjords have shown that these are typically filled with at least two distinct water masses: a relatively warm, salty water of Atlantic origin at depth (AW) and relatively cold, fresh water of Polar origin in the upper layer (PW) [Azetsu-Scott and Tan, 1997, Holland et al., 2008, Straneo et al., 2010, 2012]. Thus, the buoyant plume near the ice-front rises vertically within a water column whose properties (including density) vary with depth. As suggested both by theoretical and laboratory studies [Huppert and Josberger, 1980, Huppert and Turner, 1980] and by recent observations [Straneo et al., 2011], this may result in a more complex circulation (and hence a more complex pattern of heat transport to the glacier) since the rising buoyant plume may reach its neutral density level before it reaches the free surface.

The presence of different freshwater masses inside the fjord introduces additional elements of complexity in the estimate of submarine melting. The buoyant plume is forced by two distinct glacial waters sources: one due to subglacial discharge, and one due to submarine

melting. Herein, by subglacial discharge we indicate the portion of surface runoff occurring on the glacier surface, in contact with air, that is discharged at the glacier base and, by submarine melting the melting of the glacier front immersed in water. As argued in recent studies, the subglacial discharge that enters the fjord at depth is likely to be a major contributor to the dynamics (e.g. Motyka et al. [2003]) by forcing the buoyant plume at the glacier front and, as such, to be a primary control on the submarine melt rate [Jenkins, 2011, Xu et al., 2012]. Yet how the submarine melt rate depends on the magnitude and seasonal variability of subglacial discharge remains largely unknown.

Some progress on the dynamics near the ice-ocean interface has been made using simplified one-dimensional models based on the theory of buoyant plumes [Hellmer and Olbers, 1989, Jenkins, 1991, 2011]. MacAyeal and Jacobs [1985] applied a plume model to the overturning circulation beneath ice shelves where the submarine melting generated by ice-ocean interaction is a distributed source of buoyancy. Without an initial localized buoyancy source (i.e. subglacial discharge), the development of a turbulent plume can be treated in analogy with the theory of convection against a heated plate [Wells and Worster, 2008]. More recently, Jenkins [2011] developed a simplified model, analogous to MacAyeal and Jacobs [1985], for the dynamics at the grounding line of ice shelves and tidewater glaciers where the main forcing is assumed to be the buoyancy flux generated by the subglacial discharge. In the case of Greenland's tidewater glaciers, this assumption is likely valid for the summer but not necessarily for winter, when the shutdown of surface runoff strongly reduces the buoyancy source at the base of the glacier terminus. Given the inherent simplicity of these models, their ability to capture the complexity of the dynamics may be limited and the effects of the dynamics neglected in these models needs to be addressed. Many of the relevant oceanic processes such as the circulation generated by the glacier subglacial discharge, the fjord's circulation itself, and the effect of viscosity and diffusivity on the circulation are not captured by these one-dimensional plume models. These effects can be included by using more complex models such as general circulation models (GCM). Recently, Xu et al. [2012] have shown that high-resolution ocean models can be useful tools to

investigate the complex ocean dynamics near the ice-ocean interface. Although turbulence, boundary layer dynamics, and entrainment are still parameterized at the resolution used both in Xu et al. [2012] and in the present study, the use of high-resolution ocean models can highlight the limitation and strength of simplified one-dimensional plume models.

Here, we investigate the ice-ocean boundary layer dynamics and the fjord circulation forced by glacial boundary conditions (subglacial discharge and submarine melting) using a high-resolution, non-hydrostatic ocean general circulation model (GCM) with a thermodynamical melt rate parameterization of a vertical glacier terminus. The configuration is an idealized version of a major glacier/fjord system, Helheim Glacier and Sermilik Fjord in southeast Greenland. Field data collected both in summer and winter provide the initial and boundary conditions for this problem and are used for comparison. Specifically, we investigate differences between summer and winter conditions due to changes in subglacial discharge as well as water properties. The goal of this study is to obtain estimates of submarine melting for Helheim Glacier and its dependency on subglacial discharge, temperature, and stratification of ambient waters. The novelty of this study compared to previous studies using one-dimensional plume models (e.g. Jenkins [2011]) is in the use of a GCM which includes more dynamical effects, in particular the circulation generated by glacial forcing and the effect of viscosity and diffusivity on the circulation. Compared with previous studies using a GCM [Xu et al., 2012], this study differs in terms of regime investigated. We focus mainly on the regime in which the melt water plume generates a 'double cell' circulation with two distinct outflows, one at the free surface and one at the layers' interface, similar to that inferred from observations in Sermilik Fjord [Straneo et al., 2011]. In particular, we propose a scaling argument to characterize the dynamical regime of the circulation generated by the glacier. Our results suggest that velocity dependent turbulent transfer coefficients substantially modify not only the magnitude of the submarine melting but also its vertical distribution. Hence, our study provides new insight into the dynamics regulating the submarine melting and points to possible fundamental dynamics still missing in the formulation of the problem.

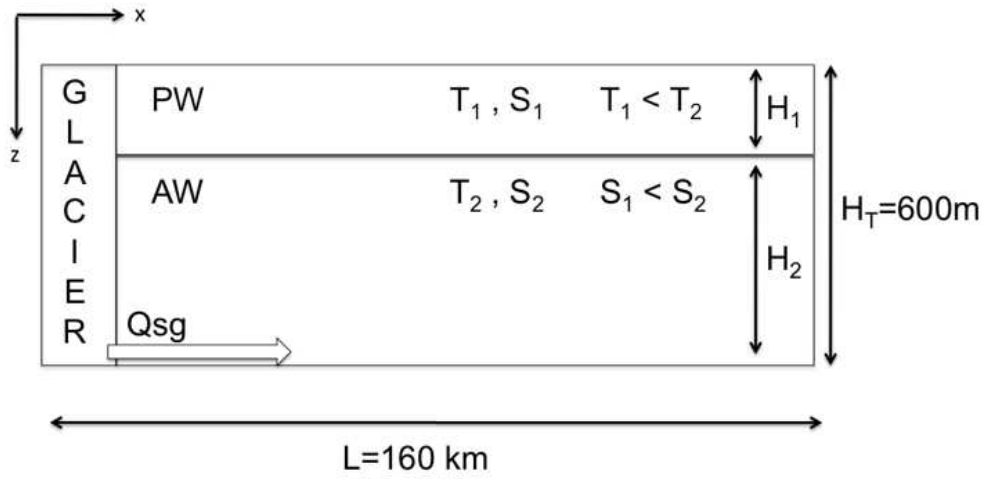

Figure 8.1: Model geometry with the glacier front on the left side of the domain and the mouth of the fjord on the right side of the domain. PW (Polar waters) layer with temperature T_1 and salinity S_1. AW (Atlantic waters) layer with temperature T_2 and salinity S_2. Subglacial discharge is confined to the last two cells near the bottom of the domain. Horizontal and vertical resolution at the glacier front are 10 m.

The model and its set–up are described in section 2. These are followed by a review of the theory of buoyant line plumes, section 3. The main findings are presented in sections 4 to 8 followed by a summary and conclusions in the final section.

8.2 Model Set-up

To investigate the circulation and melting at the terminus of a Greenland tidewater glacier we use the following idealized set-up. We consider a vertical glacier front at the head of a rectangular fjord and assume that it is grounded at the bottom of the fjord (Figure 8.1). The configuration is chosen to broadly match the features of Helheim Glacier, a large tidewater glacier in southeast Greenland, which discharges into Sermilik Fjord ($66°N, 38°W$) [Straneo et al., 2010]. The real fjord's width varies from 4 to 10 km and is about 100 km long, with depths varying from 900 m at the mouth to around 600 m at the head [Schjøth et al., 2012]. Hydrographic surveys [Straneo et al., 2010] have shown that property changes occur primarily in the along-fjord direction and that across-fjord gradients are small. This is consistent with the fact that the Rossby radius of deformation and fjord

width are roughly equal and, therefore, that rotation has a secondary effect on the fjord dynamics. Hence, we simplify the problem to a two-dimensional one, assuming no variations in the across-fjord direction. As a result of this simplification, this set-up is ill-suited to study across-fjord variations induced, for example, by a localized (in the horizontal) subglacial discharge channel. Yet, overall, we think it is an important first step to understand the leading dynamics of the problem.

Helheim glacier terminus is represented as a $H_T = 600$ m deep wall (the thermodynamical parameterization is described below) with a vertical front (i.e. no floating ice tongue) typical of the present state of Greenland's outlet glaciers [Joughin et al., 2004]. Subglacial discharge is confined near the bottom of the glacier where the input of fresh water is likely to have the largest impact on the dynamics. Also, it is consistent with the notion that the bulk of the seasonal surface runoff is discharged at the base of the glacier through a series of drainage channels [Andreasen, 1985, Zwally et al., 2002, Das et al., 2008, Catania et al., 2008].

8.2.1 The Model

The MITgcm (http://mitgcm.org) is a substantially evolved version of Marshall et al. [1997a,b] and Adcroft et al. [2004] which solves the Boussinesq form of the Navier–Stokes equations on a generalized curvilinear grid. The finite-volume discretization is rendered on a horizontal Arakawa C-grid, and with vertical z-levels. The model has been used over a wide range of geophysical phenomena, from large-scale ocean circulation to small scale processes, both in realistic [Magaldi et al., 2011] and idealized [Spall, 2011] set–ups.

In our study we consider a high–resolution, non–hydrostatic set–up [Marshall et al., 1998] with a modified version of the UNESCO equation of state by Jackett and Mcdougall [1995]. In this configuration mixing processes are permitted up to the grid scale of the model. Previous studies have applied similar high-resolution formulations to problems such as internal waves, overflows, and convection [Legg and Adcroft, 2003, Legg et al., 2006, Visbeck et al., 1996]. We perform two-dimensional idealized experiments (Figure 8.1) with 10 m uniform vertical resolution and a telescopic horizontal resolution

going from 10 m at the glacier front up to 500 m at the mouth of the fjord. The model width in the $y-$direction is one grid cell of size $L = 10$ m. 3D simulations with a 6 km wide fjord (not shown) reveal that the across fjord variability and the differences between the 3D and 2D simulations are small provided that the forcing applied (e.g. subglacial discharge) is 2D. The advantage of using a 2D setup is that the reduced computational cost allow us to perform a large number of simulations.

Sub-grid scale processes are parameterized using a Laplacian eddy diffusion of temperature, salinity, and momentum with grid–size re–scaled constant coefficients. At the scales adopted (10 m x 10 m), diffusive (κ) and viscous (ν) processes are dominated by turbulence and consequently are of the same order of magnitude. Hence, the choice of dimensional parameters (Table 8.2) is such that the horizontal Prandtl number is equal to one and the properties vary without discontinuities at the grid-scale of the model. Depending on the characteristics of the simulations the model is integrated with a time step ranging from 1 to 20 seconds (Table 8.1).

The boundary conditions of the model are free surface at the top, rigid boundaries with no-slip boundary conditions at the bottom and left side (i.e. glacier front), and open boundary on the right side (i.e. fjord's mouth) with a sponge layer restoring temperature and salinity profiles to those prescribed as initial conditions. The domain is sufficiently long (160 km) for the simulations to reach a steady state before the open boundary conditions influence the circulation at the glacier front. In section **??** we describe a series of sensitivity experiments supporting our assumption that the leading order dynamics in the fjord do not depend on the exact choice of parameters such as horizontal resolution, ν, or κ.

8.2.2 Melt rate parametrization

The thermodynamical melt rate parameterization of the ice–ocean boundary (eqs. 8.2.1-8.2.3) is based on the Holland and Jenkins [1999]

Table 8.1: Value of dimensional parameters used in each simulation (see section 8.2.5 for details).

	Qsg [m^3s^{-1}]	Δx [m]	Δy [m]	Δt [s]	$\gamma_{T,S}$	H_2 [m]	T_1 [$^\circ C$]	T_2 [$^\circ C$]	S_1 [psu]	S_2 [psu]	$\overline{smr}$ [myr^{-1}]
WIN	0	10	10	10	variable	450	-1.5	4	32.9	34.6	70
SUM	4.3	10	10	5	variable	450	-1.5	4	32.9	34.6	738
WIN50	0	50	10	20	variable	450	-1.5	4	32.9	34.6	34
WIN20	0	20	10	10	variable	450	-1.5	4	32.9	34.6	42
WIN5	0	5	10	1	variable	450	-1.5	4	32.9	34.6	57
WINγ	0	10	10	10	constant	450	-1.5	4	32.9	34.6	59
SUMs	4.3	10	10	5	variable	450	0.5	3	32.5	34.5	551
SUMd	0.29 - 8.7	10	10	5	variable	450	-1.5	4	32.9	34.6	73 - 1111
TEMP	0	10	10	10	variable	450	-1.5	0-8	32.9	34.6	0.7 - 172
TEMPs	4.3	10	10	10	variable	450	-1.5	0-8	32.9	34.6	170 - 1104
INTER	0	10	10	10	variable	50-550	-1.5	4	32.9	34.6	0.4 -104
INTERs	4.3	10	10	10	variable	50-550	-1.5	4	32.9	34.6	225 - 677
SALT	0	10	10	10	variable	450	-1.5	4	32.9	34-35	69-66
SALTs	4.3	10	10	10	variable	450	-1.5	4	32.9	34-35	776-686

Table 8.2: Dimensional parameters and variables (T_b, S_b, q) used in the simulations.

Symbol	Description	Value	Unit
ρ	density of water	1030	$kg\,m^{-3}$
c_p	specific heat capacity	3974	$Jkg^{-1}\,K^{-1}$
$C_d^{1/2}\Gamma_T$	thermal Stanton number	$1.1 \cdot 10^{-3}$	
$C_d^{1/2}\Gamma_S$	diffusion Stanton number	$3.1 \cdot 10^{-5}$	
L_i	latent heat of fusion of ice	334000	$J\,kg^{-1}$
ρ_i	density of ice	916	$kg\,m^{-3}$
$c_{p,i}$	heat capacity of ice	3974	$Jkg^{-1}\,K^{-1}$
k	heat diffusivity	$1.54 \cdot 10^{-6}$	$m^2\,s^{-1}$
λ_1	liquidus slope	-0.0573	$^\circ C$
λ_2	liquidus intercept	0.0832	$^\circ C$
λ_3	liquidus slope	$-7.53 \cdot 10^{-8}$	$^\circ C\,Pa^{-1}$
T_w	water temperature	see Table 8.1	$^\circ C$
T_i	ice temperature	-10	$^\circ C$
S_w	water salinity	see Table 8.1	psu
ν_H	horizontal viscosity	$2.5 \cdot 10^{-1}$	$m^2\,s^{-1}$
ν_V	vertical viscosity	10^{-3}	$m^2 s^{-1}$
κ_H	horizontal diffusion	$2.5 \cdot 10^{-1}$	$m^2\,s^{-1}$
κ_V	vertical diffusion	$2 \cdot 10^{-5}$	$m^2\,s^{-1}$
T_b	boundary temperature		$^\circ C$
S_b	boundary salinity		psu
q	melt rate of ice		$kg\,m^{-2}\,s^{-1}$

and Jenkins et al. [2001] three-equations model

$$T_b = \lambda_1 S_b + \lambda_2 + \lambda_3 P_b, \tag{8.2.1}$$

$$c_p \rho_i \gamma_T (T_w - T_b) = -L_i q - \rho_i c_{p,i} k (T_i - T_b), \tag{8.2.2}$$

$$\rho_i \gamma_S (S_w - S_b) = -S_b q. \tag{8.2.3}$$

Equation (8.2.1) is the linear equation for the freezing temperature of seawater, where T_b, P_b and S_b are the temperature, pressure and salinity at the ice–ocean boundary, respectively, and λ_{1-3} are constants. Together with the conservation of heat, eq.(8.2.2) and salinity, eq.(8.2.3), these equations describe the thermodynamical equilibrium at the ice-ocean interface. T_w and S_w are the sea water temperature and salinity, T_i is the ice temperature, $\gamma_{T,S}$ are the turbulent transfer coefficients for temperature and salinity, and the other parameters in equations (8.2.1)-(8.2.3) are defined in Table 8.2. This ice–ocean boundary parameterization has been used to model sub-ice shelf melting around Antarctica with the MITgcm [Losch, 2008].

While most of the terms in the thermodynamical parameterization

of the ice-boundary (eqs. 8.2.1-8.2.3) are physical constants that can be easily measured, the same cannot be said for the turbulent transfer coefficients $\gamma_{T,S}$ which represent a parameterization of the effects of turbulence in the ice-ocean boundary layer. Earlier parameterizations of the turbulent transfer coefficients by Hellmer and Olbers [1989] adopted a constant value for $\gamma_{T,S}$. Holland and Jenkins [1999] and more recently Jenkins et al. [2010] showed that a parameterization with a functional dependence on water velocities produces a better agreement with submarine melt rate measurements. Hence, in our formulation we use a parameterization that include a functional dependence on the water velocity. Explicitly, the transfer coefficients $\gamma_{T,S}$ are defined as

$$\gamma_{T,S} = C_d^{1/2} \Gamma_{T,S} U_b, \tag{8.2.4}$$

where $U_b = \sqrt{u_b^2 + w_b^2}$ is the magnitude of the velocity at the ice-ocean boundary. $C_d^{1/2}\Gamma_{T,S}$ are the thermal and diffusive Stanton number [Steele et al., 1989] and their values are those used of [Jenkins et al., 2010, Jenkins, 2011]. Parameters values and variables used in the equations are given in Table 8.2.

The turbulent transfer coefficients are related to the far field current beyond the ice-ocean boundary layer [Jenkins et al., 2010] but, at present, it is unclear what this velocity actually is. For quasi-horizontal ice shelves, like those present in Antarctica, the relevant velocities are the horizontal ones parallel to the ice shelf. In the case of significant tidal flows, such as under Ross ice shelf, these velocities are assumed to be dominated by the magnitude of the tidal flows [Jenkins et al., 2010]. In the case of a vertical glacier front, the relevant velocity is likely that of the buoyant plume with additional potential contributions from tidal flows, internal fjord modes, and externally driven flows [Jenkins et al., 2010, Jenkins, 2011]. If we consider the glacier–driven circulation alone, plume theory suggests that at the ice-ocean boundary the vertical velocity is much larger than the horizontal velocity induced by entrainment. Hence, at the vertical glacier front the velocity dependence of the turbulent transfer coefficients is likely determined mainly by the vertical velocity of the buoyant plume.

8.2.3 Boundary conditions - Subglacial discharge

As we show below, among the parameters and forcing explored here the largest seasonal control on the fjord's circulation and the submarine melt rate is the subglacial discharge. In summer, large amounts of surface runoff are thought to find their way to the bed of Greenland's glacier and discharge fresh water at depth [Das et al., 2008]. Evidence for these fresh intrusions in summer and their absence in winter in Sermilik Fjord is discussed in Straneo et al. [2011]. To investigate this seasonal variability we consider two distinct seasonal regimes: a winter regime with no subglacial discharge, and a summer regime with subglacial discharge. Geothermal and frictional melting at the base of the glacier are much smaller than submarine melting and subglacial discharge [Mernild et al., 2010]. Thus, we assume that the melting generated by these two processes can be neglected in both seasons. To quantify a plausible range for the summer subglacial discharge in our simulations we proceed as follows. Andersen et al. [2010] estimate a summer surface runoff of $Q_{TOT} \sim 174$ m^3 s^{-1} entering the fjord from Helheim Glacier catchment basin through an unknown number of drainage channels of unknown dimensions. Since our simulations are limited to a 10 m wide vertical slice of the fjord and glacier, it makes little sense to force the model with the total discharge (this would be equivalent to assume that the entire discharge occurs through a 10 m wide channel). Instead, we consider two scenarios that may provide plausible lower and upper limits for the subglacial discharge forcing to be used in our simulations. For the lower bound, we consider the case in which the total subglacial discharge is uniformly distributed along the entire base of Helheim Glacier. Assuming that Helheim Glacier is 6 km wide, this amounts to a discharge flux of 0.029 m^2 s^{-1} per unit width. Since our 2D slice is 10 m wide (i.e. it has the width of a grid cell), the uniformly distributed flux that provides the lower limit for our simulations amounts to a subglacial discharge $Qsg = 0.29$ m^3 s^{-1}. For the upper limit, we assume that Helheim's entire subglacial discharge occurs through a single opening that is 200 m wide. Since our 2D slice is 10 m wide this upper limit amounts to $Qsg = 8.7$ m^3 s^{-1}. In examining the impact of subglacial discharge on the dynamics at the ice front, we perform a series of experiments with discharge values ranging between these two extremes: the 'distributed' scenario

and the 'single' channel scenario. It is important to stress that the problem addressed here is two–dimensional in nature, and that we are not investigating the 3D dynamics associated with the discharge by a localized channel but rather the 2D dynamics associated with the flux expected from a channel.

We impose a subglacial discharge with zero salinity, at the freezing temperature for the given depth, and with an initial horizontal velocity computed from the total discharge $u_{Qsg} = Qsg/A$, where A is the area of the model cells where the subglacial discharge is applied (20 m high and 10 m wide). Some plume models [Mugford and Dowdeswell, 2011] derive the initial subglacial discharge velocity from the Manning equation for a open channel flow [Chow, 1959] which gives rise to larger initial velocities. We also performed experiments using these larger velocities and found that it did not significantly impact the results. We conclude that the dynamics is more sensitive to the subglacial discharge magnitude rather than to the prescribed initial velocity. The subglacial discharge is treated as a 'virtual mass flux' which modifies water properties of a given water mass (i.e. temperature, salinity, velocity) without adding volume to the system. This choice is volume–conserving and allows us to minimize the number of parameters necessary to define the problem by imposing open boundary conditions only on temperature and salinity fields. On the other hand, this formulation does not conserve salt, but for the time and space scales considered in this study, this effect is negligible.

8.2.4 Initial conditions

Sermilik Fjord is filled with two water masses [Straneo et al., 2010]: a cold and fresh layer of polar waters (PW) overlying warm, salty Atlantic waters (AW) (Figure 8.1). The winter profiles (Figure 8.2a) clearly show a two–layer stratification of temperature and salinity, and hence density. In summer (Figure 8.2b), the stratification is more complex, reflecting the presence of large volumes of glacially modified waters in the upper 100-200 m [Straneo et al., 2011]. The winter runs were initialized with a two–layer stratification in which the temperature and salinity in each layer are equal to the layer average as observed during a winter survey of Sermilik Fjord (Table 8.1). In summer, magnitude and spatial distributions of temperature and salinity

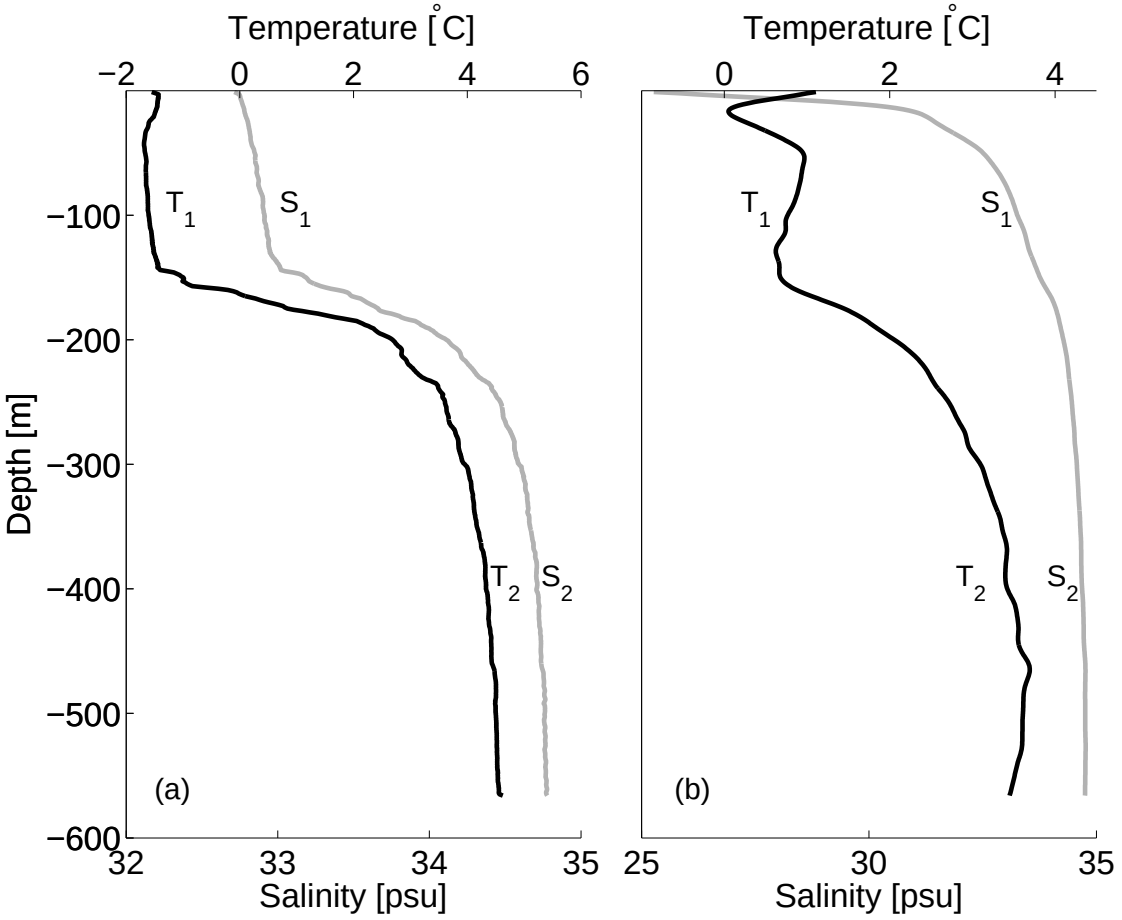

Figure 8.2: Sermilik Fjord temperature and salinity vertical profiles at mid-fjord. Measurement taken in winter 2010 (a), and summer 2009 (b) [Straneo et al., 2011].

differ from winter conditions (Figure 8.2b). For simplicity, and to reduce the number of variables changed simultaneously, we initialize the model with the same idealized two–layer stratification. In summer, we consider two different scenarios: one in which the temperature and salinity are identical to the winter runs (SUM, Table 8.1), and one in which the temperature and salinity are those observed in summer (SUMs, Table 8.1, and Figure 8.2b). The same water temperature and salinity profiles used for the initial conditions in the fjord are used as relaxation profiles at the open boundary. The interface between the two water masses is set to a depth of 150 m with the exception of the runs described in section 8.6 (INTER, INTERs Table 8.1). The flow is assumed to be initially at rest and analysis is carried out after a spin–up period of 8 days.

8.2.5 Model experiments

We conduct a series of experiments aimed at investigating the dynamics of the glacier driven buoyant plume in both winter and summer conditions, and its sensitivity to model parameters. In particular, we focus on the submarine melt rate's dependence on the subglacial discharge rate and the fjord's bottom layer temperature, salinity and thickness. The experiments are briefly described below and listed in Table 8.1.

Control experiment - WIN

Control experiment with winter water properties (Figure 8.2a) and without subglacial discharge.

Summer experiment - SUM

We explore the effect of summer subglacial discharge on fjord dynamics by considering a simulation with the same water properties of the WIN experiment but with a steady subglacial discharge equal to $Qsg = 4.3$ m^3 s^{-1} equivalent to a total discharge fluxed through a 400 m wide opening.

Summer experiment - SUMs

Same as the SUM simulation except the initial water properties are those observed during the summer survey (Figure 8.2b). The idealized two–layer stratification is maintained.

Sensitivity to subglacial discharge - SUMd

Sublgacial discharge rate is highly variable during summer. In this

set of experiments we explore the influence of the subglacial discharge rate on submarine melting and fjord circulation by varying the subglacial discharge within the range $Qsg = 0.29 - 8.7$ m^3 s^{-1}. For each experiment we consider a steady subglacial discharge.

Sensitivity to grid resolution - WIN5, WIN20, WIN50

With this set of experiments we explore the sensitivity of submarine melt rate to numerical horizontal resolution (5 m, 20 m, and 50 m, respectively).

Sensitivity to velocity - $WIN\gamma$

In all the experiments the turbulent transfer coefficients (eq. 8.2.4) are functions of the velocity U_b at the ice-ocean interface. Here we consider how the results differ if U_b is assumed to be constant. All other parameters are identical to the WIN run.

Sensitivity to AW temperature - TEMP and TEMPs

In these experiments we vary the temperature of the AW layer from $0°C$ to $8°C$ with $1°C$ increments, both in the WIN (TEMP) and SUM (TEMPs) set–up.

Sensitivity to AW thickness - INTER and INTERs

In these experiments we vary the AW thickness, H_2, from 50 m to 550 m with 50 m increments, both in the WIN (INTER) and SUM (INTERs) set–up.

Sensitivity to AW salinity - SALT and SALTs

In these experiments we vary the AW salinity, S_2, from 34 psu to 35 psu with 0.25 psu increments, both in the WIN (SALT) and SUM (SALTs) set–up.

We compare simulations in terms of water properties and velocity, but also in terms of submarine melt rate at a given depth, $smr(z)$ [m yr^{-1}], its maximum value smr_M [m yr^{-1}], and the vertically averaged submarine melt rate defined as $\overline{smr} = \frac{1}{H_T}\int_{-H_T}^{0} smr(z)\mathrm{d}z$ [m yr^{-1}]. Note that this definition averages the submarine melting over the entire water column depth. Hence, if the melting occurs preferentially in one layer (AW layer, see below) this definition of $\overline{smr}$ will underestimate the average melting for that layer.

8.3 Line plume theory

Near the glacier front, the circulation addressed in this study is that of a buoyant plume rising along the vertical ice front. Its dynamics are controlled by the buoyancy forcing due to the glacier (both submarine melting along the ice front and subglacial discharge at depth), by the entrainment and mixing with the ambient fluid, and by viscous drag at the ice-ocean interface. Since the submarine melt rate depends both on the plume's velocity and its properties (see next sections), a correct representation of the buoyant plume is critical to estimating the submarine melt rate. In the simulations presented throughout the paper, even at grid spacings of 5-10 m, the turbulent buoyant plume is not fully resolved. Nevertheless, the extent to which the model captures the bulk properties of the plume can be evaluated by comparing our model runs to the theory of buoyant plumes [Morton et al., 1956, Turner, 1980]. This theory, although idealized, is a good starting point to describe the processes at play at the ice-ocean interface. If we assume that the buoyancy source due to subglacial discharge is homogeneously distributed along the glacier width, the generated plume can be studied in analogy with the theory of line buoyant plumes in a homogeneous, non–rotating ambient fluid [Turner, 1980]. The flow variables can be expressed in terms of the buoyancy flux per unit length, $B = g'Qsg/L$, and the distance above the source z. In a line buoyant plume the buoyancy flux is constant with depth, the volume flux $Q \sim B^{1/3}z$ increases with height above the source due to entrainment of ambient fluid, the reduced gravity $g' \sim B^{2/3}z^{-1}$ decreases with height, the vertical velocity is constant, $w \sim B^{1/3}$, and the half width of the plume $b \sim z$ increases with height above the source.

Entrainment generated by the turbulent buoyant plume induces the density within the plume to increase due to mixing with denser ambient waters. Following the definition of entrainment velocity $w_e = \alpha w$ [Ellison and Turner, 1959] we define an entrainment flux

$$F_e = \int\int w_e \Delta\rho \mathrm{d}x \, \mathrm{d}z = \alpha \int w \Delta\rho \mathrm{d}x \, \mathrm{d}z, \tag{8.3.5}$$

where α is the entrainment coefficient, w is the plume vertical velocity, and $\Delta\rho$ is the difference between ambient and plume density.

In the simulations, the turbulent entrainment processes are not

resolved but are instead parameterized by a diffusive flux

$$F_d = \kappa \int \int \frac{\partial \rho}{\partial x} \mathrm{d}x \, \mathrm{d}z, \tag{8.3.6}$$

where κ is the horizontal diffusion coefficient, and ρ is the density at a given position x. Therefore, a consistent representation of the buoyant plume requires the entrainment and diffusion fluxes to be of the same order of magnitude ($F_e/F_d \sim 1$). From equations (8.3.5) and (8.3.6) this occurs when

$$\frac{\int \int w \Delta \rho \mathrm{d}x \, \mathrm{d}z}{\int \int \mathrm{d}\rho \, \mathrm{d}z} \simeq \frac{\kappa}{\alpha}, \tag{8.3.7}$$

where $\alpha = 0.08$ is the entrainment coefficient for line plumes [Turner, 1980]. In most of the simulations discussed here, we use $\kappa = 2.5 \times 10^{-1}$ $\mathrm{m^2\,s^{-1}}$ as the model horizontal diffusivity, which yields to values of the LHS of equation (8.3.7) in the range 2 -7, in good agreement with the expected value of $\frac{\kappa}{\alpha} = 3.1$. Hence, we expect the model to capture the leading order dynamics of the evolving plume.

To further investigate the sensitivity of the results to the exact values of the diffusivity, we perform a series of experiments in which we vary the horizontal diffusivity κ. The simulated buoyant plume density ρ_p at $z = -450$ m is compared with the theoretical value for line plumes, ρ_t, at the same distance above the bottom (not shown). We find that a value of κ an order of magnitude smaller produces a lighter buoyant plume than predicted by the line plume theory (i.e. $\rho_t > \rho_p$) indicative of an underestimate of the entrainment flux. A slightly larger value of $\kappa = 9 \times 10^{-1}$ $\mathrm{m^2\,s^{-1}}$ produces slightly larger plume density than in the runs with $\kappa = 2.5 \times 10^{-1}$ $\mathrm{m^2\,s^{-1}}$. This is consistent with having a larger entrainment, further diluting the buoyant plume and increasing its density. Both of these results are consistent with the scaling described above. The above analysis highlights that to correctly represent the dynamics of the buoyant plume generated by submarine melting and subglacial discharge, entrainment processes should be resolved or at least parameterized correctly choosing the appropriate value of κ based on equation (8.3.7). Given that Pr=1 in all the experiments, the above analysis is also valid for the viscosity coefficient ν.

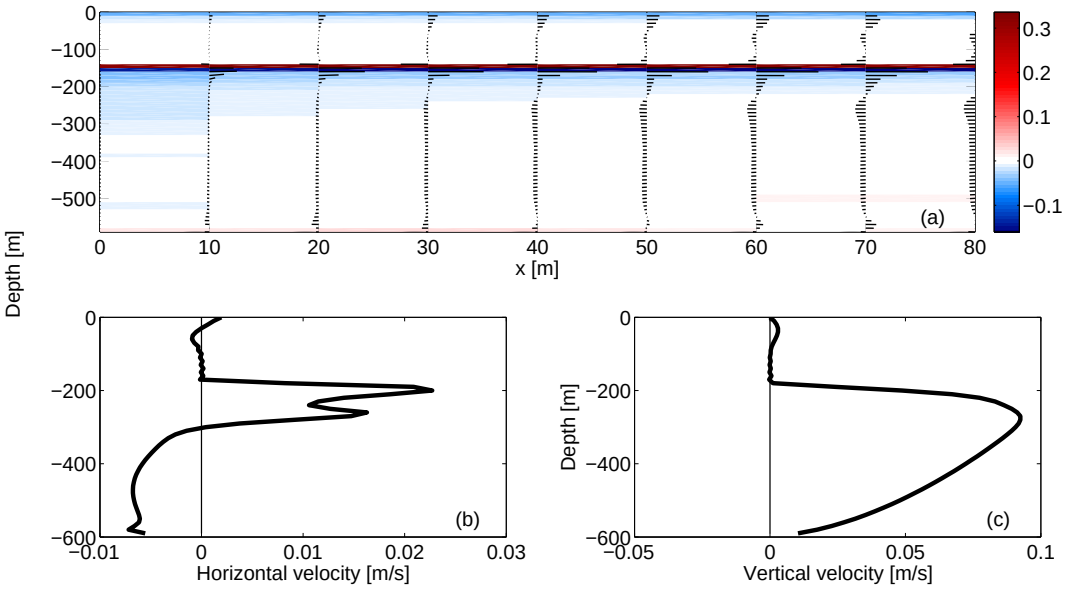

Figure 8.3: Control winter experiment (WIN). (a) Fjord velocities (u, w) overlaid on the salinity anomaly with respect to the initial conditions (the glacier front is on the left side of the panel). (b) Horizontal velocity profiles averaged over $0 \leq x \leq 100$ m. (c) Vertical velocity profile at the glacier front. Thin black lines correspond to zero velocity. All quantities have been averaged over a 300 hrs period.

8.4 Control winter experiment (WIN)

In the control run (WIN) submarine melting at the glacier front by ocean waters gives rise to a buoyant, relatively fresh plume (a mixture of glacial waters and entrained ambient waters) which rises along the vertical front of the glacier. The velocities close to the glacier front are mainly vertical while the horizontal velocities become dominant with increasing distance from the glacier (Figure 8.3). Two distinct plumes are evident in this run, one generated by melting in the upper 150 m, within the PW layer, which reaches the free surface, and a second plume, with density ρ_p, such that $\rho_1 < \rho_p < \rho_2$ where ρ_1 (ρ_2) is the density of the upper PW (lower AW) layer, which intrudes at the interface between the two water masses. As a result, there are two distinct outflows of glacial melt water mixtures, one at the free surface and one at the layers' interface. Conservation of volume and entrainment processes, in turn, drive ambient waters to the glacier front in the bottom layer ($\sim 300 - 600$ m) and in the upper layer ~ 80 m (Figure 8.3b) generating a 'double cell' circulation consistent with that inferred from water properties collected in a winter survey of

Sermilik Fjord [Straneo et al., 2011]. In our simulations, the transport in the lower cell is much greater than in the upper cell, consistent with the larger melting driven by AW compared to PW.

Similarly, the plume's vertical velocity is maximum in the AW layer with a mean value in this layer of $\sim 0.04\ \mathrm{m\,s^{-1}}$ (Figure 8.3c). Within this layer, the vertical velocity increases with distance above the bottom due to the increased buoyancy flux resulting from the addition of melt water as the plume rises. Consequently, the vertical velocity of the plume reaches its maximum at the AW/PW interface (Figure 8.3c). Because the submarine melt rate depends on the plume velocity, the *smr* also increases towards the surface in the AW layer, reaching its maximum value at the AW/PW interface. The outflow averaged horizontal velocity in the lower layer is $\sim 0.02\ \mathrm{m\,s^{-1}}$ (Figure 8.3b), even though the front, i.e. 'nose', of the buoyant current has a maximum velocity of $0.09\ \mathrm{m\,s^{-1}}$. In our simulations, the nose of the current reaches the end of the domain (160 km) in $\sim$ 21 days. After this time, the model shows changes in the $\overline{smr}$ which we attribute to the impact of the open boundary on the circulation. In terms of spin-up, we see that after about $\sim$ 8 days the submarine melt rate reaches a steady state. Thus, to estimate the submarine melt rate in steady conditions, we compute the $\overline{smr}$ by averaging from day 9 to 21 of the simulation, i.e. after the transient initial period and before the open boundary affects the $\overline{smr}$. The $\overline{smr}$ for WIN is $70\ \mathrm{m\,yr^{-1}}$.

8.5 Sensitivity analysis

8.5.1 Model Resolution

The sensitivity of the fjord circulation and submarine melt rate to the model resolution is estimated by varying the horizontal resolution ($\Delta x = 50$ m, 20 m, and 5 m) and then comparing the results with the control experiment. The vertical resolution is kept constant at $\Delta z = 10$ m. Following Bryan et al. [1975], the horizontal grid scale Reynolds number, $Re_H = u\Delta x/\nu_H$ where u is the horizontal velocity, is kept constant and below 2 by changing the horizontal viscosity accordingly. Similarly, the horizontal diffusion is varied to keep the Prandtl number $Pr = \nu_H/k_H = 1$ for all the simulations. Sensitivity to horizontal grid resolution is closely related to the choice of viscosity and diffusivity

parameters which have been kept constant for the winter and summer experiments. For this reason, all the results described below (WIN5-WIN50) can be extended to the summer season.

We find that as the resolution decreases from 10 m to 50 m, the $\overline{smr}$ decreases by a factor of 2 (Table 8.1). We attribute this behavior to the fact that the submarine melt rate depends strongly on the buoyant plume's vertical velocity and that, by lowering the resolution, the upwelling plume is forced to occur over a greater horizontal distance (greater than or equal to the cell width), thus resulting in lower vertical velocities. A decrease in the $\overline{smr}$ is also found as the horizontal resolution is increased from 10 m to 5 m (Table 8.1). The parameterization of boundary layer processes depends on the model's resolution. In this work, we parameterize entrainment processes with diffusive and viscous coefficients (see section 8.3) and, when using a 5 m horizontal resolution we are, at the same time, partially resolving the relevant turbulence and also parameterizing it. This produces an artificially larger entrainment than is dynamically consistent and, therefore, a slower plume and decreased submarine melt rate.

8.5.2 Velocity dependence of the turbulent transfer coefficients

When the only buoyancy source is the submarine melting (WIN), we find that the vertical plume velocity is maximum at the layers' interface and minimum at the bottom, with a mean value in the AW layer of 0.04 $\mathrm{m\,s^{-1}}$ (Figure 8.3c) which yields $\gamma_T = 0.44 \times 10^{-4}$ $\mathrm{m\,s^{-1}}$ and $\gamma_S = 1.2 \times 10^{-6}$ $\mathrm{m\,s^{-1}}$. To examine the importance of the vertical structure of the plume's velocity and that of the turbulent transfer coefficients, we perform one experiment (WINγ) where the velocity U_b in the turbulent transfer coefficients is fixed and equal to the mean vertical velocity in the AW layer of the WIN run, and compare the results to those obtained in the WIN run.

Even though the two simulations have a comparable $\overline{smr}$ (Table 8.1), the variation of the submarine melt rate in the vertical is quite different (Figure 8.4). In the WINγ experiment, the melt rate depends only on the fjord water's properties and has a constant profile in the lower layer, with a slight increase with depth due to pressure effects on the freezing temperature of seawater. This is in contrast with the

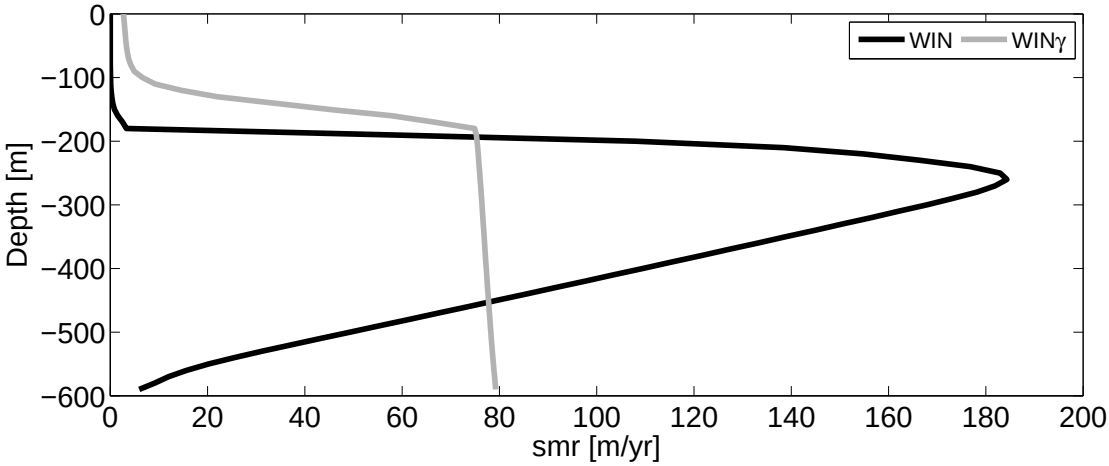

Figure 8.4: Vertical profiles of submarine melt rate for different parameterizations of the turbulent transfer coefficients.

results of the WIN run where the submarine melting is a function of both temperature and flow velocity at the glacier front. As the buoyant plume rises, the vertical velocity increases (Figure 8.3c) producing larger values of submarine melt rate close to the interface between the two water masses (Figure 8.4). By imposing a constant $\gamma_{T,S}$ one is effectively assuming that the velocity along the ice-ocean interface does not vary. The differences between the two simulations are even more evident within the PW layer where in the WIN run the melting is essentially zero because the plume's velocity is quite small, while in the $WIN\gamma$ run the mean velocity used gives rise to a significant melt rate even in this layer. These results suggest that not only the amplitude, but also the vertical velocity structure near the glacier front has a leading order impact on submarine melt rate estimates and its vertical structure. Knowledge of these details are therefore necessary to evaluate if and how ocean forcing can affect glacier stability.

8.6 Summer experiment

The large summer surface runoff which occurs over southern Greenland gives rise to a large subglacial discharge which is likely to be a major contributor to the buoyant upwelling plume at the glacier's front. In our summer simulation (SUM), we find that the buoyancy forcing is dominated by the subglacial discharge and that its occurrence changes the amount of submarine melting dramatically.

For the particular choice of subglacial discharge used in SUM, the overall features of the circulation are largely similar to those of WIN, with a double-cell circulation that is enhanced in the AW layer and at the PW/AW interface (Figure 8.5a), consistent with observations from Sermilik Fjord [Straneo et al., 2011]. Yet the magnitude of the vertical velocity is much larger in SUM and it exhibits a very different variation with depth (Figure 8.5c). This, in turn, gives rise to a much larger melt rate $\overline{smr} = 738\ \mathrm{m\,yr^{-1}}$ (an order of magnitude larger) and a much larger salinity anomaly than in WIN (Figures 8.5a - 8.3a, note the different scale of the colorbar).

The maximum value of submarine melt rate in SUM is found near the bottom, and not at the layers' interface as in WIN (Figure 8.5b), due to the different vertical velocities profiles in the two experiments (Figure 8.5c). In winter, the dominant buoyancy forcing of the plume is due to the addition of water melted along the glacier front. Thus, the buoyancy forcing increases as the plume rises and more melt water is added. This gives rise to a vertical velocity which increases with depth and is maximum at the PW/AW interface. In summer, the large buoyancy flux due to the subglacial discharge causes the vertical velocities to have a maximum near the bottom where the water is discharged into the fjord (Figure 8.5c). As the buoyant plume rises, the vertical velocity decreases slightly with depth (probably due to viscous effects) which, together with the contribution from pressure effects, causes the submarine melt rate to decrease with increasing distance from the bottom.

The results obtained with (SUM) and without (WIN) subglacial discharge are compared with those obtained using the Jenkins [2011] 1D plume model with similar initial conditions and subglacial discharge. Jenkins [2011] describes the evolution of a buoyant plume by solving four ordinary differential equations for the conservation of mass, momentum, heat, and salt. The 1D model takes into account entrainment processes by introducing a parameterization for the entrainment rate which is a linear function of the plume velocity [Ellison and Turner, 1959] $w_e = \alpha w$, where w_e is the entrainment (horizontal) velocity, α is the entrainment coefficient, and w is the plume vertical velocity (see section 8.3). Figure 8.5b shows that in both runs the vertical profiles of submarine melt rate agree with those obtained with

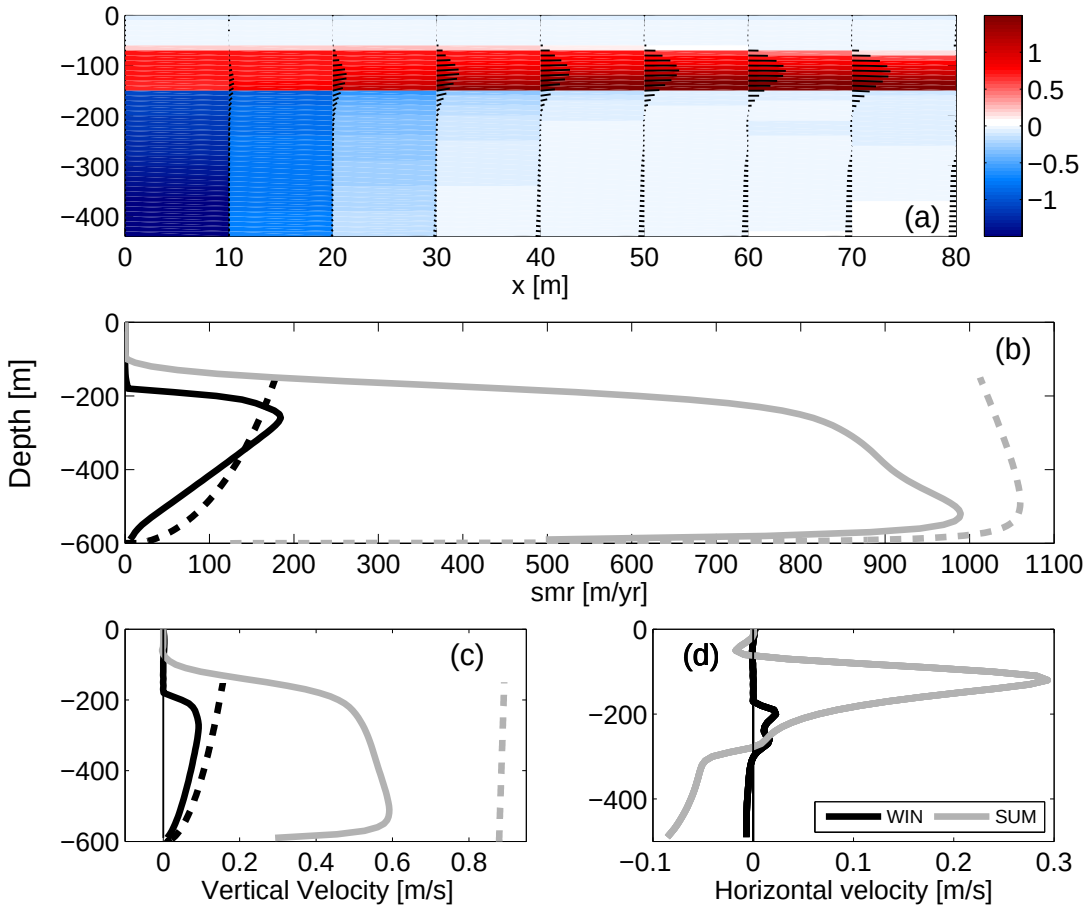

Figure 8.5: Summer (SUM) and winter (WIN) runs comparison. (a) SUM fjord circulation (u, w) overlaid on the salinity anomaly with respect to the initial conditions (the glacier front is on the left side of the panel). (b) Vertical profiles of submarine melt rate. (c) Vertical velocity profiles at the glacier front. (d) Horizontal velocity profiles averaged over $0 \leq x \leq 100$ m. All quantities have been averaged over a 300 hrs period. Dashed lines are profiles computed using the Jenkins [2011] plume model with the same initial subglacial discharge values in summer and $Qsg << 1$ in winter. Black (gray) lines represent winter (summer) runs. Thin black lines correspond to zero velocity.

Jenkins' 1D plume model (dashed lines). In winter, both profiles have a maximum at the layers' interface while in summer the maximum is at the glacier's grounding line. The vertical velocities in Jenkins' model are larger (Figure 8.5c), especially for the SUM run, resulting in an increased submarine melt rate compared to our simulations. The model of Jenkins [2011] is a simplified 1D model in which the viscous forces are neglected, possibly explaining the larger vertical velocities compared to our 2D model results in which viscous forces are included. It is important to note that Jenkins' plume reaches, in both runs, its neutral buoyancy level at the interface between the two water masses and therefore the comparison is possible only in the AW layer, which is the dynamically dominant layer as shown in Figure 8.5a.

As discussed earlier, summer conditions in Sermilik Fjord differ from winter ones in two ways. One important difference is the summer subglacial discharge investigated above. A second difference is that the water properties observed in summer were somewhat different from those observed in winter (Figure 8.2). Here, we examine whether adding more realistic summer water properties further affects the winter/summer differences due to the subglacial discharge described above. Therefore, in SUMs we maintain the idealized two–layer stratification but use summer values of temperature and salinity (Table 8.1) while keeping all the other parameters unchanged. Our results show that the summer/winter water property differences do impact the submarine melt rate, but that overall their effect is secondary compared to the presence/absence of subglacial discharge. The model shows the same leading order dynamics in both SUM and SUMs. The lower submarine melt rate in SUMs, $\overline{smr} = 551\ \mathrm{m\,yr^{-1}}$, compared to $\overline{smr} = 738\ \mathrm{m\,yr^{-1}}$ found in SUM (Figure 8.6), is attributed to the fact that the AW temperature observed in summer was lower than that observed in winter (Table 8.1).

8.7 Influence of subglacial discharge variability

Estimates of subglacial discharge suggest large variability from hourly to seasonal to interannual timescales [Andersen et al., 2010, Mernild et al., 2010]. To investigate the sensitivity of the submarine melt rate and the plume dynamics to a varying subglacial discharge we perform

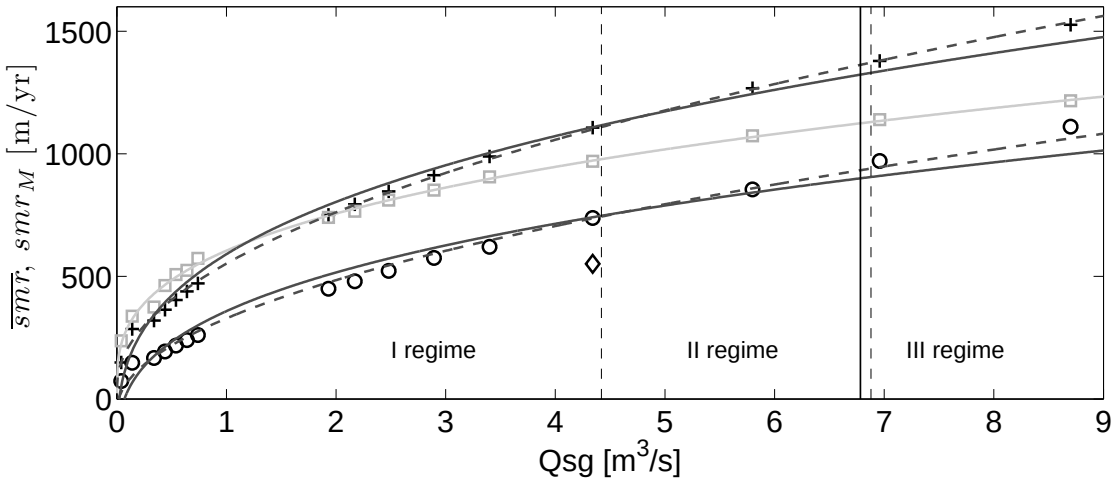

Figure 8.6: $\overline{smr}$ as a function of subglacial discharge, Qsg (SUMd). Black circles represent the MITgcm model and gray squares Jenkins [2011] 1D plume model. Black cross represent the maximum $\overline{smr}$. Black diamond indicates the SUMs experiment. Solid curves indicate the cubic root fit of $\overline{smr}$ for both analysis and the dashed curve indicate the square root fit for the SUMd runs. The vertical dashed lines refer to the different circulation regimes found in our simulations. The solid line is the theoretical location of $\rho_I = \rho_1$ (see section 8.7).

a series of experiments (SUMd). We find that both the average submarine melt rate ($\overline{smr}$) and its maximum (smr_M) increase with the square root of subglacial discharge (Figure 8.6). For the lowest values of subglacial discharge, $Qsg = 0.29$ m^3 s^{-1}, $\overline{smr} = 73$ m yr^{-1} which is similar to the value obtained for the WIN simulation (Table 8.1). Over the explored range of Qsg, our $\overline{smr}$ estimates are consistent with those obtained with Jenkins' 1D plume model (Figure 8.6, square symbols), and the difference in the power law exponent (cubic root vs. square root) are not statistically significant. The small differences can be explained by the slightly different vertical velocity distribution (Figure 8.5c). In particular, the larger magnitude of Jenkins' 1D model vertical velocities results in a larger $\overline{smr}$ (Figure 8.6). Furthermore, the inclusion of viscous term in our model give rise to a plume whose vertical velocity decreases as it rises. This is consistent with a slightly weaker dependence (square root) on Qsg than predicted by Jenkins (cubic root). Xu et al. [2012] also found a power law of $\sim 1/3$. We are not able to make a more detailed comparison with their results because of the minimal overlap in the range of subglacial discharge (Qsg) investigated. As the subglacial discharge increases, the dynamics at the glacier front evolve into three different regimes (Figure 8.7). For

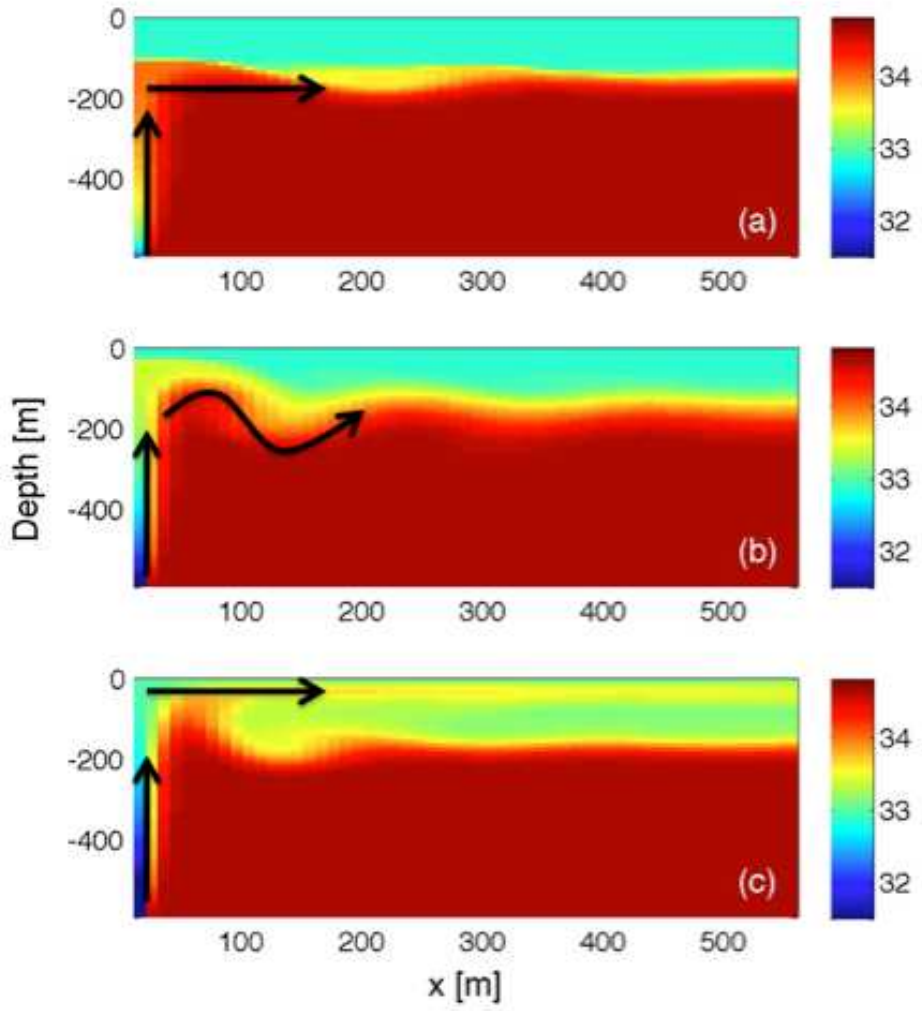

Figure 8.7: Salinity distribution near the glacier front (on the left side of the panels) in psu. (a) regime I: $Qsg = 0.74$ m^{3}s^{-1}, (b) regime II: $Qsg = 5.8$ m^{3}s^{-1}, (c) regime III: $Qsg = 8.7$ m^{3}s^{-1}. Black arrows indicates the plume water pathways.

low values of the subglacial discharge the dynamics is characterized by the same double cell circulation described in WIN with an enhanced outflow at the interface between the two water masses as described in section 8.6 (regime I, Figure 8.7a). This regime characterize Sermilik Fjord dynamics and is the main focus of the paper. For intermediate subglacial discharge values, the plume is more buoyant than in regime I and has larger vertical velocities which cause it to slightly overshoot the layers' interface generating a large amplitude interfacial wave (regime II, Figure 8.7b). Finally, for larger values of subglacial discharge, the plume is more buoyant than in regime II and is able to penetrate through the layers' interface and reach the free surface (regime III, Figure 8.7c). Regime III has been previously described, in a similar set–up, by Xu et al. [2012], who investigated the influence of large subglacial discharges, up to Qsg=250 $\mathrm{m^3\,s^{-1}}$. For the lowest value of subglacial discharge used, Xu et al. [2012] may have been in the intermediate regime II as suggested by the wave in the velocity field in their Figure 2a.

The value of Qsg for which the buoyant plume is able to penetrate through the layers' interface can be estimated as follows. A buoyant plume with an initial flow rate Qsg and an initial density ρ_{p0} changes its density through entrainment of ambient waters of density ρ_a. The flow rate of entrained ambient waters is defined as

$$Q_e = \int_{A_p} w_e \mathrm{d}A = \alpha w A_p, \tag{8.7.8}$$

where α is the entrainment coefficient, $w = 1.8(g'_0 Qsg)^{1/3}$ is the vertical velocity evaluated from the line plume theory [Turner, 1980], A_p is the area through which entrainment occurs defined as H_2 multiplied by the width of the fjord (L=10m), and $g'_0 = g(\rho_{p0} - \rho_a)/\rho_a$ is the initial reduced gravity. The density of the plume ρ_p is then given by

$$\rho_p(z) = \frac{\rho_{p0} Qsg + \rho_a Q_e}{Qsg + Q_e}, \tag{8.7.9}$$

and for a two–layer ambient stratification the buoyant plume will penetrate through the interface between the two layers if the density of the plume at the layers' interface $\rho_p(z = H_2) = \rho_I$ is lower than the density of the upper PW layer (ρ_1), i.e. $\rho_I < \rho_1$. Figure 8.6 shows

that the theoretical transition to regime III, i.e. $\rho_I = \rho_1$, occurs for $Qsg = 6.7\ \mathrm{m^3\,s^{-1}}$, which is in excellent agreement with the transition between regime II and III found in the model.

8.8 Influence of AW temperature and interface depth

Next, we consider the impact of variations in ocean properties on the submarine melt rate and the fjord circulation. Since the PW temperature is close to freezing, its contribution to the submarine melt rate is small. Hence, we focus our attention on three likely drivers of change: 1) the temperature of the AW, T_2, 2) its thickness H_2, and 3) its salinity S_2.

To investigate the impact of varying T_2, we performed a series of experiments where T_2, is varied from $0°C$ to $8°C$, while keeping the temperature of the upper layer and the salinity of both layers constant (TEMP and TEMPs runs). To investigate the influence of the relative thickness of the PW and AW layer, we varied the AW layer thickness H_2 between 50 m and 550 m (INTER and INTERs runs) while keeping all other parameters constant.

In the explored parameter range, we find that the structure of the circulation is not influenced by changes to T_2 and H_2, but that the $\overline{smr}$ increases linearly with T_2 and H_2 (Figure 8.8), both in winter (i.e. without subglacial discharge) and in summer (i.e. with subglacial discharge). A comparison with Jenkins' 1D plume model (Figure 8.8, square symbols) confirms a linear dependence of $\overline{smr}$ on T_2 and H_2. This linear dependence of submarine melt rate on T_2 is consistent with the scaling developed in Jenkins [2011] and the model results of Xu et al. [2012] who investigate only the summer season. As expected, we find that increasing H_2 is comparable to increasing the AW temperature T_2. For example, increasing the lower layer thickness from 450 m to 500 m is comparable to increasing the temperature of the AW by one degree from $4°C$ to $5°C$ (Figure 8.8). Holland et al. [2008] found a quadratic dependence of $\overline{smr}$ on water temperature and showed that previous results are highly variable and, depending on the nature of the study (e.g modeling, observations), the $\overline{smr}$ can have a linear or quadratic dependence on water temperature. We find that, in the

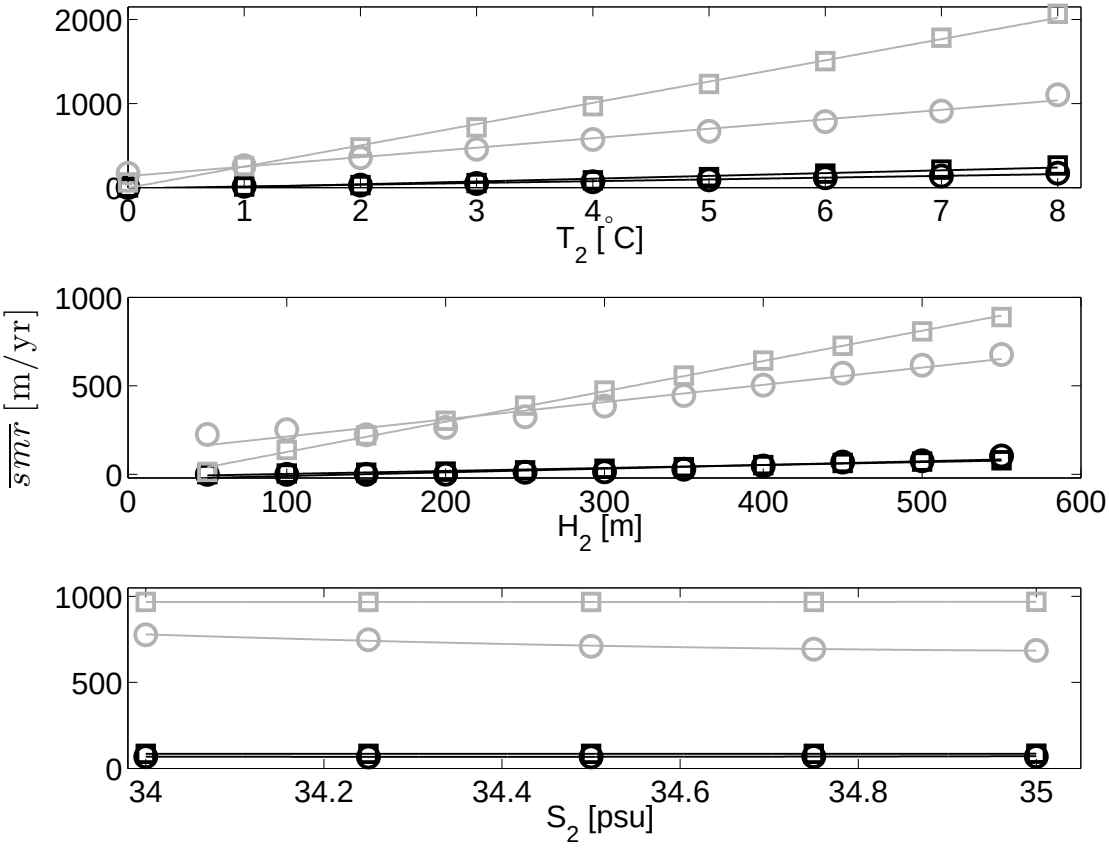

Figure 8.8: Vertically averaged submarine melt rate ($\overline{smr}$) as a function of T_2 and H_2. Gray (black) symbols denote experiment with (without) subglacial discharge. Circles represent the MITgcm model and squares the Jenkins [2011] 1D plume model. Solid lines are linear fits.

temperature range explored here, the difference between a quadratic and liner dependence is not statistically significant. We note that the dependence of the $\overline{smr}$ on H_2 deviates slightly from the linear dependence, and this subtle difference may be explained again by the vertical velocity dependence with depth found in our runs which is absent in Jenkins' 1D plume model (Figure 8.5c). Next we investigate the impact of changes in the AW salinity by varying S_2 in the range 34-35 psu (SALT and SALTs runs). From our own observations and historical data in the Irminger Sea (not shown), AW salinity variations are not likely to exceed this range. In summer, a 1 psu increase corresponds to a 13% decrease in $\overline{smr}$ from 776 m yr^{-1} to 686 m yr^{-1}. In winter, $\overline{smr}$ is less sensitive to AW salinity changes with a 4% decrease from 69 m yr^{-1} to 66 m yr^{-1} for a 1 psu increase (Figure 8.8). A 1 psu change in salinity impacts both the density of the AW layer and the freezing point temperature. The corresponding density change of ~ 0.79 kg m^{-3} at the base of the glacier is still much less than the PW/AW density difference, and similarly the freezing point temperature changes of only $0.05°C$. These variations are negligible compared to the dynamical effect of salinity on the plume. The plume buoyancy flux increases with increasing salinity resulting in a increase in the plume vertical velocity (see section 8.3). However, the plume will entrain denser water resulting in a higher plume density. Even though we observe a faster plume (not shown) which locally melts more the $\overline{smr}$ is less because the plume reaches its neutral buoyancy at a greater depth.

8.9 Discussion and Conclusions

We use a fjord scale, non-hydrostatic general circulation model to investigate the circulation and submarine melt rate resulting from the presence of a glacier at the head of a long, deep fjord. The set–up is meant to be an idealized representation of the Sermilik Fjord/Helheim Glacier system in East Greenland. We examine variations forced by changes in the properties of the two water masses observed in the fjord (the cold, fresh Polar Water layer and the warm, salty Atlantic Water layer) and in the rate of subglacial discharge.

Our simulations indicate that the fjord's two–layer stratification

gives rise to a double cell circulation where relatively fresh water (containing glacial melt) is exported both at the free surface and at the interface between the two water masses. Hence, large amounts of glacially modified waters are exported below the PW layer. Even though the general structure of the circulation is the same in summer and winter, our results indicate that both the vertical distribution and magnitude of the submarine melt rate vary strongly from summer to winter. In summer, the rate of submarine melt is an order of magnitude larger than in winter, and it is maximum at the glacier's base while it is maximum at the interface between the two water masses in winter. These differences are primarily due to the large subglacial discharge that occurs in summer. This discharge results in a large and fast buoyant plume, which in turn, enhances the submarine melt rate along the glacier front by affecting the ice-ocean transfer processes. Physically, the summer plume is much more buoyant, resulting in a more turbulent plume with larger entrainment rates and larger transport of heat towards the glacier. In winter, the only buoyancy forcing is due to melting of the glacier itself, giving rise to a less buoyant and slower plume. As a result, the vertically averaged submarine melt rate is an order of magnitude smaller than in summer. Substantial changes in the submarine melt rate can also result from changes in the Atlantic Water layer thickness and temperature, while the Atlantic Water salinity has a smaller impact on the dynamics and the submarine melt rate. Our results show that vertically averaged submarine melt rate varies with the square root of the subglacial discharge, and linearly with the Atlantic water temperature and layer's thickness.

Our results are in fairly good agreement with the cubic-root scaling developed by Jenkins [2011] and Jenkins' 1D plume model, indicating that simplified one-dimensional plume models are a useful tool to understand the first order dynamics regulating the melting at the glacier front. The use of a general circulation model presents some advantages when compared to the simpler plume model in that we could identify different regimes of the circulation driven by the glacier itself. A scaling argument indicates that to generate the 'double cell' circulation characterizing Sermilik Fjord dynamics (regime I), the buoyant plume density at the layers' interface ρ_I must be less than the density of the upper PW layer which, for the parameters of Sermilik Fjord,

occurs for $Qsg < 6.7$ $\mathrm{m^3\,s^{-1}}$, in excellent agreement with our simulation (Figure 8.6). Our results are also consistent with some of the findings of Xu et al. [2012]. In their study, however, they focused on a regime in which the melt water plume penetrates all the way to the ocean free surface and generates a single outflowing current which is approximately 100 m deep and with very large horizontal velocities (of the order of 2 $\mathrm{m\,s^{-1}}$). Such circulation and large velocities are not observed in Sermilik Fjord and therefore it is unlikely that Xu et al. [2012] results are applicable to Sermilik and similar environments.

Our estimates indicate that the summer melt rates are of the order of 700 $\mathrm{m\,yr^{-1}}$ while winter melt rates are about 70 $\mathrm{m\,yr^{-1}}$ and that this difference is largely due to subglacial discharge. Caution must be used, however, in converting these estimates to average values over the entire submerged front of a glacier such as Helheim since they were obtained for a 10 m wide glacier. In winter, when there is no subglacial discharge, we expect the 10 m wide glacier to be representative of the entire portion of the glacier in contact with the ocean. Therefore, the 70 $\mathrm{m\,yr^{-1}}$ melt rate estimate *is* likely to be representative of a mean melt rate for Helheim as long as the transfer coefficients used in the ice/ocean boundary layer parameterization are appropriate. In summer, however, the estimate of 700 $\mathrm{m\,yr^{-1}}$ melt rate is only appropriate for the fraction of the glacier characterized by a large subglacial discharge, and not necessarily for the entire glacier front. Thus, even though it is tempting to compare the summer melt rate with the recent estimate of 400-1000 $\mathrm{m\,yr^{-1}}$ obtained using synoptic velocity and temperature profiles collected in Sermilik Fjord during summer 2009 [Sutherland and Straneo, 2012], the comparison *is not* appropriate. Given that the model based estimate is only representative of a portion of the glacier, one could speculate that average melt rates across the entire glacier front should be considerably less and thus at odds with the field based estimate. For example, one should consider a 700 $\mathrm{m\,yr^{-1}}$ over 400 m and 70 $\mathrm{m\,yr^{-1}}$ over the remaining glacier's width which results in a $\overline{smr} = 112$ $\mathrm{m\,yr^{-1}}$. On the other hand, the field based estimate of Sutherland and Straneo [2012], is indicative of the quasi-instantaneous (field data were obtained in less than a week) melt rate averaged across the entire glacier front. In practice, there are multiple reasons why we should be cautious about making this

comparison. First, the data based estimate itself is highly uncertain and based on a snapshot of conditions inside the fjord. Furthermore, it is important to remember that the model simulations are highly idealized in nature and only consider the circulation driven by the glacier itself. A potentially important dynamical feature neglected in the model simulation is, for example, the fast and rapidly changing continental shelf-forced circulation observed in Sermilik Fjord [Straneo et al., 2010, Sutherland and Straneo, 2012]. A second, likely source of discrepancies is due to the fact that the turbulent transfer coefficients are largely untested in Greenlands tidewater glacier environment.

Several important simplifications have been made in this study. First, we have assumed that the leading order dynamics is two-dimensional. This assumption is justified for the fjord scale circulation but is questionable for localized subglacial discharges which may introduce spatial asymmetries in the problem, something which needs to be investigated further. Second, large uncertainties remain regarding the timing and magnitude of the subglacial discharge. Here, we have made an attempt to cover what we consider is a realistic dynamical range. Yet until the uncertainties on these numbers are reduced, it is hard to identify an appropriate dynamical regime. Third, we have assumed that even though the model does not explicitly resolve the smaller turbulent scales of the problem, their integral effect is captured by the parameterizations of eddy viscosity and diffusivity. We have presented a scaling argument which supports this assumption in the dynamical range explored here, but further studies with even higher resolution models are needed. Fourth, key to these experiments is an appropriate parameterization of the ice-ocean boundary. This study shows that the submarine melt rate and its vertical structure can vary substantially depending on the choice of parameters and variables in the turbulent transfer coefficients. Given our present knowledge of the turbulent transfer coefficients, our results indicate that a correct estimate of the vertical velocities is crucial to represent the ice-ocean dynamics and the submarine melt rate, in particular. More work is needed to determine whether the parameterization of this dynamics is appropriate for models that cannot resolve the small-scale non-hydrostatic boundary layer processes at the ice-ocean interface. Our results suggests that models such as the one used here could help bridge the gap be-

tween small-scale and large-scale models that are unlikely to resolve the dynamics at the ice-ocean boundary. For example, the derived relationship between submarine melt rates and subglacial discharge (Figure 8.6) could be integrated in the melt rate parameterizations for large-scale models. A formulation not depending on near-ice front vertical velocities might also lend itself for inclusion in isopycnal models with a fundamentally different vertical discretization (e.g. Adcroft and Hallberg [2006]) and implied plume and entrainment parameterization.

Albeit very simplified, this study illustrates the suitability of using a GCM to investigate the dynamics driving glacier melting and is the necessary step to investigate the importance of fjord circulations on the dynamics near a glacier front. We find that the inclusion of a variable velocity in the turbulent transfer coefficients is fundamental to capture the seasonal variability of the vertical structure of $\overline{smr}$. Larger subglacial discharge, induce larger vertical velocity and a resulting larger submarine melt rate. Hence, the quantification of the subglacial discharge and the number and size of drainage channels is fundamental for a correct prediction of submarine melting and fjord circulation. By varying the AW layer thickness from 450 m to 500 m we find that the submarine melt rate is increased by the same amount as if the temperature of the AW was increased by one degree from $4°C$ to $5°C$. Hence, the displacement of the interface between AW and PW may be as, if not more, important than a temperature change in the AW layer.

Finally, these idealized experiments have neglected a whole range of oceanic/fjord processes which likely have a strong impact on the heat transport to the glacier and hence the submarine melt rate. These include circulations forced by continental shelf and atmospheric variability at the mouth, local winds and tides. The interaction between these circulations and the buoyancy driven circulation described here is the subject of ongoing research. Such process studies are crucial to improve our understanding of the dynamic response of Greenland's outlet glaciers to oceanic and atmospheric forcings [Straneo et al., 2013].

Chapter 9

Conclusion

9.1 Summary

In this thesis I have explored, using different numerical approaches, the role of turbulence in two oceanic systems of climatic relevance.
In the first part I have looked at the influence of turbulence in shaping the distribution and composition of planktonic communities in the ocean.
The second part was focused on the high-latitude dynamics of Greenland fjords. I have addressed the role of ice-ocean boundary processes in influencing the submarine ice melting and fjord circulation.

In chapter 4 I have investigated the settling of particles in a homogeneous and isotropic turbulent environment, simulated by the direct numerical integration of the Navier-Stokes equations. I have addressed the role of particle density, given that plankton particles are only slightly heavier than ocean water. Using different measures we found that, in the range of explored parameters, variations in particle density can lead to preferential concentration not only in downdrafts but also in the updrafts and therefore to temporary particle suspension. This behavior is relevant in situations where particles undergo processes that depend on their vertical position, such as for phytoplankton in aquatic environments, which can photosynthesize only in the euphotic layer close to the surface.

In chapter 5 I have introduced a parametrization for turbulence in a simplified ecosystem model to explore how sinking affects the outcome of phytoplankton competition. Larger species, which would be biologically disadvantaged, can instead be favoured by turbulence when sinking is slower owing for example to turbulent suspension or

to the presence of upwelling. The same behaviour is observed in presence of intermittent spatial and temporal sinking conditions due for example to mesoscale vortices or fronts.

In chapter 6 I have discussed a simplified mathematical model describing the dynamics of the alpine lake ecosystems. Model outputs are compared with measurements recorded in twelve high–altitude mountain lakes in the Gran Paradiso National Park during the summer season from 2006 to 2009. Model results are consistent with measured data, indicating the appropriateness of this modeling approach for quantitatively studying mountain lake ecosystems and their response to environmental changes.

In chapter 8 I have presented a high resolution non-hydrostatic model to study the impact of fjord dynamics on a Greenland glacier. Submarine melting of Greenland's glaciers has emerged as a key term in the ice sheet's mass balance and as a plausible trigger for their recent acceleration. The simulations support the hypothesis that the circulation in the fjords is more complex than just the result of simple dependence on water temperature. A double cell circulation, generated by a plume of subglacial discharge, submarine meting and entrained ambient waters, is observed year round and is strongly dependent on the turbulent transfer parametrization between the ice and the ocean. Moreover, this work has elucidated the dynamics of buoyant plumes close to the ice edge and the numerical requirements to properly resolve such processes in non-hydrostatic models.

Starting from these personal works I have explored the role of oceanic turbulence, further interesting questions can be addressed in the future. In the following I will enumerate some of them.

9.2 Outlook

Further studies should be done to better explore some of the following aspects:

(i) The role of turbulence on ecosystem dynamics was elucidated in highly simplified models. It would be interesting to introduce an ecosystem model in regional circulation models with higher resolution, capable of properly representing the pattern of upwelling and downwelling and of parametrizing the level of turbulence.

(ii) Plankton zoology is complex and particles are nothing but spherical. Further studies would be necessary to better explore the parameter space and particle shapes. Introducing an equation of motion for non spherical particles can change the dynamics and therefore influence the settling rates of phytoplankton particles.

(iii) Boundary layer processes between the ice and the ocean emerged as a key feature of glacier dynamics. Boundary layer velocities control the turbulent transfer processes between the ice and the ocean. Therefore developing a high resolution parametrization of entrainment processes would improve the estimate of plume velocities as well as the generated submarine melting.

(iv) Data have shown that Greenland fjords are closely linked to the shelf dynamics. Thus by nesting the high resolution fjord model in a coarser model of the shelf, one can study the influence of external variability on submarine melting. Of particular interest are the role of passing storms and tides.

Acknowledgements

Il dottorato é un viaggio nel senso piú vero del termine, un viaggio umano e lavorativo. Il mio viaggio mi ha portato in tanti luoghi, mi ha permesso di vivere tante esperienze lavorative e umane e conoscere persone che altrimenti non avrei mai conosciuto.
Vorrei ringraziare la persona con la quale questo viaggio lavorativo é iniziato, Antonello Provenzale, per il supporto, il confronto e le infinite possibilitá datemi in questi anni.
I would like to thank my new group: Fiamma Staneo, Claudia Cenedese, Patrick Heimbach with whom I've traveled the world of ice. Thanks for being great mentors, for all the opportunities and for helping my scientific evolution.
Vorrei ringraziare tutte le persone con le quali ho lavorato in questi anni. Fra tutte Claudia Pasquero per i consigli e il confronto.
Grazie a tutto I'ISAC-CNR di Torino. Un grazie particolare a Jost per le due summer school passate assieme, a Guido Boffetta per la disponibilitá e, a Donatella e Gabriella per essere state due stupende segretarie sempre pazienti e gentili.
Vorrei ringraziare il collegio docenti del dottorato in Fluidodinamica del Politecnico di Torino, il coordinatore Prof. Gaetano Iuso, e tutto il personale del DIASP. Un grazie particolare a Vilma Boaglio.
Un viaggio ha bisogno di gradi compagni, e lungo la strada ne ho trovati tanti che non dimenticheró mai.
Grazie alla mia unica e sola compagna di ufficio, grazie Mara. Grazie per il confronto scientifico, per i consigli da zia, per le bacchettate quando ce n'é stato bisogno, grazie per i momenti Rob, grazie per essere la mia compagna di ufficio anche con un oceano di mezzo ma sopratutto grazie per essere prima di tutto un'amica.
Caterina,Tosa, grazie per essere stata non solo una compagna di dottorato, di studio, di summer school ma una compagna di risate, di serate passate assieme, di chiacchierate al telefono ritornando a casa.

Grazie per aver condiviso questi anni assieme.
Valentina, grazie, perché il mio dottorato é iniziato e finito con te, perché ho scoperto un'amica, per l'extreme-terme, per le serate cena-film, per esserci stata quando piú ne avevo bisogno.
Sabino grazie per i laghi, per la cremina, per la puglia in ufficio. Un giorno tutto questo sará tuo.
Grazie a tutte quelle persone che ho incontrato lungo la strada e che difficilmente dimenticheró: Marta, Lara, Davide Proment, Elisa, Marco Cisternino.
I would like to thank my new American family. Thanks to you I've realized that home can be anywhere. Thanks Laura, Diane, Chiara, Anita, Meg, Liz, Wilken, Elise, Simon, Daniel. And all the people at WHOI and EAPS.
E poi c'é il porto sicuro, quello dove ritorni sempre, casa. Vorrei ringraziare la mia famiglia per esserci sempre stata. La mia mamma e il mio papá, per l'amore incondizionato, per i sacrifici non ultimo quello di avere una figlia con -6 ore di fuso.
Vorrei ringraziare i miei amici di sempre, quelli dei banchi di scuola, quelli con cui sono cresciuta, che sempre ci saranno e per cui sempre ci saró: Adriana, Marco, Riccardo.
Grazie ai nuovi amici che negli ultimi anni sono diventati una presenza importante e fondamentale. Grazie per tutte le cene, le vacanze assieme, le risate: Chantal, Nadia, Nickj, Luca, Gianluca, Cristina.
Grazie ai fisici perché anche se siamo sempre piú distanti e sparpagliati per il mondo siamo sempre noi, anche solo per una cena di Natale. Grazie Ale Sola, Il Lava, Carla, EleLanzi, Pennaz, Mario, Mauro.
E non ultimo grazie a Davide per essere stato prima di tutto un amico e una presenza costante. Grazie per il viaggio che stiamo facendo insieme. É il viaggio piú imprevedibile, bello ed emozionante che possa immaginare.

Bibliography

O. Reynolds. An experimental investigation of the circumstances which determine whether the motion of water shall be direct or sinuous, and of the law of resistance in parallel channels. *Royal Society of London Philosophical Transactions Series I*, 174:935–982, 1883.

O. Reynolds. On the dynamical theory of incompressible viscous fluids and the determination of the criterion. *Royal Society of London Philosophical Transactions Series A*, 186:123–164, 1895.

S.A. Thorpe. *An introduction to ocean turbulence.* Cambridge University Press, 2007.

E. M. Purcell. Life at low Reynolds number. *American Journal of Physics*, 45(1):3–11, 1977.

W. Munk and G. A. Riley. Absorption of nutrients by aquatic plants. *Journal of Marine Research*, 11:215–240, 1952.

U. Sommer. Some size relationship in phytoplankton mortality. *Hydrobiologia*, 161:125–131, 1988.

J.R.N Lazier and K.H. Mann. Turbulence and the diffusive layers around small organisms. *Deep Sea Research Part A. Oceanographic Research Papers*, 35:1247–1253, 1989.

H. Stommel. Trajectories of small bodies sinking slowly through convection cells. *J. Mar. Res.*, 8:24–29, 1949.

M.R. Maxey and S Corrsin. Gravitational settling of aerosol particles in randomly oriented cellular flow fields. *J. Atmos. Sci*, 43:1112–1134, 1986.

C Pasquero, A Provenzale, and EA Spiegel. Suspension and fall of heavy particles in random two-dimensional flow. *Phys. Rev Lett.*, 91, 2003.

M.R. Maxey. The gravitational settling of aerosol-particles in homogeneous turbulence and random flow fields. *J. Fluid Mech.*, 174: 441–465, 1987.

L.P. Wang and M.R. Maxey. Settling velocity and concentration distribution of heavy particles in homogeneous isotropic turbulence. *J. Fluid Mech.*, 256:27–68, 1993.

J Ruiz, D Macias, and F Peters. Turbulence increases the average settling velocity of phytoplankton cells. *Proc. Natl. Acad. Sci. U. S. A.*, 101:17720–17724, 2004.

E Deleersnijder, JM Beckers, and EJM Delhez. The residence time of settling particles in the surface mixed layer. *Environ. Fluid Mech.*, 6:25–42, 2006.

Marco Martins Afonso. The terminal velocity of sedimenting particles in a flowing fluid. *J. Phys. A: Math. Theor.*, 41, 2008.

J. C. H. Fung. Gravitational settling of particles and bubbles in homogeneous turbulence. *j. Geophys. Res.*, 98:20,287–20,297, 1993.

Noh et al. Large eddy simulation of particle settling in the ocean mixed layer. *Phys. Fluids*, 18:085109, 2006.

Q. Zhou and N. S. Cheng. Experimental investigation of single particle settling in turbulence generated by oscillating grid. *Chemical Engineering Journal*, 149(1-3):289–300, 2009.

MR Maxey and JJ Riley. Equation of motion for a small rigid sphere in a nonuniform flows. *Phys. Fluids*, 26:883–889, 1983.

V Armenio and V Fiorotto. The importance of the forces acting on particles in turbulent flows. *Phys. Fluids*, 13:2437–2440, 2001.

M Cencini, J Bec, L Biferale, G Boffetta, A Celani, AS Lanotte, S Musacchio, and F Toschi. Dynamics and statistics of heavy particles in turbulent flows. *J. Turbul.*, 7:1–16, 2006.

J Davila and JCR Hunt. Settling of small particles near vortices and in turbulence. *J. Fluid Mech.*, 440:117–145, 2001.

J.L. Snyder, W.H. & Lumley. Some measurements of particle velocity auto-correlation functions in a turbulent flow. *J. Fluid Mech.*, 48: 41–71, 1971.

Peter Nielsen. Mean and variance of the velocity of solid particles in turbulence. In *Particle-Laden Flow*, pages 385–391. Springer, 2007.

T.J. Smayda. The suspension and sinking of phytoplankton in the sea. *Oceanogr. Mar. Biol. Ann. Rev.*, 8:353–414., 1970.

Daniela N. Schmidt, David Lazarus, Jeremy R. Young, and Michal Kucera. Biogeography and evolution of body size in marine plankton. *Earth-Science Reviews*, 78(3-4):239–266, 2006.

Elena Litchman, Christopher A. Klausmeier, Oscar M. Schofield, and Paul G. Falkowski. The role of functional traits and trade-offs in structuring phytoplankton communities: scaling from cellular to ecosystem level. *Ecology Letters*, 10(12):1170–1181, 2007.

Paul G. Falkowski and Matthew J. Oliver. Mix and match: how climate selects phytoplankton. *Nature Reviews Microbiology*, 5(10): 813–819, 2007.

Kohei Yoshiyama and Christopher A. Klausmeier. Optimal cell size for resource uptake in fluids: A new facet of resource competition. *American Naturalist*, 171(1):59–70, 2008.

L Jiang, OME Schofield, and PG Falkowski. Adaptive evolution of phytoplankton cell size. *American Naturalist*, 166(4):496–505, 2005.

C Pasquero, A Bracco, and A Provenzale. Impact of the spatiotemporal variability of the nutrient flux on primary productivity in the ocean. *Journal of geophysical research-oceans*, 110(C7), 2005.

R Margalef. Life-forms of phytoplankton as survival alternatives in an unstable environment. *Oceanologica Acta*, 1(4):493–509, 1978.

J Huisman, M Arrayas, U Ebert, and B Sommeijer. How do sinking Phytoplankton species manage to persist? *American Naturalist*, 159 (3):245–254, 2002.

M Estrada and E Berdalet. Phytoplankton in a turbulent world. *Scientia Marina*, 61(Suppl. 1):125–140, 1997.

L Peperzak, F Colijn, R Koeman, WWC Gieskes, and JCA Joordens. Phytoplankton sinking rates in the Rhine region of freshwater influence. *Journal of plankton research*, 25(4):365–383, 2003.

RRP Chase. Settling behavior of natural aquatic particulates. *Limnology and oceanography*, 24(3):417–426, 1979.

L Stemmann, GA Jackson, and D Ianson. A vertical model of particle size distributions and fluxes in the midwater column that includes biological and physical processes - Part I: model formulation. *Deep-Sea Research Part I - Oceanographic Research Papers*, 51(7):865–884, JUL 2004.

Lionel Guidi, George A. Jackson, Lars Stemmann, Juan Carlos Miquel, Marc Picheral, and Gabriel Gorsky. Relationship between particle size distribution and flux in the mesopelagic zone. *Deep-Sea Research Part I - Oceanographic Research Papers*, 55(10):1364–1374, 2008.

Edward A. Laws. The importance of respiration losses in controlling the size distribution of marine phytoplankton. *Ecology*, 56(2):419–426, 1975.

Alexandrine Pannard, Myriam Bormans, Sebastien Lefebvre, Pascal Claquin, and Yvan Lagadeuc. Phytoplankton size distribution and community structure: influence of nutrient input and sedimentary loss. *Journal of plankton research*, 29(7):583–598, 2007.

Christoph G. Jaeger, Sebastian Diehl, and Gertraud M. Schmidt. Influence of water-column depth and mixing on phytoplankton biomass, community composition, and nutrients. *Limnology and oceanography*, 53(6):2361–2373, 2008.

Antonello Provenzale. Transport by coherent barotropic vortices. *Annual Review of Fluid Mechanics*, 31(1), 1999.

P. Tanga and A. Provenzale. Dynamics of advected tracers with varying buoyancy. *Physica D: Nonlinear Phenomena*, 76(1–3):202–215, 1994.

P. J. Thomas. On the influence of the basset history force on the motion of a particle through a fluid. *Physics of Fluids A: Fluid Dynamics*, 4(9):2090–2093, 1992.

O. A. Druzhinin and L. A. Ostrovsky. The influence of basset force on particle dynamics in two-dimensional flows. *Physica D: Nonlinear Phenomena*, 76(1–3):34–43, 1994.

T. Brooke Benjamin. Note on added mass and drift. *Journal of Fluid Mechanics*, 169:251–256, 1986.

A.Srdic. *Interaction of dense particles with stratified and turbulent environment*. PhD thesis, ArizonaStateUniversity, 1999.

R. Mallier and M. Maxey. The settling of nonspherical particles in a cellular flow field. *Physics of Fluids A: Fluid Dynamics*, 3(6): 1481–1494, 1991.

T.J. Smayda. Normal and accelerated sinking of phytoplankton in the sea. *Marine Geology*, 11(2):105–122, 1971.

Judit Padisák, Éva Soróczki-Pintér, and Zsuzsanna Rezner. Sinking properties of some phytoplankton shapes and the relation of form resistance to morphological diversity of plankton – an experimental study. *Hydrobiologia*, 500:243–257, 2003.

Alice L. Alldredge and Chris Gotschalk. In situ settling behavior of marine snow. *Limnology and Oceanography*, 33(3):339–351, 1988.

H Ploug and H P Grossart. Bacterial growth and grazing on diatom aggregates: Respiratory carbon turnover as a function of aggregate size and sinking velocity. *Li*, 45(7):1467–1475, 2000.

K Van den Meersche, JJ Middelburg, K Soetaert, P van Rijswijk, HTS Boschker, and CHR Heip. Carbon-nitrogen coupling and algal-bacterial interactions during an experimental bloom: Modeling a C-13 tracer experiment. *Limnology and oceanography*, 49(3):862–878, 2004.

RW Eppley. Half-satutration constants for uptake of nitrate and ammonium by marine phytoplankton. *Agriculture biology and environmental sciences*, 43:A11–A12, 1979.

JA Raven. Why are there no picoplanktonic O(2) evolvers with volumes less-than 10(-19) M(3). *Journal of plankton research*, 16(5): 565–580, 1994.

EPY Tang. The allometry of algal growth-rates. *Journal of plankton research*, 17(6):1325–1335, 1995.

G. E. Hutchinson. The paradox of the plankton. *The American Naturalist*, 95(882):137–145, 1961.

D Tilman and JA Downing. Biodiversity and stability in grasslands. *Nature*, 367(6461):363–365, 1994.

AP Martin. Phytoplankton patchiness: the role of lateral stirring and mixing. *Progress in oceanography*, 57(2):125–174, 2003.

Andrew D. Barton, Stephanie Dutkiewicz, Glenn Flierl, Jason Bragg, and Michael J. Follows. Patterns of diversity in marine phytoplankton. *Science*, 327(5972):1509–1511, March 2010.

I Koszalka, A Bracco, JC McWilliams, and A Provenzale. Dynamics of wind-forced coherent anticyclones in the open ocean. *J. Geophys. Res. - Oceans*, 114(C08011), 2009. doi: 10.1029/2009JC005388.

Michael J. Follows, Stephanie Dutkiewicz, Scott Grant, and Sallie W. Chisholm. Emergent biogeography of microbial communities in a model ocean. *Science*, 315(5820):1843–1846, 2007.

M. Levy, P. Klein, and A.-M. Treguier. Impact of sub-mesoscale physics on production and subduction of phytoplankton in an oligotrophic regime. *J. Marine Res.*, 59:535–565, 2001.

N. Gruber, H. Frenzel, S.C. Doney, P. Marchesiello, J.C. McWilliams, J.R. Moisan, J.J. Oram, G.-K. Plattner, and K.D. Stolzenbach. Eddy-resolving simulation of plankton ecosystem dynamics in the california current system. *Deep Sea Res.*, 53:1483–1516, 2006.

M Estrada, M Alcaraz, and C Marrasé. Effects of turbulence on the composition of phytoplankton assemblages in marine microcosm. *Mar. Ecol. Prog. Ser.*, 38:267–281, 1987.

M. Beniston, H.F. Diaz, and R.S. Bradley. Climatic change at high elevation sites: An overview. *Climatic Change*, 36(3/4):233–251, 1997.

Sabine Sommaruga-Wograth, Karin A. Koinig, Roland Schmidt, Ruben Sommaruga, Richard Tessadri, and Roland Psenner. Temperature effects on the acidity of remote alpine lakes. *Nature*, 387 (6628):64–67, 05 1997.

Brian R. Parker, Rolf D. Vinebrooke, and David W. Schindler. Recent climate extremes alter alpine lake ecosystems. *Proceedings of the National Academy of Sciences*, 105(35):12927–12931, 2008.

M.J. Boavida and Z. M. Gliwicz. Limnological and biological characteristics of the alpine lakes of portugal. *Limnetica*, 12(2):39–45, 1996.

Roland A. Knapp, Kathleen R. Matthews, and Orlando Sarnelle. Resistance and resilience of alpine lake fauna to fish introductions. *Ecological Monographs*, 71(3):401–421, 2001.

Lars Håkanson. Optimal size of predictive models. *Ecological Modelling*, 78(3):195–204, 1995.

R. Tiberti, G. A. Tartari, and A. Marchetto. Geomorphology and hydrochemistry of 12 alpine lakes in the gran paradiso national park, italy. *Journal of Limnology*, 69(2):242–256, 2010.

R. Tiberti. *Master thesis*. University of Pavia, 2007.

C.S. Reynolds. *Ecology of phytoplankton*. Cambridge University Press, 2006.

Cristiana Callieri, Gianluca Corno, and Roberto Bertoni. Bacterial grazing by mixotrophic flagellates and daphnia longispina: a comparison in a fishless alpine lake. *Aquatic Microbial Ecology*, 42(2): 127–137, 2006.

M. Yúfera, G. Parra, and E. Pascual. Energy content of rotifers (brachionus plicatilis and brachionus rotundiformis) in relation to temperature. *Hydrobiologia*, 358:83–87, 1997.

R. Tiberti. Morphology and ecology of daphnia middendorffiana, fisher 1851 (crustacea, daphniidae) from four new populations in the alps. *Journal of Limnology*, 70(2), 2011.

R. Tiberti and von Hardenberg A. Impact of introduced fish on common frog (rana temporaria) close to its altitudinal limit in alpine lakes. *Amphibia-Reptilia*, 33:303–307, 2012.

R. Tiberti. *Ecology of alpine lakes in Gran Paradiso National Park*. PhD thesis, University of Pavia, 2012.

Rocco Tiberti and Rocco Iacobuzio. Does fish predation influence the vertical distribution of zooplankton in high transparency, shallow lakes? *Hydrobiologia*, page in press, 2012.

Wolf Mooij, Dennis Trolle, Erik Jeppesen, George Arhonditsis, Pavel Belolipetsky, Deonatus Chitamwebwa, Andrey Degermendzhy, Donald DeAngelis, Lisette De Senerpont Domis, Andrea Downing, J. Elliott, Carlos Fragoso, Ursula Gaedke, Svetlana Genova, Ramesh Gulati, Lars Håkanson, David Hamilton, Matthew Hipsey, Jochem 't Hoen, Stephan Hülsmann, F. Los, Vardit Makler-Pick, Thomas Petzoldt, Igor Prokopkin, Karsten Rinke, Sebastiaan Schep, Koji Tominaga, Anne Van Dam, Egbert Van Nes, Scott Wells, and Jan Janse. Challenges and opportunities for integrating lake ecosystem modelling approaches. *Aquatic Ecology*, 44, 2010.

Sven Erik Jørgensen. A review of recent developments in lake modelling. *Ecological Modelling*, 221(4), 2010.

R. G. Wetzel. *Limnology – Lake and River Ecosystems*. Elsevier Academic Press, 2001.

O. Vadstein and Y. Olsen. Chemical composition and phosphate uptake kinetics of limnetic bacterial communities cultured in chemostats under phosphorus limitation. *Limnology and Ocenaography*, 34(939-946), 1989.

Franck Touratier, John G Field, and Coleen L Moloney. A stoichiometric model relating growth substrate quality (c:n:p ratios) to n:p ratios in the products of heterotrophic release and excretion. *Ecological Modelling*, 139(2–3):265–291, 4 2001.

K. Vrede, M. Heldal, S. Norland, and G. Bratbak. Elemental composition (c, n, p) and cell volume of exponentially growing and nutrient-limited bacterioplankton. *Applied and Environmental Microbiology*, 68, 2002.

E.M. Smith and Y.T. Prairie. Bacterial metabolism and growth efficiency in lakes: The importance of phosphorus availability. *Limnology and Ocenaography*, 49, 2004.

Theis Kragh, Morten Søndergaard, and Lars Tranvik. Effect of exposure to sunlight and phosphorus-limitation on bacterial degradation of coloured dissolved organic matter (cdom) in freshwater. *FEMS Microbiology Ecology*, 64(2):230–239, 2008.

A. Lyche, T. Andersen, K. Christoffersen, D.O. Hessen, P.H Berger Hansen, and A. Klysner. Mesocosm tracer studies. 1. zooplankton as sources and sinks in the pelagic phosphorus cycle of a mesotrophic lake. *Limnology and Ocenaography*, 41(460-474), 1996.

RS Rasmussen and TH Ostenfeld. Effect of growth rate on quality traits and feed utilisation of rainbow trout (oncorhynchus mykiss) and brook trout (salvelinus fontinalis). *Aquaculture (Amsterdam, Netherlands)*, 184(3/4), 2000.

R.S. Rasmussen, T.H. Ostenfeld, and E. McLean. Growth and feed utilisation of rainbow trout subjected to changes in feed lipid concentrations. *Aquaculture International*, 8, 2000.

A.C. Baudoux. The role of viruses in marine phytoplankton mortality. Master's thesis, University of Groningen, 2007.

Hildegard E. Enesco. Rotifers in aging research: use of rotifers to test various theories of aging. *Hydrobiologia*, 255-256:59–70, 1993.

Tatsuki Yoshinaga, Gen Kaneko, Shigeharu Kinoshita, Satoshi Furukawa, Katsumi Tsukamoto, and Shugo Watabe. Insulin-like growth factor signaling pathway involved in regulating longevity of rotifers. In *Rotifera X*, volume 181, pages 347–352. Springer Netherlands, 2005.

R.A. Myers and J.A. Runge. Predictions of seasonal natural mortality rates in a copepod population using life-history theory. *Marine Ecology Progress Sereries*, 11, 1983.

Green AS, Chandler GT, and Coull BC. Age-specific survival analysis of an infaunal meiobenthic harpacticoid copepod, amphiascus tenuiremis. *Marine Ecology Progress Series*, 129, 1995.

S. Nandini and S. S. S. Sarma. Lifetable demography of four cladoceran species in relation to algal food (chlorella vulgaris) density. *Hydrobiologia*, 435, 2000.

JoséLuis Gama-Flores, S. S. S. Sarma, and S. Nandini. Exposure time-dependent cadmium toxicity to moina macrocopa (cladocera): a life table demographic study. *Aquatic Ecology*, 41(4):639–648, 2007.

Orlando Sarnelle and Alan E. Wilson. Type iii functional response in daphnia. *Ecology*, 89(6):1723–1732, 2008.

KL Denman. Modelling planktonic ecosystems: parameterizing complexity. *Progress in Oceanography*, 57:429–452, 2003.

J. Steele and E. Henderson. The role of predation in plankton models. *J. Plankton Research*, 14:157–172, 1992.

Y Olsen, A Jensen, H Reinertsen, KY Borsheim, M Heldal, and A Langeland. Dependence of the rate of release of phosphorus by zooplankton on the p : C ratio in the food supply, as calculated by a recycling model. *Limnology and Ocenaography*, 31(1):34–44, 1986.

Urs Uehlinger. Bacteria and phosphorus regeneration in lakes. an experimental study. *Hydrobiologia*, 135:197–206, 1986.

N.G. Hairston, F.E. Smith, and L.B. Slobodkin. Community structure,population control and competition. *American Naturalist*, 94 (879):421–425, 1960.

E. Rignot, J. E. Box, E. Burgess, and E. Hanna. Mass balance of the Greenland ice sheet from 1958 to 2007. *Geophys. Res. Lett.*, 35: L20502, 2008. doi: 10.1029/2008GL035417.

Eric Rignot and Pannir Kanagaratnam. Changes in the Velocity Structure of the Greenland Ice Sheet. *Science*, 311(5763):986–990, 2006.

Michiel van den Broeke, Jonathan Bamber, Janneke Ettema, Eric Rignot, Ernst Schrama, Willem Jan van de Berg, Erik van Meijgaard, Isabella Velicogna, and Bert Wouters. Partitioning recent greenland mass loss. *Science*, 326(5955):984–986, 2009.

Paul R. Holland, Adrian Jenkins, and David M. Holland. The response of ice shelf basal melting to variations in ocean temperature. *Journal of Climate*, 21(11):2558–2572, 2008.

Roman J. Motyka, Martin Truffer, Mark Fahnestock, John Mortensen, S. Rysgaard, and Ian Howat. Submarine melting of the 1985 jakobshavn isbrêfloating tongue and the triggering of the current retreat. *J. Geophys. Res.*, 116, 2011.

Fiammetta Straneo, Gordon Hamilton, David Sutherland, Leigh Stearns, Fraser Davidson, Mike Hammill, Garry Stenson, and Aqqalu Rosing-Asvid. Rapid circulation of warm subtropical waters in a major glacial fjord in East Greenland. *Nature Geoscience*, 3(3):182–186, 02 2010.

H.E. Huppert and E.G. Josberger. The melting of ice in cold stratified water. *Journal of Physical Oceanography*, 10:953–960, 1980.

Herbert E. Huppert and J. Stewart Turner. Ice blocks melting into a salinity gradient. *Journal of Fluid Mechanics*, 100(02):367–384, 1980.

Fiammetta Straneo, Ruth Curry, David Sutherland, Gordon Hamilton, Claudia Cenedese, Kjetil Vage, and Leigh Stearns. Impact of fjord dynamics and glacial runoff on the circulation near helheim glacier. *Nature Geoscience*, 4(5):322–327, 2011.

J. Mortensen, K. Lennert, J. Bendtsen, and S. Rysgaard. Heat sources for glacial melt in a sub-arctic fjord (godthâbsfjord) in contact with the greenland ice sheet. *J. Geophys. Res.*, 116, 2011.

Robert S. Pickart, Daniel J. Torres, and Paula S. Fratantoni. The east greenland spill jet. *Journal of Physical Oceanography*, 35(6): 1037–1053, 2005.

David A. Sutherland and Robert S. Pickart. The East Greenland Coastal Current: Structure, variability, and forcing. *Progress In Oceanography*, 78(1):58–77, 2008.

T. W. N. Haine, S. Zhang, G. W. K. Moore, and I. A. Renfrew. On the impact of high-resolution, high-frequency meteorological forcing on denmark strait ocean circulation. *Quarterly Journal of the Royal Meteorological Society*, 135(645):2067–2085, 2009.

M. G. Magaldi, T. W. N. Haine, and R. S. Pickart. On the nature and variability of the east greenland spill jet: A case study in summer 2003. *Journal of Physical Oceanography*, 2011.

G. W. K. Moore and I. A. Renfrew. Tip Jets and Barrier Winds: A QuikSCAT Climatology of High Wind Speed Events around Greenland. *Journal of Climate*, 18(18):3713–3725, 2005.

Thomas Klein and Günther Heinemann. Interaction of katabatic winds and mesocyclones near the eastern coast of greenland. *Meteorological Applications*, 9(04):407–422, 2002.

J. S. Turner. Turbulent entrainment: the development of the entrainment assumption, and its application to geophysical flows. *Journal of Fluid Mechanics*, 173:431–471, 1986.

B. R. Morton, Geoffrey Taylor, and J. S. Turner. Turbulent Gravitational Convection from Maintained and Instantaneous Sources. *Proceedings of the Royal Society of London. Series A. Mathematical and Physical Sciences*, 234(1196):1–23, 1956.

T. H. Ellison and J. S. Turner. Turbulent entrainment in stratified flows. *Journal of Fluid Mechanics*, 6(03):423–448, 1959.

Douglas MacAyeal and Stanley Jacobs. Evolution of tidally triggered melt water plumes below ice shelves. *Antarctic Research Series*, 43: 133–143, 1985.

Andrew J. Wells and M. Grae Worster. A geophysical-scale model of vertical natural convection boundary layers. *Journal of Fluid Mechanics*, 609:111–137, 2008.

David M. Holland and Adrian Jenkins. Modeling Thermodynamic Ice–Ocean Interactions at the Base of an Ice Shelf. *Journal of Physical Oceanography*, 29(8):1787–1800, 1999.

Miles McPhee. *Air-ice-ocean-interaction: Turbulent Ocean Boundary Layer Exchange Processes*. Springer, 2008.

Miles G. McPhee, Gary A. Maykut, and James H. Morison. Dynamics and thermodynamics of the ice/upper ocean system in the marginal ice zone of the Greenland sea. *J. Geophys. Res.*, 92(C7):7017–7031, 1987. doi: 10.1029/JC092iC07p07017.

J. Determan and R. Gerdes. Melting and freezing beneath ice shelves: implications from a three-dimensional ocean-circulation model. *Annals of Glaciology*, 20(1):413–419, 1994.

H. H. Hellmer and D. J. Olbers. A two-dimensional model for the thermohaline circulation under an ice shelf. *Antarctic Science*, 1 (04):325–336, 1989.

M. Scheduikat and D. J. Olbers. A one-dimensional mixed layer model beneath the Ross Ice Shelf with tidally induced vertical mixing. *Antarctic Science*, 2(1):29–42, 1990.

Adrian Jenkins. A One-Dimensional Model of Ice Shelf-Ocean Interaction. *J. Geophys. Res.*, 96(C11):20671–20677, 1991. doi: 10.1029/91JC01842.

B. A Kader and A. M Yaglom. Heat and mass transfer laws for fully turbulent wall flows. *International Journal of Heat and Mass Transfer*, 15(12):2329–2351, 12 1972.

B. A. Kader and A. M. Yaglom. Turbulent heat and mass transfer from a wall with parallel roughness ridges. *International Journal of Heat and Mass Transfer*, 20(4):345–357, 4 1977.

Adrian Jenkins, Keith W. Nicholls, and Hugh F. J. Corr. Observation and Parameterization of Ablation at the Base of Ronne Ice Shelf, Antarctica. *Journal of Physical Oceanography*, 40(10):2298–2312, 2011/11/16 2010.

Anny Cazenave and William Llovel. Contemporary sea level rise. *Annual Review of Marine Science*, 2(1):145–173, 2009. doi: 10.1146/annurev-marine-120308-081105.

Glenn A. Milne, W. Roland Gehrels, Chris W. Hughes, and Mark E. Tamisiea. Identifying the causes of sea-level change. *Nature Geoscience*, 2:471–478, 2009.

Jonathan Bamber, Michiel van den Broeke, Janneke Ettema, Jan Lenaerts, and Eric Rignot. Recent large increases in freshwater fluxes from greenland into the north atlantic. *Geophys. Res. Lett.*, 39(19):L19501, 10 2012. doi: 10.1029/2012GL052552.

Ian Joughin, Waleed Abdalati, and Mark Fahnestock. Large fluctuations in speed on greenland's jakobshavn isbrae glacier. *Nature*, 432 (7017):608–610, 2004.

Leigh A. Stearns and Gordon S. Hamilton. Rapid volume loss from two east greenland outlet glaciers quantified using repeat stereo satellite imagery. *Geophys. Res. Lett.*, 34(5), 2007.

Ian M. Howat, Ian Joughin, and Ted A. Scambos. Rapid Changes in Ice Discharge from Greenland Outlet Glaciers. *Science*, 315(5818): 1559–1561, 2007.

Ian M. Howat, Ian Joughin, Mark Fahnestock, Benjamin E. Smith, and Ted A. Scambos. Synchronous retreat and acceleration of southeast Greenland outlet glaciers 2000-2006: ice dynamics and coupling to climate. *Journal of Glaciology*, 54(646-660), 2008.

Robert H. Thomas. Force-perturbation analysis of recent thinning and acceleration of Jakobshavn Isbrae, Greenland. *Journal of Glaciology*, 50(168):57–66, 2004.

Andreas Vieli and Faezeh Nick. Understanding and Modelling Rapid Dynamic Changes of Tidewater Outlet Glaciers: Issues and Implications. *Surveys in Geophysics*, 32(4-5):437–458, 2011.

T. Murray, K. Scharrer, T. D. James, S. R. Dye, E. Hanna, A. D. Booth, N. Selmes, A. Luckman, A. L. C. Hughes, S. Cook, and P. Huybrechts. Ocean regulation hypothesis for glacier dynamics in

southeast greenland and implications for ice sheet mass changes. *J. Geophys. Res.*, 115, 2010.

P. Christoffersen, R. I. Mugford, K. J. Heywood, I. Joughin, J. A. Dowdeswell, J. P. M. Syvitski, A. Luckman, and T. J. Benham. Warming of waters in an East Greenland fjord prior to glacier retreat: mechanisms and connection to large-scale atmospheric conditions. *The Cryosphere*, 5(3):701–714, 2011.

F. Straneo, D.A. Sutherland, D. Holland, C. Gladish, G.S. Hamilton, H.L. Johnson, E. Rignot, Y. Xu, and M. Koppes. Characteristics of ocean waters reaching Greenland's glaciers. *Annals of Glaciology*, 53(60):202–210, 2012.

V.W. Chu, L.C. Smith, A.K. Rennermalm, R.R. Forster, J.E. Box, and N. Reehy. Sediment plume response to surface melting and supraglacial lake drainages on the Greenland ice sheet. *Journal of Glaciology*, 55(194):1072–1082, 2009.

Sarah B. Das, Ian Joughin, Mark D. Behn, Ian M. Howat, Matt A. King, Dan Lizarralde, and Maya P. Bhatia. Fracture Propagation to the Base of the Greenland Ice Sheet During Supraglacial Lake Drainage. *Science*, 320(5877):984–986, 2008.

E. Hanna, J. Cappelen, X. Fettweis, P. Huybrechts, A. Luckman, and M. H. Ribergaard. Hydrologic response of the Greenland ice sheet: the role of oceanographic warming. *Hydrological Processes*, 23(1): 7–30, 2009.

Eric Rignot, Michele Koppes, and Isabella Velicogna. Rapid submarine melting of the calving faces of west greenland glaciers. *Nature Geosci*, 3(3):187–191, 2010.

Roman J. Motyka, Lewis Hunter, Keith A. Echelmeyer, and Cathy Connor. Submarine melting at the terminus of a temperate tidewater glacier, LeConte Glacier, Alaska, USA. *Annals of Glaciology*, 36(1): 57–65, 2003.

Kumiko Azetsu-Scott and Francis C. Tan. Oxygen isotope studies from Iceland to an East Greenland Fjord: behaviour of glacial meltwater plume. *Marine Chemistry*, 56(3-4):239–251, 1997.

Adrian Jenkins. Convection-driven melting near the grounding lines of ice shelves and tidewater glaciers. *Journal of Physical Oceanography*, 41:C08043, 2011. doi: doi:10.1029/2007JC004368.

Y. Xu, E. Rignot, D. Menemenlis, and M.N. Koppes. Numerical experiments on subaqueous melting of Greenland tidewater glaciers in response to ocean warming and enhanced subglacial runoff. *Annals of Glaciology*, 53(60):229–234, 2012.

Frands Schjøth, Camilla S. Andresen, Fiammetta Straneo, Tavi Murray, Kilian Scharrer, and Alexander Korablev. Campaign to map the bathymetry of a major Greenland fjord. *Eos Trans. AGU*, 93 (14):141, 2012.

J.O. Andreasen. Seasonal surface-velocity variations on a sub-polar glacier in West Greenland. *Journal of Glaciology*, 31:319–323, 1985.

H. Jay Zwally, Waleed Abdalati, Tom Herring, Kristine Larson, Jack Saba, and Konrad Steffen. Surface Melt-Induced Acceleration of Greenland Ice-Sheet Flow. *Science*, 297(5579):218–222, 2002.

Ginny A. Catania, Thomas A. Neumann, and Stephen F. Price. Characterizing englacial drainage in the ablation zone of the Greenland ice sheet. *Journal of Glaciology*, 54(187):567–578, 2008.

John Marshall, Alistair Adcroft, Chris Hill, Lev Perelman, and Curt Heisey. A finite-volume, incompressible Navier Stokes model for studies of the ocean on parallel computers. *J. Geophys. Res.*, 102 (C3):5753–5766, 1997a. doi: 10.1029/96JC02775.

John Marshall, Chris Hill, Lev Perelman, and Alistair Adcroft. Hydrostatic, quasi-hydrostatic, and nonhydrostatic ocean modeling. *J. Geophys. Res.*, 102:5733–5752, 1997b.

A. Adcroft, C. Hill, J. Marshall, and P. Heimbach. Overview of the formulation and numerics of the MIT GCM. In ECMWF, editor, *Proceedings of the ECMWF: Seminar Series on Numerical Methods, Recent Developments in Numerical Methods for Atmosphere and Ocean Modelling*, pages 139–149, 2004.

Michael A. Spall. On the Role of Eddies and Surface Forcing in the Heat Transport and Overturning Circulation in Marginal Seas. *Journal of Climate*, 24(18):4844–4858, 2011.

John Marshall, Helen Jones, and Christopher Hill. Efficient ocean modeling using non-hydrostatic algorithms. *Journal of Marine Systems*, 18(1–3):115–134, 12 1998.

David R. Jackett and Trevor J. Mcdougall. Minimal Adjustment of Hydrographic Profiles to Achieve Static Stability. *Journal of Atmospheric and Oceanic Technology*, 12(2):381–389, 1995. doi: 10.1175/1520-0426(1995)012¡0381:MAOHPT¿2.0.CO;2.

S. Legg and A. Adcroft. Internal Wave Breaking at Concave and Convex Continental Slopes. *Journal of Physical Oceanography*, 33: 2224–2246, 2003.

S. Legg, R.W. Hallberg, and J.B. Girton. Comparison of entrainment in overflows simulated by z-coordinate, isopycnal and non-hydrostatic models. *Ocean Modelling*, 11(1-2):69–97, 2006.

Martin Visbeck, John Marshall, and Helen Jones. Dynamics of Isolated Convective Regions in the Ocean. *Journal of Physical Oceanography*, 26(9):1721–1734, 1996.

Adrian Jenkins, Hartmut H. Hellmer, and David M. Holland. The role of meltwater advection in the formulation of conservative boundary conditions at an ice–ocean interface. *Journal of Physical Oceanography*, 31(1):285–296, 2011/12/14 2001.

M. Losch. Modeling ice shelf cavities in a z coordinate ocean general circulation model. *J. Geophys. Res.*, 113, 2008.

Michael Steele, George L. Mellor, and Miles G. Mcphee. Role of the Molecular Sublayer in the Melting or Freezing of Sea Ice. *Journal of Physical Oceanography*, 19(1):139–147, 1989.

S. H. Mernild, G. E. Liston, I. M. Howat, Y. Ahn, K. Steffen, B. Hasholt, B. H. Jakobsen, B. Fog, and D. van As. Freshwater flux to Sermilik Fjord, SE Greenland. *The Cryosphere Discussions*, 4:1195–1224, 2010.

M. L. Andersen, T. B. Larsen, M. Nettles, P. Elosegui, D. van As, G. S. Hamilton, L. A. Stearns, J. L. Davis, A. P. Ahlstrøm, J. de Juan, G. Ekström, L. Stenseng, S. A. Khan, R. Forsberg, and D. Dahl-Jensen. Spatial and temporal melt variability at Helheim Glacier, East Greenland, and its effect on ice dynamics. *J. Geophys. Res.*, 115:F04041, 2010. doi: 10.1029/2010JF001760.

R. I. Mugford and J. A. Dowdeswell. Modeling glacial meltwater plume dynamics and sedimentation in high-latitude fjords. *J. Geophys. Res.*, 116, 2011.

V. Chow. *Open-Channel Hydraulics*. McGraw-Hill, New York, 1959.

J.S. Turner. *Buoyancy Effects in Fluids*. Cambridge University Press, 1980.

Kirk Bryan, Syukuro Manabe, and Ronald C. Pacanowski. A Global Ocean-Atmosphere Climate Model - Part II, The Oceanic Circulation. *Journal of Physical Oceanography*, 5(1):30–46, 1975.

D. A. Sutherland and F. Straneo. Estimating ocean heat transports and submarine melt rates in Sermilik Fjord, Greenland, using lowered acoustic Doppler current profiler (LADCP) velocity profiles. *Annals of Glaciology*, 53(60):50–58, 2012.

A. Adcroft and R. Hallberg. On methods for solving the oceanic equations of motion in generalized vertical coordinates. *Ocean Modelling*, 11:224–233, 2006.

F. Straneo, P. Heimbach, O. Sergienko, et al. Challenges to Understand the Dynamic Response of Greenlands Marine Terminating Glaciers to Oceanic and Atmospheric Forcing. *Bulletin of the American Meteorological Society*, accepted, 2013.